Chapter 4
Hard and Superhard Multicomponent Nitride Coatings Deposited Using Vacuum-Arc Evaporation:
The Effects of Cr and Si on the Structure and Properties of the Nanostructured (Zr-Ti-Nb)N Coatings

Didar Yeskermessov
https://orcid.org/0000-0002-2206-8132
D. Serikbayev East Kazakhstan Technical University, Kazakhstan

Yerkezhan Tabiyeva
https://orcid.org/0000-0002-9726-7187
D. Serikbayev East Kazakhstan Technical University, Kazakhstan

Zhanerke Toleukhanova
https://orcid.org/0009-0002-9254-3901
D. Serikbayev East Kazakhstan Technical University, Kazakhstan

Waqar Ahmed
University of Lincoln, UK

Zarina Aringozhina
https://orcid.org/0009-0001-8428-4033
D. Serikbayev East Kazakhstan Technical University, Kazakhstan

ABSTRACT

This chapter is devoted to experimental research on the investigated of the structural-phase, morphology, elemental composition, physical-mechanical, and tribological properties (friction, wear, and adhesion) of hard and superhard micro- and nanostructured coatings of systems based on (Zr-Ti-Nb)N, (Zr-Ti-Cr-Nb)N, and (Zr-Ti-Cr-Nb-Si)N were fabricated by vacuum-arc deposition in the nitrogen atmosphere. The

DOI: 10.4018/978-1-6684-6830-2.ch004

authors in the work used advanced proven experimental research methods (SEM-EDX, TEM-EDS, XRD, SIMS, GDMS, PIXE, XPS, AFM, hardness measurements, and adhesion testing), as well as theoretical methods for analysing the results. Based on the results obtained, according to the experimental data, an optimal mode was selected that provides an increase in mechanical and tribological characteristics, and a method for vacuum-arc surface hardening was also developed. Such coatings seem to have prospects as protective ones for couples of friction and cutting tools.

1. INTRODUCTION

High-tech industries such as: rocket and space, aviation, petroleum and gas production, as well as various alternative energy industries today pay great attention to improving the reliability and efficiency of products that are operated in various environments. The emphasis in modern materials analysis is usually directed at the structure and composition of the surface and outer layers of materials from several tens to hundreds of nanometers.

In particular, products based on titanium (Ti) and its alloys, which are used in various fields of industry, are of considerable interest due to their properties. The literature data indicate that various methods of surface treatment are used to improve the physical and mechanical properties of titanium and alloys based on it. The emphasis is on the realization that the surface and near-surface areas control many mechanical and chemical properties of solids: corrosion, friction, wear, adhesion and destruction. In addition, the composition and structure of the outer layers can be adapted using directed energy processes using lasers or electron and ion beams, as well as using more traditional methods such as oxidation and diffusion. The research of nanostructured objects is the fastest developing in modern materials science, since the ultrafine dispersed structure causes a significant improvement, and in some cases, a radical change in the properties of the material (Gavaleiro & De Hosson, 2006; Voevodin et al., 2004).

The investigation of ultrafine-grained materials has shown that a decrease in the size of crystals below a certain threshold value can lead to a significant change in properties. Dimensional effects are manifested when the average size of crystalline grains does not exceed 100 nm, and is most clearly observed when their size approaches 10 nm, and the intercrystalline (intergranular layer) is units of nanometres, consisting as a rule of an amorphous phase like nitrides, oxides and carbides (Gavaleiro & De Hosson, 2006; Nordin et al., 1998; Nordin et al., 1999; Pogrebnjak et al., 2015; Voevodin et al., 2004). From a physical point of view, the transition to the nanostate is associated with the appearance of dimensional effects, which should be understood as a complex of phenomena associated with changes in the properties of matter due to the coincidence of the size of the microstructure block and some critical length, characterizing the phenomenon as the free path lengths of electrons and phonons, the wall thickness of domains, the critical radius of the dislocation loop, etc (Morris, 1998). Conventionally, these coatings can be divided into conditionally hard (< 40 GPa) and superhard (>40 GPa), obtained using CVD (chemical vapor deposition), PVD (physical vapor deposition), magnetron sputtering and ion-assisted deposition methods (Kim & Cha, 2005; Lee et al., 2007; Leng et al., 2001; Rizzo et al., 2006; Shin et al., 2002).

Based on this, nanostructured nitride coatings based on multicomponent alloys containing at least 3-4 constituent elements are of scientific interest, and their synthesis and intensive research is an urgent task of materials science. Thus, the most diverse combination of constituent elements and changes in the physical parameters of deposition (working gas pressure and substrate bias voltage) will make it possible to change the structural state (grain size, texture, residual stresses) and properties of condensates

in a wide range. Proceeding from the foregoing, the synthesis and study of nitride coatings of transition metals based on multicomponent alloys by vacuum-arc deposition is an urgent task. The analysis of the regularities of the formation of nanocrystalline coatings, the investigation of the correlation of their structural-phase state and properties depending on the deposition modes are of scientific and practical interest.

Therefore, the objective of this work is to conduct comprehensive research of the microstructure, elemental and phase compositions, surface morphology, physical-mechanical and tribological characteristics of the coating based on (Zr-Ti-Nb)N obtained by vacuum-arc deposition of the cathode, when the deposition and alloying parameters of the coating with chromium (Cr) and silicon (Si) elements change.

And for this reason, this chapter is generally devoted to experimental study on the investigation of the structural-phase, elemental composition, as well as the physical-mechanical and tribological properties of solid and superhard micro- and nanostructured coatings of systems based on Ti, Zr, Cr, Nb, Si, N elements. So, in section 2, the objects of research are discussed, as well as the principles, methods of obtaining, means of testing and determining the physical-mechanical and tribological properties of coatings are described in detail. The description of the equipment used in the work is given. Section 3 presents and analyzes the results of experimental and theoretical studies of the morphology, elemental and phase composition of coatings based on (Zr-Ti-Nb), (Zr-Ti-Nb-Cr) and (Zr-Ti-Nb-Cr-Si) obtained by vacuum-arc deposition. In Section 4, the relationship between mechanical properties and deposition parameters of multicomponent nitride coatings based on Zr, Ti, Nb, Cr, and Si was studied, and the tribological characteristics were also analyzed.

2. EQUIPMENT AND METHODS FOR RESEARCHING THE STRUCTURE AND PROPERTIES OF MULTI-COMPONENT NANOSTRUCTURED COATINGS

2.1. Materials and Equipment for Coating Deposition

Previously, the development of new technologies and principles for the design of new materials was based on the use of one to three elements as the main ones, for example: steel (Fe), heat-resistant alloys (Mn, Zr), bulk metallic glasses (Ni, Co), protective coatings based on (Ti). However, such compounds did not always meet the basic requirements for coatings. Further development of materials science led to the formation of 3- and 4-nitride systems, which were characterized by a significant increase in functional properties compared to binary nitrides. Recently, the so-called multicomponent (multi-element) alloys with variable chemical composition, which are characterized by universalization of physical and chemical properties, have been widely used.

It is known that, according to the configurational model of matter, the properties of nitride coatings (hardness, adhesive activity (strength), melting point, etc.) depend on the statistical weight of stable atomic sp- and d-configurations (SWSC) (Azarenkov et al., 2012). If titanium nitride (TiN) is considered as the basis, then its stability can be increased by doping with elements containing a large number of electrons at the d-level. Mostly stable d-configurations have elements of groups IV, V and VI of the periodic system. In this case, those alloying elements have the greatest influence on the properties of alloys, the atoms of which differ to the greatest extent from the atoms of the base in their external structure. The most common alloying elements are transition metals of groups IV and VI of the periodic system. Such elements have a high SWSC sp- и d- configurations at room temperature (Ti – 43%, Zr – 52%, Hf – 55%,

Table 1. Characteristics of elements used to produce nitride coatings

Element	Atomic Mass (g/mol)	Atomic Radius (pm)	Density (g/cm^3)	Melting Temperature (K)	Enthalpy of Formation (kJ/mol)
Ti	47.867	147	4.54	1933	336.3
Nb	92.906	146	8.57	2741	237.8
Zr	91.224	160	6.506	2125	355.6
Cr	51.996	130	7.19	2130	342.1
Si	28.086	132	2.33	1688	383.1
N	14.007	92	0.00125	63.29	-

V – 63%, Nb – 76%, Si – 81%, Cr – 73%, Mo – 84%, W – 96%) (Samsonov, 1969). According to the configurational model of a substance, the higher their total SWSC, the lower the adhesive interaction of the contacting metals. Thus, an increase in the properties of the TiN compound (for example: adhesive activity) is possible due to doping with elements that, on the one hand, will increase the SWSC of the d-configuration, and on the other hand, the elements must have high thermal stability. This circumstance suggests that alloying the TiN compound with atoms of Hf-, V-, Nb-, W-, Cr-, Si-elements will make it possible to obtain a compound with a unique set of properties (high hardness, heat resistance, melting point, etc.). However, taking into account the high degree of chemical affinity, it is advisable to use Zr, Nb, Cr and Si as constituent elements (Table 1), since the use of elements with a lower chemical affinity with nitrogen makes it difficult to grow a mononitride film.

If we compare the enthalpy of formation (-ΔH, kJ/mol), then the most stable nitrides with a high heat of formation are ZrN – 355.6 kJ/mol, TiN – 336.6 kJ/mol, Nb_2N – 255.8 kJ/mol, NbN – 237.8 kJ/mol, Cr_2N – 135.1 kJ/mol, CrN – 123.4 kJ/mol (Azarenkov et al., 2012). A class of compounds such as Cr_2N and CrN although it has the lowest heat of formation, however, has high functional properties (resistance to oxidation and wear). It should be noted that the Nb and Cr elements have a body-centered cubic (BCC)-lattice at room temperature, while Zr, Ti, and Si face-centered cubic (FCC) have an face-centered tightly packed (FCTP) lattice at room temperature and a BCC lattice at high temperatures. Thus, the high degree of chemical affinity of the constituent elements with nitrogen, as well as the stabilization of the BCC-lattice due to the inclusion of Nb and Cr, will make it possible to obtain a nitride phase based on a high-entropy single-phase alloy. An analysis of literature sources has shown that alloying titanium nitride with zirconium atoms favourably affects the functional properties, in particular, wear resistance increases due to the formation of a thin layer of zirconium oxide on the coating surface. Additional modification with Cr, Nb additives improves the thermal stability, oxidation and corrosion resistance of the protective coating, reduces the friction coefficient, and increases the level of hardness. It should also be noted that with the transition of metal nitrides from group VI (CrN, Cr_2N) to group IV (ZrN, NbN) resistance to high-temperature oxidation increases. Based on the above, it can be assumed that the compound based on Ti, Zr, Nb, Cr, Si and N will have a unique set of properties: high hardness, high oxidation resistance, excellent tribological characteristics and other functional properties.

Coatings were obtained by vacuum-arc evaporation at the “Bulat-6” installation, which consisted of a vacuum chamber, a control rack, a high-voltage rectifier, and three power sources for arc evaporators. (Shulayev et al., 2006). The main deposition parameters are given in Table 2.

Table 2. Deposition parameters of nitride coatings

Series (Sample) No.	Deposited Material	Arc current I_C, A	Nitrogen Pressure P_N, Pa	Bias Voltage U_b, V
1	(Zr-Ti-Nb)N	95	0.04	-100
2			0.5	-100
1	(Zr-Ti-Cr-Nb)N	110	0.3	-100
2			0.7	-100
3			0.3	-200
4			0.7	-200
1	(Zr-Ti-Cr-Nb-Si)N	110	0.3	-100
2			0.3	-200

Coatings (Zr-Ti-Nb)N, (Zr-Ti-Cr-Nb)N and (Zr-Ti-Cr-Nb-Si)N were deposited on a polished rotating substrate (material-steel 12Cr18Ni9Ti, A 570 Grade 36 steel and Si) 15×15×2.5 mm^3 in size with initial surface roughness R_a » 0.09 μm. The evaporated materials were solid cathodes Zr-Ti-Nb (Zr – 35 at%, Nb – 35 at%, Ti – 30 at%), Zr-Ti-Cr-Nb (Cr – 37.39 at%, Zr –27.99 at%, Nb – 22.30 at%, Ti – 12.32 at%) and Zr-Ti-Cr-Nb-Si (Cr –17.08 at%, Zr – 30.19 at%, Nb – 9.67 at%, Ti – 39.96 at%, Si – 3.1 at%). Cathodes from multicomponent alloys of the Zr-Ti-Nb, Zr-Ti-Cr-Nb and Zr-Ti-Cr-Nb-Si systems were fabricated by vacuum-arc melting in a high-purity argon atmosphere. Melting was carried out with a non-consumable tungsten electrode into a water-cooled copper container (hearth). The obtained ingots were remelted 6-7 times with a cooling rate of about 50 K/s for the final homogenization of the composition. The deposited (Zr-Ti-Nb)N, (Zr-Ti-Cr-Nb)N and (Zr-Ti-Cr-Nb-Si)N coatings were made in a molecular N_2 atmosphere, the pressure of the working gas varied from 0.04 to 0.7 Pa. The substrate bias was chosen as the control parameter, which varied from -95 to -200 V. The substrates were heated to 450°C before deposition. The distance between the substrates and the cathode was 250 mm. In practice, it is considered expedient to obtain thin coatings (up to 10 μm) due to a decrease in the influence of the scale factor on the properties of the substrate and the likelihood of destructive stresses in the coating itself. Following these, the thickness of the coatings (Zr-Ti-Nb)N, (Zr-Ti-Cr-Nb)N and (Zr-Ti-Cr-Nb-Si)N is 6.7, 10 and 6.2÷6.8 μm, respectively. The block diagram of the "Bulat-6" installation is shown in Figure 1.

The vacuum chamber is a cylindrical vessel with an inner diameter of 500 mm and a length of 500 mm with a horizontal axis (Figure 2). Vacuum-arc evaporators are fixed in the centre of the covers with flanges located at both ends of the chamber, as well as in the branch pipe located in the upper part of the chamber. In the lower part of the chamber there is a similar branch pipe with a flange, where a rotary device is fixed, on which the substrate holder is located. The rotary device is electrically isolated from the vacuum chamber and provides a rotation speed of 8 rpm. The chamber is evacuated using a steam-oil and mechanical vacuum pumps. (Shulayev et al., 2006).

The vacuum-arc evaporator (plasma source) consists of two main parts: the first is the cathode, containing the evaporated cathode with a magnetic system for holding the cathode spot on the evaporated surface of the cathode and an arc discharge ignition device, the second is the anode, which is a branch pipe with magnetic coils for focusing the plasma flow. In the case of using the cathode part as an independent evaporator without the anode part, the vacuum chamber body acts as the anode. Due

Figure 1. Installation block diagram "Bulat-6"

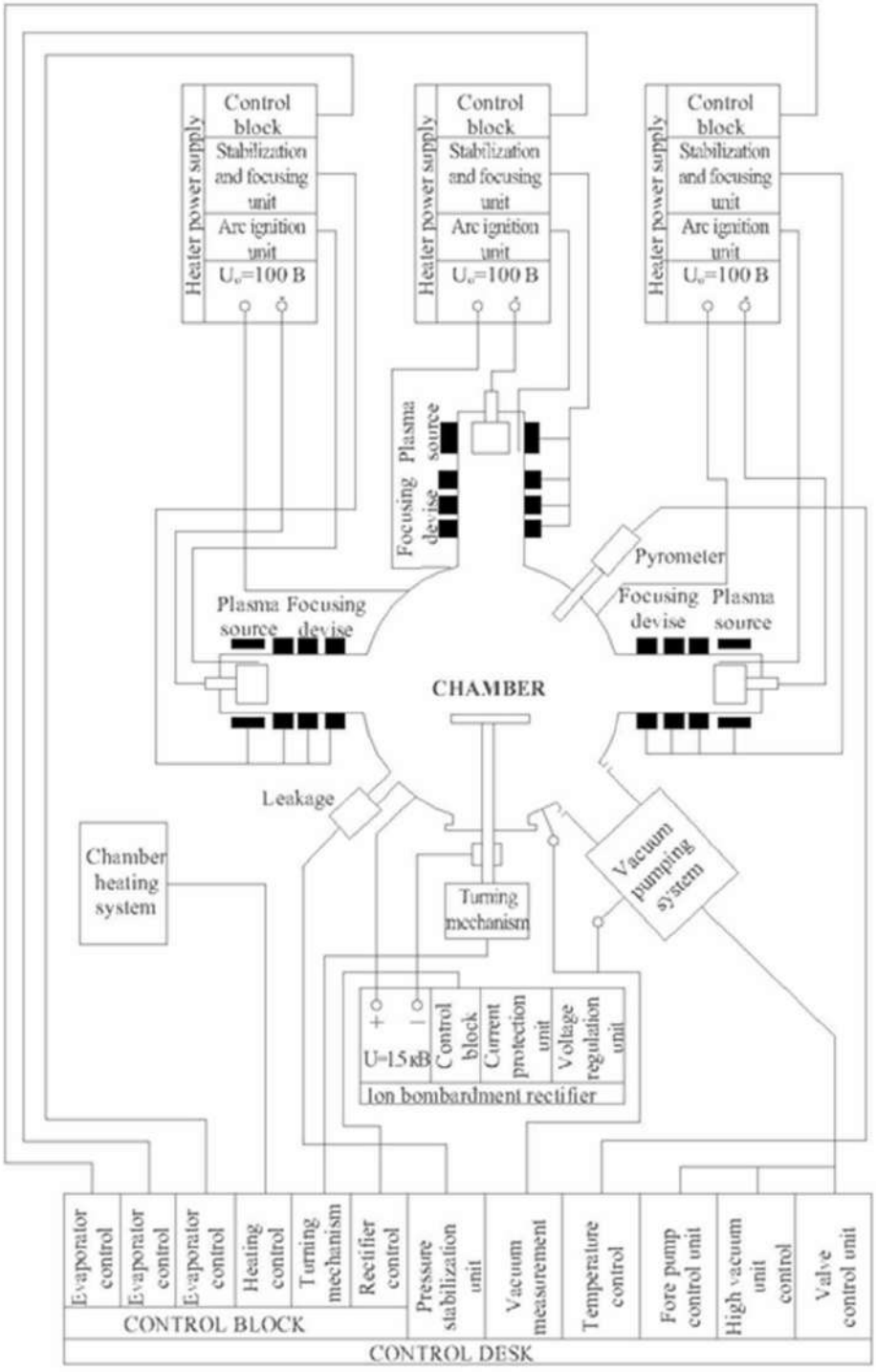

Figure 2. Vacuum-arc installation "Bulat-6": a – appearance; b – scheme

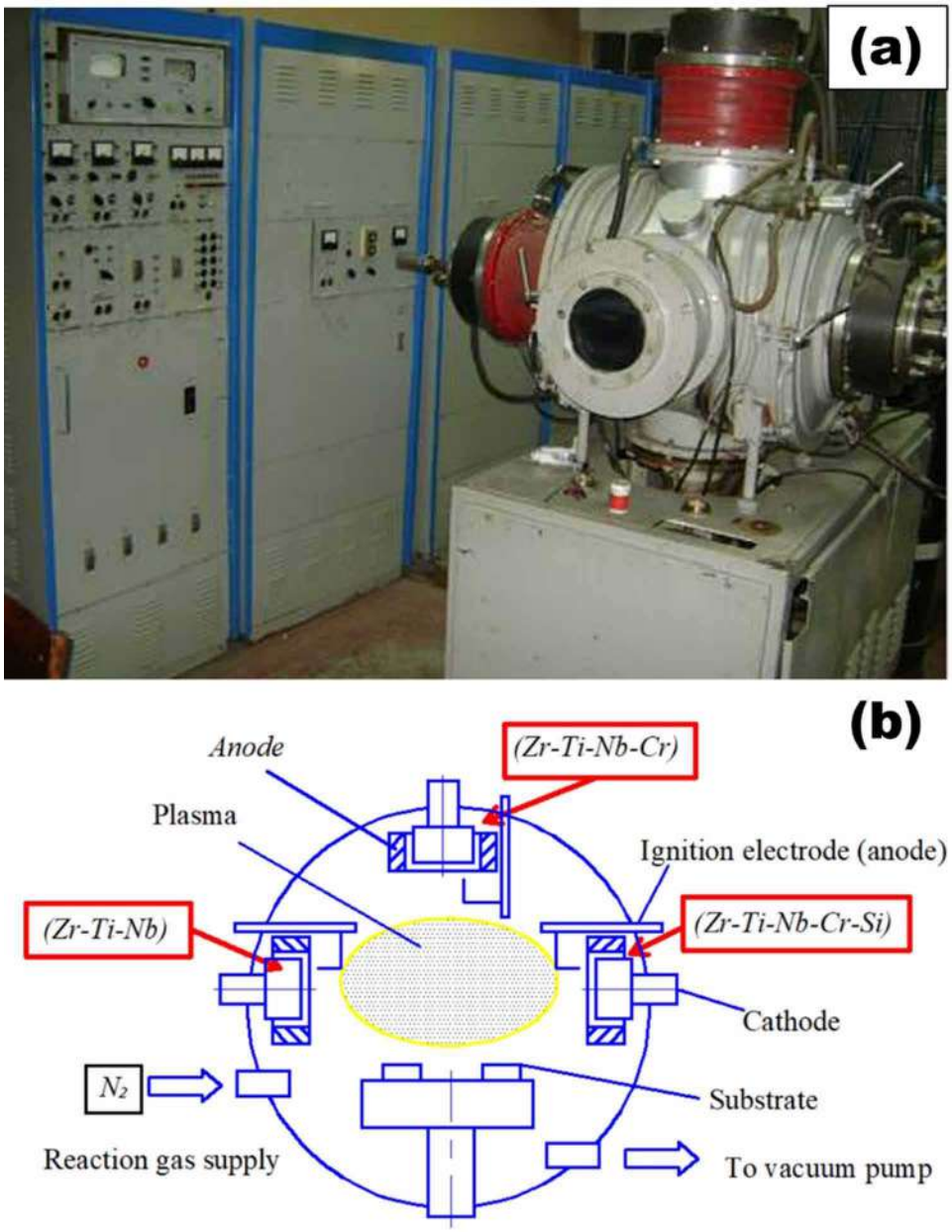

to this, the rate of deposition of coatings in the centre of the chamber increases by about one and a half to two times. The high voltage rectifier provides a voltage of 0.1 to 1.7 kV with a maximum current of 15 A. Power supplies for arc evaporators provide smooth current control from 90 to 150 A and an open circuit voltage of 100 V. The unit is equipped with a gas supply system with automatic maintenance of its pressure in the chamber in the range from 0.01 to 15 Pa (Shulayev et al., 2006).

2.2. Methods for Investigating the Structure and Properties of Multicomponent Nitride Coatings

Modern diagnostics of a substance implies the use of complementary methods for studying the physical and chemical parameters of structures, which provides complete information about the structure and physical-chemical properties. At the same time, the analysis of the substance consists in interpreting the signals recorded by the instruments, which can be the energy and intensity of the energy spectrum of absorbed or emitted electromagnetic radiation, electrons, ions, changes in the strength of the interaction of the probe with the surface under study, etc. (Troyan et al., 2008). This section provides a brief description of the research methods of nanostructured coatings used in the work.

2.2.1. Methods for Studying the Surface Morphology of Coatings

The surface morphology of nitride multicomponent coatings based on (Zr-Ti-Nb)N, (Zr-Ti-Cr-Nb)N and (Zr-Ti-Cr-Nb-Si)N was studied using scanning electron microscopy on JEOL-7000F, JSM-6390LV microscopes with energy-dispersive X-ray spectroscopy (EDS/EDX) analysers and JEOL-6010LA In-TouchScope. The use of such a technique makes it possible to study the sample area or micro-volume by irradiating it with a thin focused electron beam. Changing the angle of incidence of the primary beam makes it possible to study in detail the topography of various microparticles of the sample. Secondary, reflected and absorbed electrons are used to obtain an image of the surface. Of greatest interest are the images obtained using secondary and reflected electrons, which have a relatively high resolution (1.2 nm at 30 kV – JEOL-7000F), and also provide information about the sample areas located in the depth of a complex relief (Engel, 1986). The study was carried out at an accelerating voltage of 20 kV in real time (163.13 s.), while the scanning area was perpendicular to the main optical axis.

An atomic-force microscope (AFM) study was also conducted for a more in-depth detailed analysis of the surface morphology of the obtained nitride coatings. In this method, a change in the interaction force of the tip of the probe (needle) with the surface under study is recorded. The needle is located at the end of a cantilever beam with a known rigidity capable of bending under the action of small forces arising between the surface of the sample and the tip of the tip. These forces in a number of variants of the method can be van der Waals (molecular), electrostatic or magnetic. A beam with a needle is called a cantilever. The deformation of the cantilever is measured by the deflection of the laser beam incident on its back surface, or by the piezoresistive effect that occurs in the cantilever material during bending.

2.2.2. Elemental Analysis of Coatings

The study of the elemental composition of the coating was carried out using a scanning electron microscope JSM-6390LV – by JEOL (Japan), with the prefix of energy dispersive microanalysis INCA Energy by OXFORD Instruments. When electrons interact with matter, response signals of various forms arise (reflected and secondary electrons, Auger electrons, X-rays, absorbed current, etc.), which are used to synchronously construct an image on the monitor screen. Figure 3 shows a diagram of the formation of secondary signals under the influence of an electronic probe. An electron-optical system is not used for image formation, image scaling is carried out by radio-technical means. A scanning electron microscope is a vacuum device, since at normal atmospheric pressures the electron beam is strongly scattered and absorbed, which makes it impossible to focus it. Therefore, the working vacuum in the microscope cham-

Figure 3. Scheme of formation of secondary signals during the interaction of probe electrons with a sample

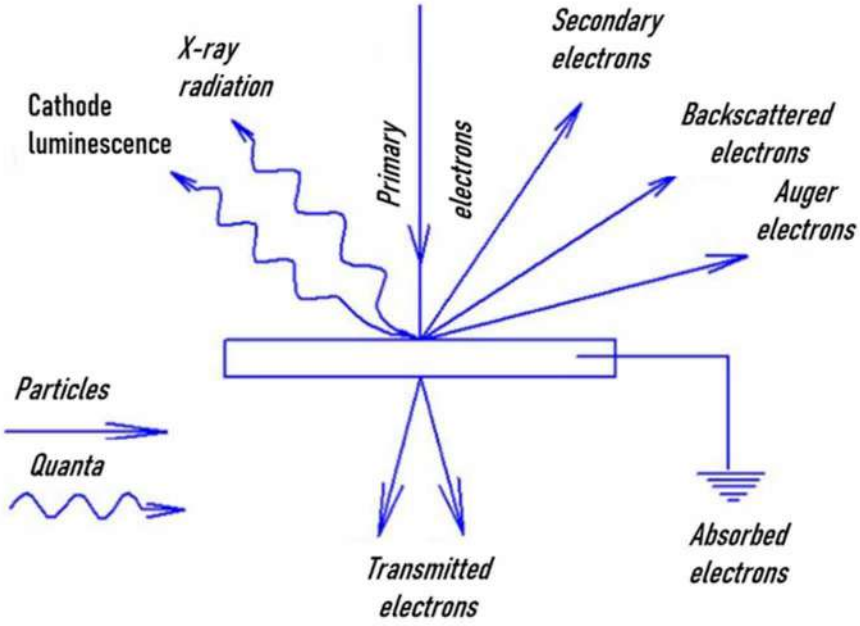

ber should be 10^{-5} Torr or better. The movement of the probe over the surface of the sample should be carried out with very high accuracy. The accuracy of the movement and the size of the probe determine the resolution of the microscope.

As a result of the interaction of the electron beam with the sample surface, a response occurs, which is recorded by the corresponding sensors. The appearance and diagram of the main nodes of the scanning microscope is shown in Figure 4. An electron beam from an electron source by a special condenser system is formed in the form of a well-formed probe and passes through a system of control electrodes or electromagnets that move the beam along the sample surface along a trajectory forming a raster. The signal recorded by the sensors is then used to modulate the brightness of the electron beam in the cathode ray tube of the monitor. The magnitude of this signal will depend on the physical properties of the sample surface and may vary from point to point. As a result, an image of the sample surface is formed on the monitor screen, displaying the topography of the corresponding physical property of the sample under study. Thus, it is possible to study the topography of inhomogeneities of defects and surface conditions: for example, the topology of the surface (grain boundaries, pores, cracks, inhomogeneities of composition, etc.) – in reflected or secondary electrons.

First of all, a scanning electron microscope (SEM) is used to study the structure of the surface. Currently manufactured devices have an increase from tens to several hundred thousand times. The possibility of studying not only the content of a particular chemical element in the sample, but also the distribution of selected chemical elements over the sample surface makes the scanning electron microscopy method unique. The energy dispersion method is based on the registration of the so-called characteristic radiation resulting from electron transitions between the internal energy levels of atoms. Depending on the

Figure 4. Scanning electron microscope (SEM): a – appearance; b – block diagram

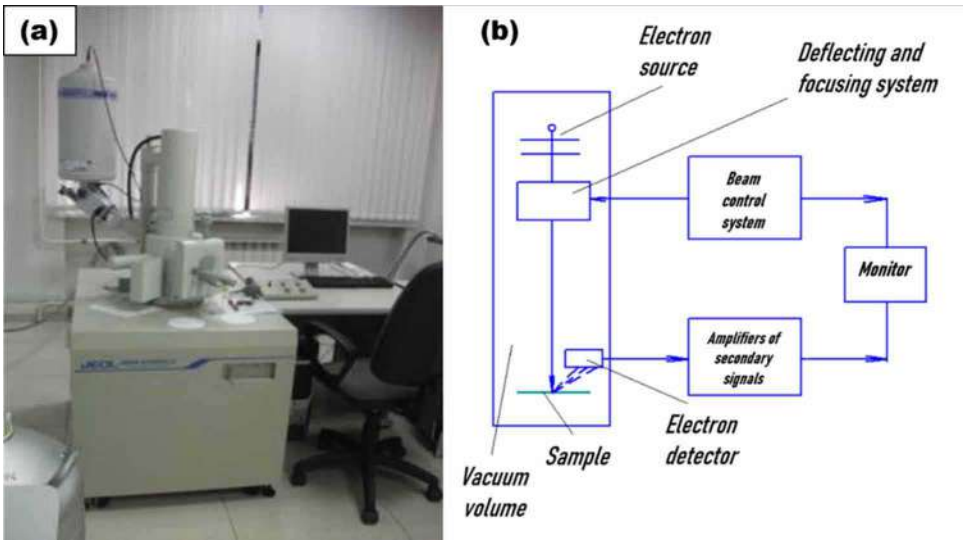

radius of the level, as well as on the binding energy, several types of spectra are distinguished: K, L, M, while only a few X-ray emission lines (K_α, $K_ß$ and L-series) are important for materials science (Uglov et al., 2007). The use of an energy-dispersive semiconductor detector based on Si doped with Li in the energy range from 0.7 to 10 keV makes it possible to identify unknown elements.

Quantitative elemental analysis consists in finding the concentration of the desired element using the measured intensity of continuous radiation. The mass fraction of an element can be determined by the following formula (1) (Gouldsteyn et al., 1984):

$$C_i = \frac{I_i \cdot I_{(B)} \cdot C_{(i)} \cdot G_i}{I_B \cdot I_{(i)} \cdot G_{(i)}} \quad (1)$$

where C_i и $C_{(i)}$ – the mass fractions of element *i* in the analysed micro-volume of the sample and the standard, respectively; I_i – measured intensity of characteristic X-ray radiation; I_B – the measured intensity of continuous radiation. The ratio of *G*-factors takes into account the fact that the standard and the sample may generate unequal intensity of continuous radiation per unit mass in a single volume (Gouldsteyn et al., 1984).

One of the additional methods of quantitative investigation of the elemental composition of coatings is Rutherford backscattering (RBS). One of the advantages of this technique is the indestructibility of the sample structure during the study. The RBS method is based on irradiation of the sample surface with an ion beam with an energy from 1 to 3 MeV. The resulting RBS spectrum is a graph along the abscissa axis of which an energy channel (n_i) is deposited, into which a scattered ion with a certain energy enters, and along the ordinate axis is the number of ions (H_i) that have fallen into the n_i channel (Uglov et al., 2007). The graph itself is a set of surface peaks, the intensity analysis of which provides information about the structure of the surface. One of the many possibilities of RBS is the study of the

distribution of elements by depth (or the construction of concentration profiles). The proportion of the desired element can be found by the formula (2), (3):

$$C_i = \frac{N_i / N_m}{\sum_i N_i / N_m + 1} \tag{2}$$

$$\frac{N_i}{N_m} = \frac{H_i}{H_m}\left(\frac{Z_m}{Z_i}\right)^2 \frac{\left[\varepsilon(E)\right]_i^{ef}}{\left[\varepsilon(E)\right]_m^{ef}} \tag{3}$$

where H_i – the height of the energy peak for the *i*-th element; H_m – the height of the energy peak for the main element (the highest concentration in the sample); Z_i и Z_m – atomic numbers of the *i*-th and main element; $\left[\varepsilon(E)\right]_i^{ef}$ and $\left[\varepsilon(E)\right]_m^{ef}$ – the factor of the effective braking cross-section for the *i*–th and the main element (the upper index means the braking medium, and the lower one means the scattering atom of the element on which the scattering occurs). The studies were carried out on He^+ ions with an energy of 1.7 MeV (scattering angle θ = 170º) with a normal incidence of probing ions on coated samples. At the same time, the energy resolution of the detector was 16 keV, and the dose of helium ions was 5 μCi. Standard software was used to process RBS spectra and obtain profiles of the distribution of elements over the depth of coverage.

Recently, there has been a tendency to use RBS to determine the depth distribution profiles of elements in combination with ion etching methods: secondary mass spectrometry (SIMS) and glow discharge mass spectrometry (GDMS). These methods are destructive in nature and involve spraying the surface (Ganeyev et al., 2012). The fundamental difference between these methods is the mechanism of formation of ions of the studied elements. Thus, in the SIMS method, the formation of ions occurs due to the simultaneous knocking out and ionization of the sample atoms by a beam of primary ions, whereas in the GDMS method, electrons emitted and accelerated in an electric field cause excitation and ionization of the atoms of the working gas (often argon). Further, argon ions bombard the cathode, cause not only ion-electron emission, but also knock out atoms of the cathode material. The atomized atoms of the sample, in turn, participate in various collisions in the plasma, which also lead to excitation and ionization (Ganeyev et al., 2012). The SIMS method is characterized by low detection limits, good spatial resolution (1 microns), allows detecting the presence of any element. The minimum concentrations that can be determined depend on the element, the matrix, the energy of the primary electrons and can vary from 10^{13} to 10^{18} cm^{-3}. The use of the GDMS method also leads to erosion of the coating surface, however, one of the main advantages of the glow discharge is its speed and the ability to study sufficiently thick coatings (several mm).

The study using the SIMS method was carried out using a SAJW-05 analyser equipped with a Physical Electronics 06-350E ion cannon and a QMA-410 Balzers quadrupole mass analyser with a rod diameter of 16 mm. The depth analysis profile was obtained using Ar^+ ions with an energy of 3 keV, the ion beam current was 1.5 μA, the angle of incidence was – 45º. For GDMS analysis, an SMWJ-01 analyser equipped with an SRS-300 quadrupole mass analyser with a rod diameter of 6 mm was used. In this case, the alternating current voltage was 1.8 kV, and the pressure of the working gas (Ar) was 0.2 Torr.

PIXE (particle induced X-ray emission) method is one of the widely used elemental analysis methods based on detection of characteristic X-ray radiation induced by a charged particle beam. One of the main advantages of the PIXE method is the ability to perform analysis in air without placing the sample in a vacuum setup. This method is characterized by high sensitivity due to the use of high-energy ions (0.1-5 MeV). An analysis of the intensity and wavelength of the characteristic X-ray radiation makes it possible to carry out a qualitative and quantitative analysis of the elemental composition of the material under study (Pogrebnyak et al., 2012). To register the emitted X-ray quanta in the PIXE technique, a semiconductor silicon-lithium detector is used. This method is primarily used to determine extremely low impurity concentrations in a coating. The PIXE method can be combined with micrometre beamforming to produce highly accurate maps of the horizontal location of negligible elemental concentrations. Such beams can be used to study biological and vacuum-degrading samples in air (Uglov et al., 2007). For the study, a microbeam of protons (μ-PIXE) with an initial energy of 1.4 MeV was used on the basis of the electrostatic accelerator of the "IPF NANU" (Sumy) with a beam size of up to 0.4 μm (charge 3×10^{-10} C/pixel, raster 50×50, scan step 0.5). As a result, maps of the distribution of the elements Ti, Nb, Cr, Zr, and Si in the coatings immediately after deposition were obtained. The chemical bonding state of the coatings was analysed by X-ray photoelectron spectroscopy (XPS, EC 2401) using MgK_{α} radiation (E=1253.6 eV). Prior to XPS measurements, the samples were subjected to sputter etching in argon plasma for 5 min.

2.2.3. Investigation of the Phase Structure of Coatings

The structure of the coating was studied using transmission electron microscopy (JEOL 2100F) in the dark field mode with an accelerating voltage of 200 and 250 keV. The study of the structure and phase composition was carried out on X-ray diffractometers DRON-4, D8 ADVANCE and Shimadzu XRD-7000 in filtered Cu-K_{α} radiation using a graphite monochromator in the secondary beam. The diffraction spectra were obtained in a point-by-point mode with a scanning step 2θ = 0.02-0.2º, X-ray diffraction was also used using a grazing beam in Cr-radiation at an angle of 3º. The average crystallite size was determined using the Debye-Scherrer equation from the broadening of diffraction peaks, taking into account instrumental broadening and the "Powder Cell 2.4" software. The instrumental broadening was determined at the half-width of the maximum of the standard silicon powder and amounted to 0.14.

The study of the phase composition was carried out on the basis that each crystalline substance (phase) has a certain crystal lattice, characterized by a set of interplanar distances d_{HKL} (Anishik et al., 2011; Umanskiy et al., 1982). The latter are found from the Wulf-Bragg equation:

$$2d_{HKL}\sin\theta = n\lambda \tag{4}$$

where θ – slip angle; λ – wavelength; n – order. Indexing a radiograph involves determining all interference indices (HKL) of each radiograph line. In this case, the interference indices are equal to the product of the plane indices (hkl) and the reflection order n. Indexing of X-ray patterns of crystals depending on syngony is based on different ratios. So, for a cubic lattice:

$$a = \frac{\lambda}{2\sin\theta_i}\sqrt{H_i^2 + K_i^2 + L_i^2} \tag{5}$$

To establish the interference indices of each line, the relation is used:

$$Q_i = \frac{sin^2\theta_i}{sin^2\theta_1} = \frac{H_i^2 + K_i^2 + L_i^2}{H_1^2 + K_1^2 + L_1^2} = \frac{d^2_{H_iK_iL_i}}{d^2_{H_1K_1L_1}} \quad (6)$$

где Q_i – line at the smallest angle θ. Thus, having determined a series of ratios Q_i for all lines of the X-ray diffraction pattern in ascending order, one can determine the grating type, interference indices, and unit cell period. One of the methods of qualitative phase analysis is the comparison of the values of interplanar distances and intensities of the studied sample with the reference one. At the same time, the JCPDS-ASTM card index file is the most widely used. One of the methods of studying the stressed state of a solid is the X-ray diffraction method. This technique allows you to determine the stresses at each point of the object surface at any stress distribution. The X-ray deformation measurement allows the assumption of a plane-stressed state, since the deformation refers to a surface layer with a thickness of ~ 10 microns. There are various ways to determine macro-stresses (principal stress sum method, single oblique survey method, multiple oblique survey method), but all of them can be combined within the so-called $sin^2\psi$-method (Gladkikh et al., 2006; Palatnik et al., 1972). This technique allows the assumption of a random orientation of crystallites, which allows one to write equations relating strain and stress for a homogeneous isotropic medium. To visualize the representation of the deformation of the body, it is convenient to use the so-called deformation ellipsoid - the surface into which the sphere of unit radius, selected in the original undeformed body, passes after deformation of this body. Under the assumption of a plane stress state, a biaxial stress state is realized in the X-ray method for studying residual stresses. It should be noted that in this case the main plane of the deformation ellipsoid coincides with the sample surface, which means that the coordinate axes also coincide. As a result, the following equation holds for the biaxial stress relation (Gladkikh et al., 2006):

$$\varepsilon_{\psi,\varphi} = \frac{1+\nu}{E}\sigma_\varphi sin^2\psi + \varepsilon_3 \quad (7)$$

where $\varepsilon\psi_{,\varphi}$ – deformation in the direction specified by the angles ψ and φ, along which it is measured (Figure 5); ν – Poisson's ratio; $\sigma\varphi$ – stress in the direction of the angle φ; E – Young's modulus.

For equation (7), there should be a linear relationship between the measured strain and $\sin2\psi$. When using X-ray analysis of residual macro-stresses, the interplanar distance of a family of crystallographic planes (hkl) is used as a scale in determining the deformation. Then the quantities $\varepsilon\psi,\varphi$ and ε_3 can be represented as (Gladkikh et al., 2006):

$$\varepsilon_3 = \frac{d_3 - d_0}{d_0} = \frac{d_\perp - d_0}{d_0} \quad (8)$$

$$\varepsilon_{\psi,\varphi} = \frac{d_{\psi,\varphi} - d_0}{d_0} \quad (9)$$

Figure 5. Geometry of diffraction in the X-ray method for determining macro-stresses: N – normal to the sample surface; σ_1, σ_2 – main voltages; ε_1, ε_2, ε_3 – main deformations; s_0, s_1 – primary and reflected beams

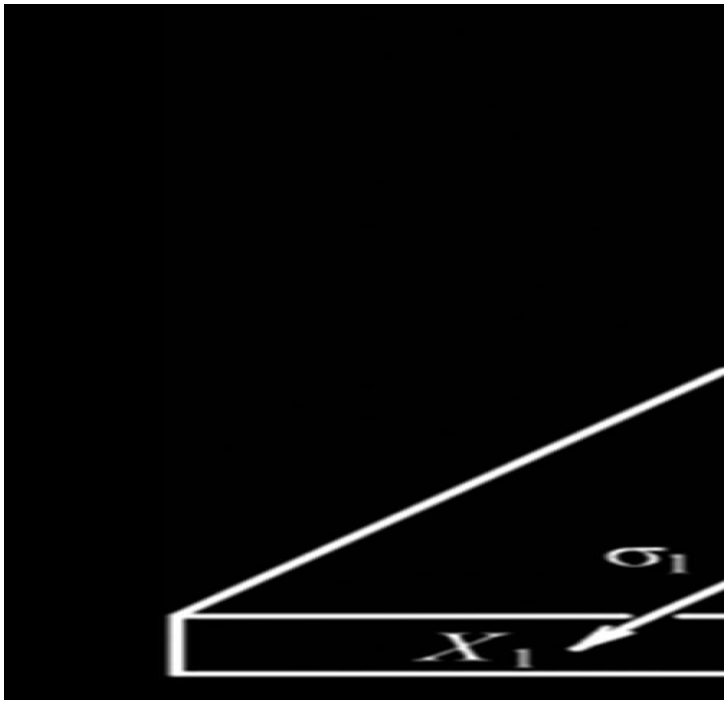

where d0 – is the interplanar distance of the planes (hkl) *i*n the unstressed state; d3 ($d_\perp$) – is the interplanar distance in the direction of the normal to the sample surface (ψ=0); dψ,φ – interplanar distance of planes (hkl) *in* a stressed state. Taking into account relations (8) and (9), equation (7) takes the form:

$$\frac{d_{\psi,\varphi}-d_0}{d_0}=\frac{1+\upsilon}{E}\sigma_\varphi sin^2\psi+\frac{d_\perp-d_0}{d_0} \tag{10}$$

Equation (10) is the main relation of the sin2ψ method. To improve the measurement accuracy, it is necessary to carry out several surveys at different angles ψ. As a result, equation (10) can be rewritten as:

$$\frac{d_{\psi_i}-d_0}{d_0}=\frac{1+\upsilon}{E}\sigma_\varphi sin^2\psi_i+\frac{d_\perp-d_0}{d_0} \tag{11}$$

where $\sigma\varphi$ defined as:

$$\sigma_\varphi=\sigma_1 cos^2\varphi+\sigma_2 sin^2\varphi \tag{12}$$

Based on equation (12), the radiographic method allows you to determine the stresses separately σ_1 and σ_2, so when $\varphi = 0°$ $\sigma_\varphi = \sigma_1$, by $\varphi = 90°$ $\sigma_\varphi = \sigma_2$. As a result, the linear dependence of $\frac{d_{\psi_i} - d_0}{d_0}$ from is a *sin²ψ-* graph. The component of normal stresses σ_φ is found from the angle of inclination of the *sin²ψ-* graph according to the ratio (Gladkikh et al., 2006):

$$\sigma_\varphi = \frac{E}{1+\mu} tg\alpha \tag{13}$$

One of the most promising and most significant methods for studying the defect structure of solids is the positron annihilation method (Pogrebnyak et al., 2012). To analyse defects of the vacancy type in the coating, we used a slow positron microbeam (SPB) from Halle, Germany, which was used to measure the S-parameter depending on the energy of the incident positron beam (up to 30 keV), i.e. from the depth of analysis. To study structural vacancies, the method of positron annihilation was used, namely, the method of Doppler broadening of the gamma-ray line. The Doppler broadening spectrum can be quantified using the characteristic S-parameter of the line shape. This parameter is the ratio of the area of the central part of the spectrum with low momentum (A_s) to the area over the entire curve (A_0) (Pogrebnyak et al., 2012).

2.2.4. Methods of Investigation of Mechanical and Tribological Properties of Coatings

Hardness, along with fatigue strength and wear resistance, is one of the most widely used mechanical characteristics of metals and alloys. At the same time, the hardness test differs from other methods for determining the mechanical properties of materials by its high sensitivity and short test time. It is carried out without destroying samples, requires a minimum of costs in their preparation.

The study of the hardness of nitride coatings based on (Zr-Ti-Nb)N, (Zr-Ti-Cr-Nb)N and (Zr-Ti-Cr-Nb-Si)N was carried out using microhardmeters manufactured by "CSM Systems AG" (Switzerland). The microhardness value was determined using the Oliver-Pharr technique (Oliver & Pharr, 1992). Measurement of Vickers microhardness was carried out using a digital automated microhardness tester "DM8-B" and "Durascan-20" by the method of pressing a tetrahedral pyramid into the sample (see Figure 6). The loads used in the measurement were 0.05–1 N. The exposure of all samples under load was 10 s. At least 10 measurements were carried out on each sample. The value of microhardness was determined by the formula (14) (Geller & Rakhshadt, 1989):

$$H = 1.854 \cdot \frac{P}{d^2} \tag{14}$$

where P – load; *d* – arithmetic mean of the length of both diagonals of the imprint after unloading, mm. The microhardness values varied in a certain range due to the internal heterogeneity of the coatings (see Figure 6). The method is used to determine the hardness of parts of small thickness and thin surface layers having high hardness. The thinner the material, the less the load should be. The Vickers hardness

Figure 6. Traces of a diamond tip on the surface of nitride coatings (Zr-Ti-Cr-Nb)N

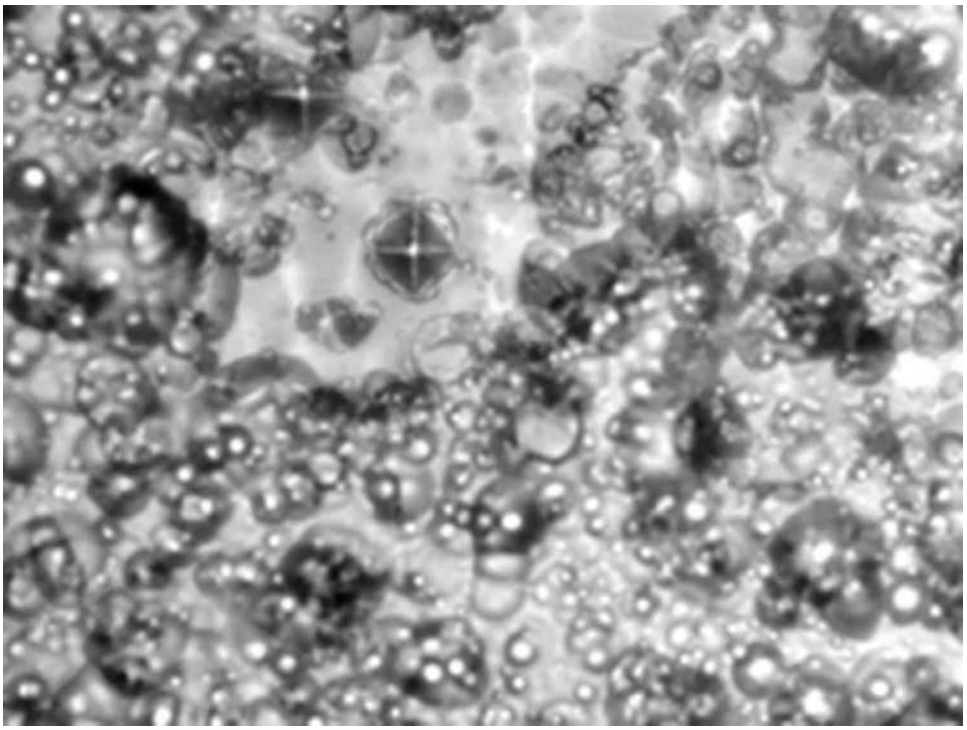

number *HV* is determined by special tables according to the measured value d (diagonal of the print in millimetres).

Additionally, the surface of the coatings was tested for nanohardness based on the use of a triangular pyramid (Berkovich's triangular pyramidal indenter). It avoids the problem of reducing four faces to one point, characteristic of Vickers indentors, and to obtain a radius of rounding of the vertex less than 100 nm. Probing with a pyramidal indenter leads to the fact that, unlike macro-tests, the deformable volume of the sample does not remain unchanged during loading but grows by many orders of magnitude. In addition, this method makes it possible to study physical and mechanical properties in nanoscale and even at the atomic level, which is not available to conventional mechanical testing technologies (Golovin, 2008). Nanohardness measurements were carried out by a diamond triangular Berkovich indenter on the "Hysitron TI 950 TriboIndenter/Nanoindenter" nanohardometer using the Oliver and Far technique (Oliver & Pharr, 1992). The maximum load was 10,000 μN. With the help of a computer program, test parameters are set – load, loading speed, holding time, unloading speed. During the tests, the dependence of the indenter vertex movement on the load was recorded with high accuracy using a capacitive sensor (Figure 7).

The device contains a loading unit of 1 m, a precision sensor 2 for registering the movement of the indenter 3 on soft springs 4, structurally combined into one measuring head 5, a controller unit 6 and a computer 7 with a software package for controlling all operating cycles of the device, collecting, processing and storing data. An optical microscope is used to select the injection site, and a two– or three-coordinate table 9 is used for positioning and moving the sample 8. In the most advanced devices, the table is motorized and also controlled by a computer. The set of nodes, their functions and relationships

Figure 7. Block diagram of nanoindentation and scratch testing: a – nanoindometer device, 1 – power cell; 2 – sensor for registering the movement of a movable rod with an indenter (3); 4 – rod suspension springs; 5 – measuring head housing; 6 – controller unit; 7 – computer; 8 – sample; 9 – slide table; b – atomic force microscope, 5 – measuring head housing; 6 – controller unit; 7 – computer; 8 – sample; 9 – slide table; 10 – probe; 11 – piezoelectric actuator; 12 – cantilever micro-beam (quantileever); 13 – four-window photodetector (recorder of probe movements); 14 – laser

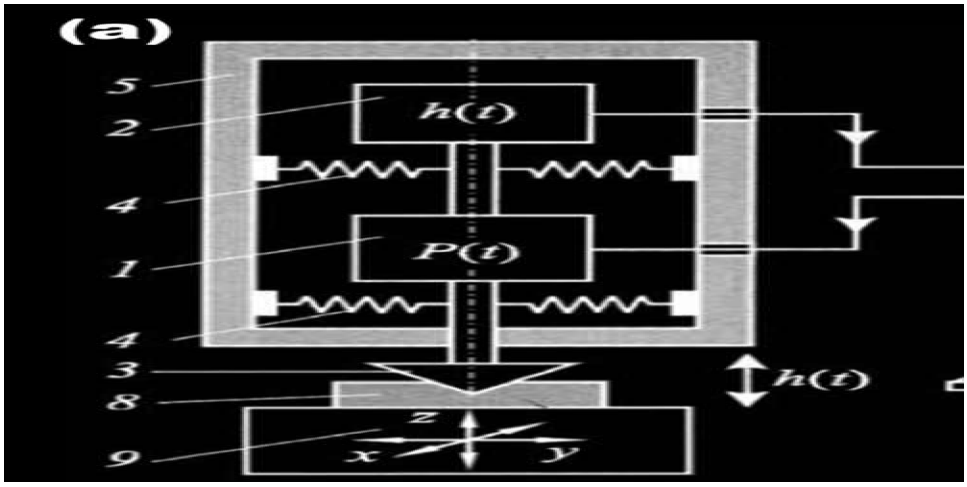

in nanoindentometers and atomic force microscopes (AFM) are similar (Figure 7b), and they developed almost in parallel and simultaneously. The resolution of the measuring path of the probe movement in them is also comparable and can be hundredths of nm. Therefore, they are often combined in one complex or even in one head, which makes it possible to expand the capabilities of probe methods and make them the most popular in modern nanotechnology. The combination of AFM and nanoindentation methods makes it possible to carry out 2D studies of the surface in normal and lateral modes and 3D characterization of mechanical properties at a given depth (from units to thousands of nm).

Figure 8 shows a general view of the nanohardometer "Hysitron TI 950 TriboIndenter/Nanoindenter". In indentation studies, a kinetic diagram is recorded, and at the same time the hardness and Young's modulus are determined, and their ratio allows you to compare the relative hardness of different materials, including in different structural states. This method makes it possible to study the micromechanical behaviour and structural sensitivity of the mechanical properties of thin near-surface layers. The sensor is formed by two glass plates located at a distance of 200 microns from each other.

The third plate is fixed on the rod of the indenter. When the depth of the print changes, the sensor capacity changes, which allows you to continuously monitor the movement of the top of the indenter. A triangular Berkovich indenter is fixed at the lower end of the rod, and an inductor is located at the upper end. The coil is placed in a permanent magnet, while when a current is passed through the inductor, the rod with the indenter is pushed out of the magnet and a load is applied to the indenter. In the range from 0 to 150 mN, the connection between current and load is linear, which allows you to control the force applied to the indenter. During the tests, the device allows you to record three parameters – the load, the movement of the top of the indenter and the time. During the tests, the dependence of the movement of the vertex of the Berkovich indenter on the load was recorded with high accuracy. The accuracy of

Figure 8. Optical, scanning probe microscopy and instrumental indentation: a – appearance; b – measuring techniques

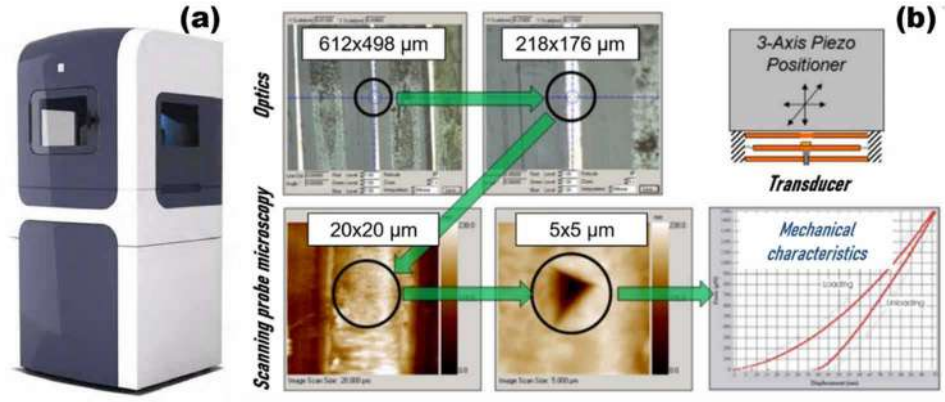

measuring the depth of the print is ± 0.04 nm, the load on the indenter is ± 75 nN. The device performs about three load and displacement measurements in 1 second. To reduce vibrations, the device is mounted on a vibration-isolating table. The rate of introduction of the indenter is 5 nm/s. During each test, the indenter was loaded/unloaded three times, each time for a higher load, which did not exceed 10 mN at a depth of 150 nm. To reduce the temperature difference between the sample and the indenter, the sample is placed in the device for 12 hours before the start of the tests. The room temperature is kept constant with an accuracy of ± 0.5 C. The tests do not start if the thermal expansion rate of the indenter rod is higher than 0.05 nm/s. During unloading, for each test, the rate of thermal expansion of the indenter was measured again and as a result, an appropriate correction was made. When an indenter is introduced near the contact area, a complex stress state is created, close to comprehensive compression, and the deformation spreading deep into the material has both elastic (reversible) and plastic (irreversible) components. Due to this, during nanoindentation, it is possible to obtain information about both hardness and Young's modulus, as well as to estimate the proportion of the elastic component in the total deformation or elastic recovery. Figure 9 shows a typical experimental curve of continuous indentation, the dependence of the load on the depth of indentation. The value of the elastic recovery W_e of the surface layer was calculated by the curves "loading – unloading" according to the formula (15):

$$W_e = \frac{h_{max} - h_r}{h_{max}} \tag{15}$$

where h_{max} - maximum penetration depth; h_r - the residual depth after removing the load, which consists in selecting the parameters of a power function describing the experimental dependence of the loading depth on the applied load, and calculating the hardness and Young's modulus from these data. The hardness value was calculated as the ratio of the maximum load to the projection area of the unrecoverable print, and the modulus of elasticity was calculated based on the projection area of the print, contact stiffness, defined as the slope of the upper third of the loading curve, and the specified Poisson's ratio.

To determine the tribotechnical characteristics, a universal "SMC-2" installation was used. The obtained coatings and uncoated samples were tested for wear resistance according to the "plane cylinder"

Figure 9. Dependence of the load on the depth of indentation

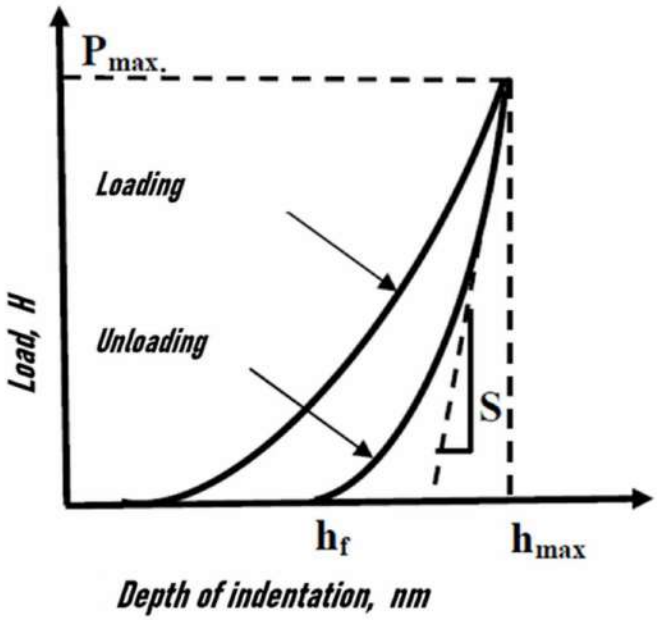

scheme using technical vaseline. During the entire test, the sample was not removed from the friction machine. The width of the groove and its length in the wear zone were carried out using a Brinell "MPB-2" microscope, which provides measurement accuracy of ± 0.025 mm. The coefficient of friction and the wear rate of nitride coatings and counterbody were determined at different temperatures on an automated friction machine (PC-Operated High-Temperature Tribometer, CSM Instruments, Switzerland), in air according to the "ball-disc" scheme (Figure 10). The coatings were applied to discs made of 45 steel (HRC = 55) with a diameter of d = 50 mm and a thickness of h = 5 mm. The load during the tests was 3.0 N, and the sliding speed was 10 cm/s. The sample was installed in a holder, a rod was fixed perpendicular to the sample plane, at the end of which there was a ceramic ball with a diameter of 6 mm made of Al_2O_3, SiN, SiC. By adjusting the displacement sensor, the wear radius of curvature was selected, another sensor compensated for the friction force and allowed the value of the friction coefficient to be set at a certain point in time.

In the course of the study, the analysis of wear products, as well as the contact area on the counterbody, was carried out by examining the structures of wear grooves on the surface of the coatings under study, as well as changes in wear spots on the ball. Measurements of the vertical section of the wear grooves were carried out on a profilometer in four diametrically and orthogonally opposite areas, after which the average value of the groove depth and cross-sectional area was calculated. The sample is in the form of a disk with a hardened surface (coating), rotates at a given frequency in the heating zone. The counterbody in the form of a certified ball is fixed immobile in the holder, which transmits a given load to it and is connected to the sensors of the friction force and the depth of immersion of the counterbody. Such a contact scheme also allows for the mathematical calculation of the initial contact stresses (Hertz stresses). The tests are carried out according to ASTM G99-959 and DIN50324 standards. The following temperatures were selected as temperatures for tribotechnical tests: 300°C and 500°C.

Figure 10. Scheme of testing samples of nitride coatings for wear resistance using the "ball-disc" method

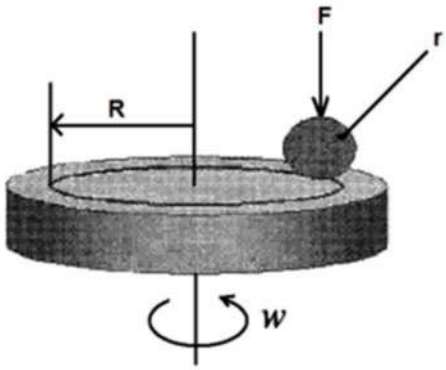

The surface profile was measured using a "Surtronic 25" profilometer device by measuring the vertical deflection of a diamond tip (probe) moving at a constant speed under conditions of mechanical contact with the sample. Surtronic-25 has a multifunctional RS-232 port, with which it is possible to transfer data to a printer for printing or to a computer for subsequent analysis using additional Talyprofile software. The software allows you to calculate parameters, set calculation modes in full compliance with international standards. Special functions allow you to get a vertical/horizontal reflection of the profile, enlarge individual sections for a more detailed examination, get an inverted profile, and also calculate the undulation and roughness separately. The structure of the coating wear grooves and wear spots on the balls were studied using an Olympus GX 51 optical inverted microscope and a Quanta 200 3D scanning ion electron microscope. As a result of the tests, the wear factor (Vershinin et al., 2010) of the coated sample and the statistical partner (ball) were evaluated according to the method (Randall, 2002):

$$W = \frac{V}{Pl} \tag{16}$$

where W – wear factor [mm^3/H·m]; V – volume of removed material [mm^3]; P – load [N]; l – friction path [m]. The wear diameter of the ball was determined using an "Olympus GX 71" optical inverted microscope, the volume of the removed material on the ball was calculated as

$$V_{\varnothing} = \pi h^2 \left(r - \frac{1}{3} h \right) \tag{17}$$

where $h = r - \sqrt{r^2 - \left(d/2\right)^2}$ segment height; d – wear diameter; r – ball radius. The volume of removed coating material is equal to $V_п = s l_п$, where $l_п$ circumference, s – wear track cross-sectional area.

The study of adhesive-cohesive strength, scratch resistance and determination of the mechanism of destruction of the coating were carried out using the "REVETEST" scratch tester (CSM Instruments). Scratches were applied to the surface with a diamond spherical indenter of the "Rockwell C" type with

Figure 11. Scheme and appearance of the scratch tester

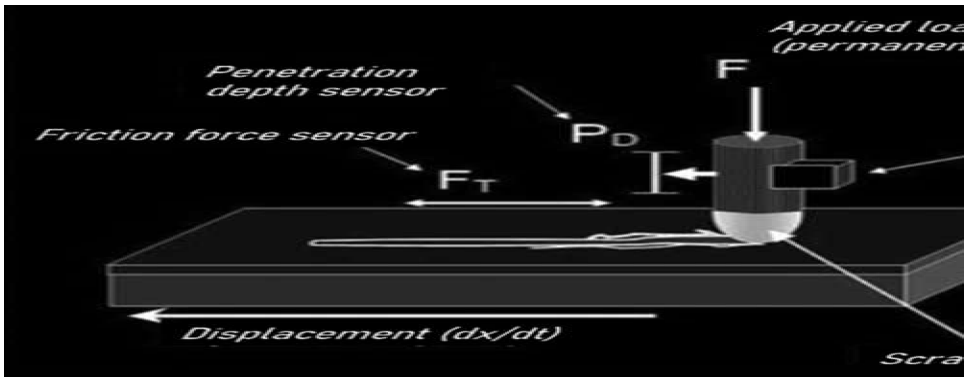

a radius of 200 microns with a continuously increasing load (Figure 11), after which physical parameters were recorded: acoustic emission, coefficient of friction and depth of penetration of the indenter.

The tests were carried out under the following conditions: the load on the indenter was increased from 0.9 to 70 N, the speed - 1 mm/min, the scratch length - 5 mm, the loading speed - 6.91 N/min, the signal sampling rate - 60, the acoustic emission - 9. The registration of various parameters during the testing process made it possible to fix the stages of coating destruction. During the movement of the indenter at a given speed and with a continuously increasing load, the readings of several sensors are recorded on the computer, namely: loading force, acoustic emission intensity, friction force, friction coefficient, scratch depth. The moment of adhesive or cohesive destruction of the coating is recorded after testing visually using an optical microscope equipped with a digital camera, as well as by analysing the shape of the "property-load" curves, by changing one of five parameters: acoustic emission, friction force, friction coefficient, indenter penetration depth and residual scratch depth. The data is stored on the hard disk of the control computer. The combination of various parameters recorded during the testing process increases the reliability of the methodology and the accuracy of determining the critical load. Additional advantages of the scratch testing method include the ability to study the type of material failure (cohesive or adhesive) and evaluate the crack resistance of materials. The sclerometric head includes a device for measuring the normal and tangential load on the indenter (a diamond pyramid of the "Rockwell C" type) when scratching, a device for measuring the magnitude of the normal movement of the indenter, a device for lifting and lowering the head, a device for lifting and lowering the indenter, a drive for moving the indenter in the tangential direction. The loading of the indenter is provided by a spring squeezed by a screw mechanism. In this case, the spring presses on the indenter through a dynamometric semicircle with a load cell to measure the load applied to the indenter. The loaded indenter is lowered and embedded in the surface. The movement and speed of the indenter insertion is measured by an inductive sensor. The scratch resistance force is measured using strain gauges.

During the test, a scratch is formed not only due to the destruction of the material, but also as a result of plastic deformation. The process of material deformation by a diamond indenter consists of the following main stages:

- preliminary incline during vertical insertion of the indenter to a given depth;

- the introduction of a rigid indenter into a solid leads to the appearance of a characteristic "crown" at the base of the print;
- at the initial moment of the scratch formation, the subsequent deformation of the riveted material occurs, caused by the movement of the lateral surface of the pyramid;
- a slice of the "crown" of the main print is transformed into an influx;
- with further movement ahead of the indenter, the influx increases and reaches the maximum height with maximum scratching force.

At this moment, local destruction of the material occurs at the tip of the influx, resulting in a reduced scratching force. As a result of the tests, it is possible to determine the minimum (critical) load (L_C), which leads to the destruction of the coating. It should be noted that not all recorded events related to the destruction of the coating describe the actual adhesion of the coating to the substrate. By changing the values of the coefficient of friction and the acoustic emission signal with an increase in the scribing load, the characteristic values of the critical load L_C were determined: The critical load responsible for the moment of the appearance of the first chevron cracks in the lower part of the scratches was determined as L_{C1}; L_{C2} – the time of the appearance of multiple chevron cracks in the lower part of the scratches; L_{C3} – when the destruction has an adhesive-cohesive character; L_{C4} – local peeling of the coating areas; L_{C5} – plastic abrasion of the coating on the substrate, loss of adhesion strength. The combination of various parameters recorded during the testing process increases the reliability of the methodology and the accuracy of determining the critical load. This technique complies with the international standard ISO DIS 20502.

Conclusions for Section 2

1. Based on the literature sources, the expediency of choosing the elements Ti, Zr, Cr, Nb, and Si as components of the nitride coating was determined.
2. Taking into account the features of the constituent elements, the optimal physical parameters were selected when using the method of vacuum-arc deposition of nitride coatings based on (Zr-Ti-Nb), (Zr-Ti-Nb-Cr) and (Zr-Ti-Nb-Cr-Si).
3. A set of complementary research methods has been selected that allows analysing the change in the morphology of the coating surface, the elemental composition and its redistribution in depth, structural and phase transformations depending on the deposition modes (change in bias voltage and pressure of working gas).
4. To determine the physical and mechanical properties, a technique has been developed for determining microhardness and nanohardness, as well as testing protective coatings for physical, mechanical and tribological tests.

3. INFLUENCE OF DEPOSITION PARAMETERS AND DOPING PROCESS ON THE ELEMENTAL AND PHASE COMPOSITION OF MULTICOMPONENT COATINGS

3.1. Morphology and Elemental Composition of the Surface of the Investigated Coatings of the System (Zr-Ti-Nb)N, (Zr-Ti-Nb-Cr)N and (Zr-Ti-Nb-Cr-Si)N

A review of the literature has shown that ion-vacuum coating technologies are the most promising (Thornton, 1982). Nitride multicomponent coatings obtained by magnetron sputtering have an amorphous structure (in the absence of nitrogen). With the addition of reaction gas (Ar+N), the structure of the coating changes from amorphous to crystalline (FCC lattice of the NaCl type).

A characteristic feature of the coatings obtained by vacuum arc deposition is the presence of a preferred orientation and high compressive stresses. The phase composition and structural state of coatings obtained by vacuum arc deposition vary widely depending on the ion energy of the deposited flow and the pressure of the working gas. At the same time, the presence of nonequilibrium condensation conditions (the influence of impurities, the radiation effect of the deposited flow, etc.) determines the metastability of the properties of the coatings obtained (Azarenkov et al., 2012). Thus, changing the energy of the deposited particles allows you to adjust the level of residual compressive stresses and the size of the crystallites. Adjusting the pressure of the working gas (nitrogen) provides a wide variation of the microstructure by changing the stress-strain state, grain size, crystallographic orientation, etc.

The chemical composition and morphology of the coatings were studied using the PEGASUS X-ray energy dispersive spectrometric system, scanning electron microscopy/energy dispersive X-ray spectroscopy (SEM/EDX) JEOL JSM-6610 LV and JEOL 7001TTLS with a voltage of 15-20 kV. The chemical bond state of the coatings was analysed by X-ray photoelectron spectroscopy (XPS, EC 2401) using MgK_{α} radiation (E = 1253.6 eV). Before XPS measurements, the samples were etched by sputtering in argon plasma for 5 min. According to the results of scanning electron microscopy, vacuum-arc condensation of a multicomponent system has a number of features in the formation of surface morphology.

Figures 12 and 13 show images of the coating surface (Zr-Ti-Nb)N. The study of surface morphology showed that deposition of coatings leads to an increase in surface roughness (from 0.09 to 0.42 μm) due to the droplet component of the plasma flow. Figure 12b clearly shows the presence of a clear boundary between the coating and the substrate without transition layers. The thickness of the coating (Zr-Ti-Nb)N is d » 6.7-10 μm, which is typical for nitride coatings obtained by vacuum-arc deposition. In the cross-sectional image in Figure 13, the coating showed a columnar structure, which is characterized for materials obtained by deposition in a vacuum arc. It should be noted that there are small voids and gaps in the columns. The concentration of various elements in the coatings (Zr-Ti-Nb)N, (Zr-Ti-Nb-Cr)N and (Zr-Ti-Nb-Cr-Si)N at different deposition parameters is shown in Table 3. The content of elements in all coatings was close to the concentration of elements in the sprayed target.

Figure 14 shows a SEM image of one of the obtained coatings of the system (Ti-Zr-Cr-Nb)N. The main difference between vacuum arc deposition, in particular, in the cathode spot arc mode, is the production of molten droplets that can be incorporated into the coating in the form of microparticles. As can be seen from Figure 14, the coating (Ti-Zr-Cr-Nb)N contains inclusions of droplet fractions of various sizes (up to 10 μm in diameter). In our case, the microdroplets have the shape of an ellipsoid, which indicates that the droplets fly almost parallel to the plane of the substrate. An increase in the temperature of the deposition flow using a bias voltage (U_C = -200 V) significantly reduces the con-

Figure 12. SEM-images of coatings based on (Zr-Ti-Nb)N at P_N=0.5 Pa: a – surface morphology; b – cross-section of coatings

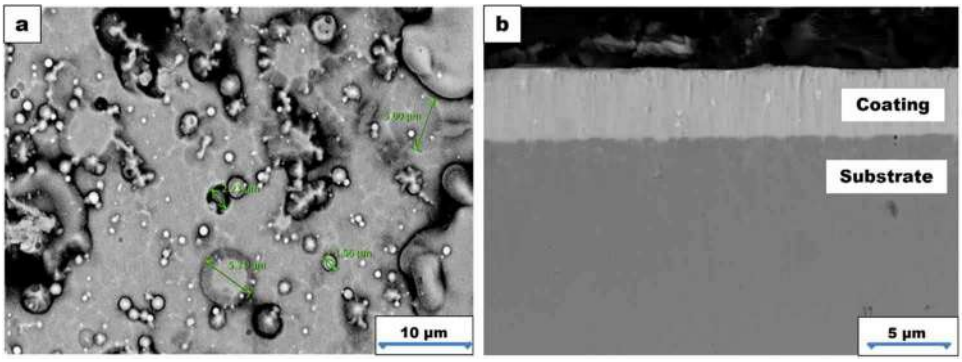

Figure 13. SEM-images of crack structures of (Ti-Zr-Nb)N coatings obtained at P_N = 0.5 Pa: coating fracture fractogram and magnified view (columnar structure)

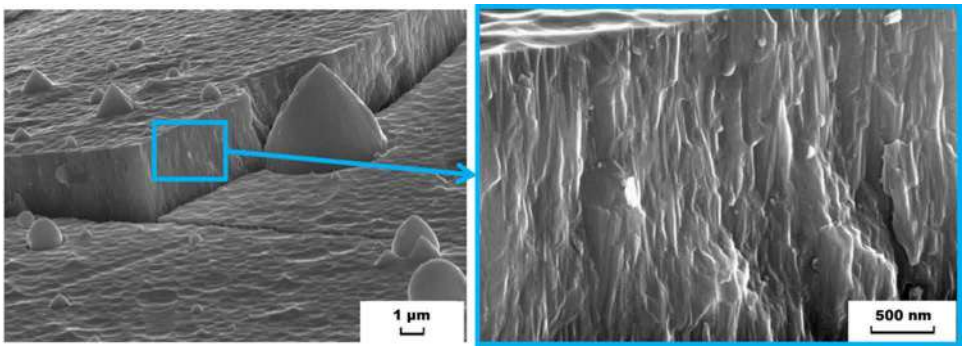

centration of the droplet fraction on the surface (Figure 14b). A reduced droplet content may occur as a result of melting processes on the coating surface. It is likely that focusing a beam of charged particles activates the process of cleaning the surface from smaller fractions, and its heating allows the formation of a homogeneous protective layer.

As morphological studies show (Figure 14b), the obtained at higher values of the displacement potential and the pressure of the working gas is a fairly flat surface with minimal droplet presence, whereas the use of reduced values of physical deposition parameters leads to the formation of micron-sized droplets of molten material on the surface (Figure 14a). According to the work (Boxman & Zhitomirsky,), the use of high pressure of the working gas contributes to the activation of the formation of chemical compounds on the cathode surface, and the content of droplets in the plasma stream depends on the thermophysical properties of the cathode, namely, on the melting temperature. As a result of the entry of a chemically active gas into the chamber, a nitride layer of constituent elements forms on the cathode surface (they often have a high melting point), which leads to a decrease in its erosion in the droplet phase. The reduction of the droplet component in the coating can also be achieved by increasing the energy of the sprayed ions. Thus, with an increase in the displacement potential of the substrate, the condensation

Figure 14. SEM-images of the surface of (Zr-Ti-Cr-Nb)N coatings: a – PN = 0.3 Pa, UC = -100 V; b – PN = 0.7 Pa, UC = -200 V

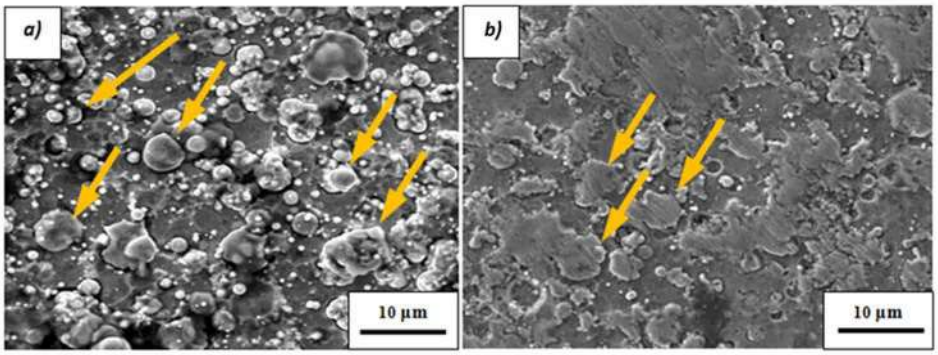

Figure 15. SEM/EDX integral elemental composition of (Zr-Ti-Cr-Nb)N coatings

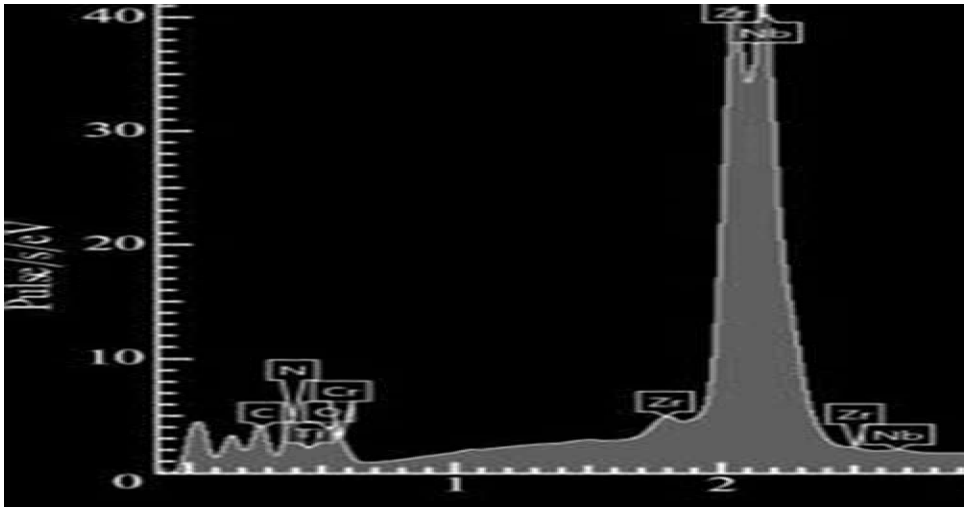

surface temperature increases, which leads to partial melting of small droplets. As a result, the number of droplets decreases due to spraying with high-energy ions, as well as due to evaporation processes.

Integral element analysis showed that the matrix of the near-surface area of the coating consists of Zr, Ti, Cr and Nb (Figure 15 and Table 3). The presence of nitrogen peaks in the spectra is associated with the composition of the gas atmosphere of the vacuum-arc source.

The high carbon content on the sample surface can be explained by the difficulty in recognizing elements such as C, N, O by energy dispersive X-ray spectroscopy due to the similarity of their electronic structure. By calculating the energy E of the K_{α} radiation for some elements, determining the difference between them and comparing them with the resolution of the analyser, it is possible to draw conclusions about the accuracy of the results obtained. It follows from Moseley ‘s law:

$$E=10,2eV\bullet(Z-1)^2 \quad (18)$$

$$\Delta E = 10,2eV \cdot \left(\left(Z_A - 1 \right)^2 - \left(Z_B - 1 \right)^2 \right) = 10,2eV \cdot \left(Z_A + Z_B - 2 \right) \left(Z_A - Z_B \right) \quad (19)$$

where Z – the ordinal number of an atom in the periodic table of chemical elements of Mendeleev. According to calculations, the difference between the radiation energies ΔE when determining an element using energy-dispersive X-ray spectroscopy is 112.2 eV for C and N, 132.6 eV for N and O, 805.8 eV for Zr and Nb. Since the difference between the radiation energies from elements C, N and N, O is less than the resolution of the analyser, it is impossible to accurately determine the ratio between these elements in the coating. It is likely that oxygen is practically absent in the coating, and the processes of diffusion of oxygen atoms into the surface composition from the air atmosphere can be considered the reason for its appearance on the spectrum. The nitrogen concentration should be slightly higher due to a decrease in the carbon concentration.

Based on the heterogeneous contrast of inclusions on the SEM-images of the surface (Figure 14), the droplet fractions have different elemental composition in stoichiometry. According to the obtained maps of the distribution of elements (Figure 16), the basis of these inclusions are zirconium, niobium and nitrogen. Note also that Nb and Zr practically duplicate their location on the map of elements and, basically, make up a matrix of inclusions of droplet fractions. The reason for this distribution is the high melting point of both elements and the almost identical work of the electron output from the metal surface (A_{out}(Nb) = 3.99 eV, A_{out}(Zr) = 3.96–4.16 eV). According to calculations, the difference in the radiation energies of zirconium and niobium is several times greater than the resolution threshold of the EDS analyser, which makes it possible to accurately recognize the mentioned elements. Therefore, the presence of droplet fractions from Nb and Zr is quite possible (light balls in Figure 14a). Titanium and nitrogen have an equally uniform distribution over the entire surface of the coating (Figure 16), and the chromium concentration is significantly lower in areas where niobium predominates. It is also seen that

Figure 16. SEM/EDX-maps of the distribution elements on the surface of the sample series 1

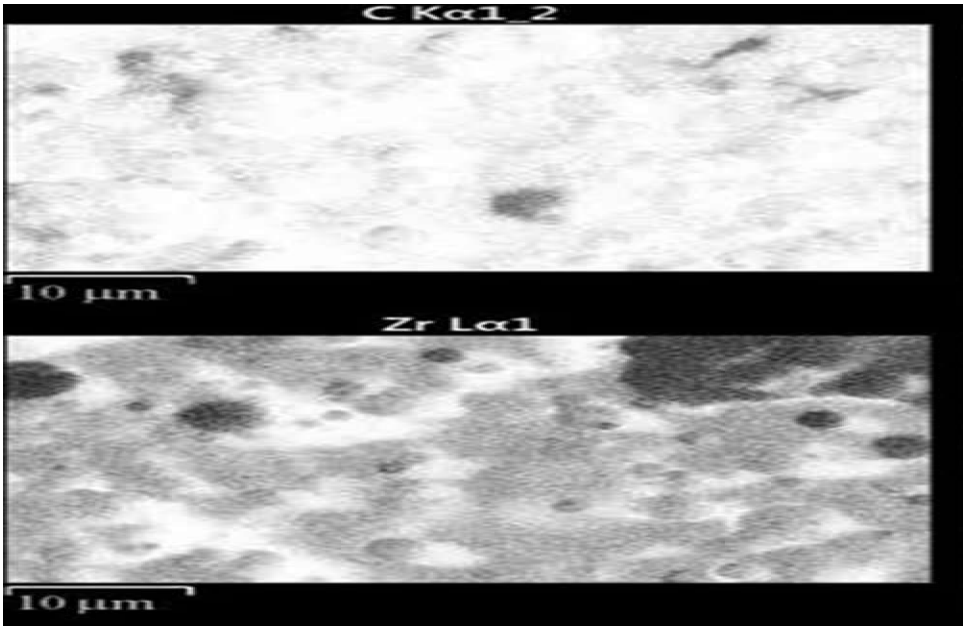

the distribution of carbon does not repeat the distribution of nitrogen over the entire surface, therefore, this is not a measurement error.

In all obtained coatings, the nature of the distribution of elements over concentrations in the surface composition has a similar pattern $C_N > C_{Cr} > C_{Ti} > C_{Zr} > C_{Nb} > C_C/C_O$. This is clearly illustrated by the pie charts presented in Figure 17. We also note that an increase in the bias voltage to –200 V leads to a noticeable decrease in the concentration of titanium and chromium atoms in the surface composition. This means that in the process of coating deposition, particles of the coating surface with the lowest atomic mass are sputtered.

From the graphs shown in Figure 18, it can be seen that an increase in nitrogen pressure in the chamber from 0.3 to 0.7 Pa leads to a decrease in the carbon concentration in the surface composition and an increase in the concentration of nitrogen, niobium and zirconium atoms. The same was observed with an increase in the negative potential of the substrate from -100 to -200 V (table 3).

The chemical bonding state and elemental composition of the (Zr-Ti-Cr-Nb)N coating were examined by the XPS method (Figure 19) with peaks associated with Ti 2p, Cr 2p, Zr 3d, Nb 3d, N 1s. There was also an oxygen peak (O 1s). According to the existing data (Morris, 1998), the Ti 2p peaks at 455.8 and 458.7 eV correspond to the Ti-O and Ti-N bonds, respectively; Cr 2p peak at 576.1 eV to the Cr-N bond; Zr 3d at 180.1 eV and 182.2 eV to Zr-N and Zr-O bonds respectively; Nb 3d at 203.8 eV and 207.5 eV,

Figure 17. SEM/EDX-elemental composition of (Zr-Ti-Cr-Nb)N coatings: a – series (sample) 1; b – series (sample) 2; c – series (sample) 3; d – series (sample) 4

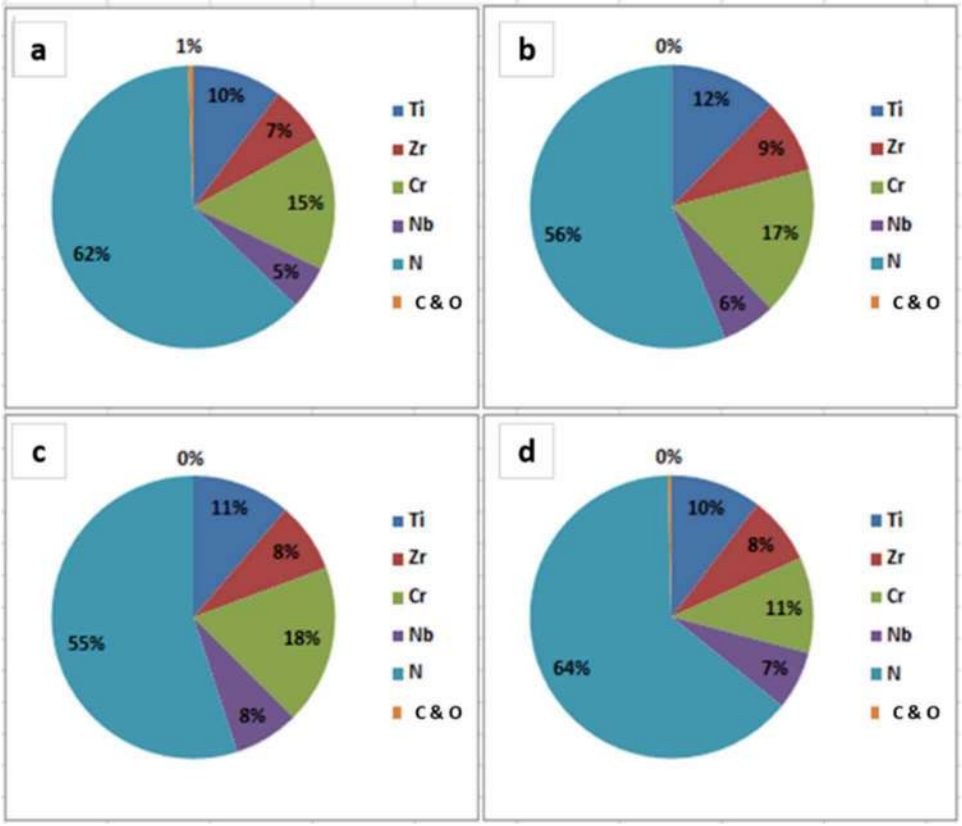

Figure 18. Change in the concentration of elements in (Zr-Ti-Cr-Nb)N coatings depending on the deposition parameters: a – P_N = 0.3 Pa; b – U_b = -100 V

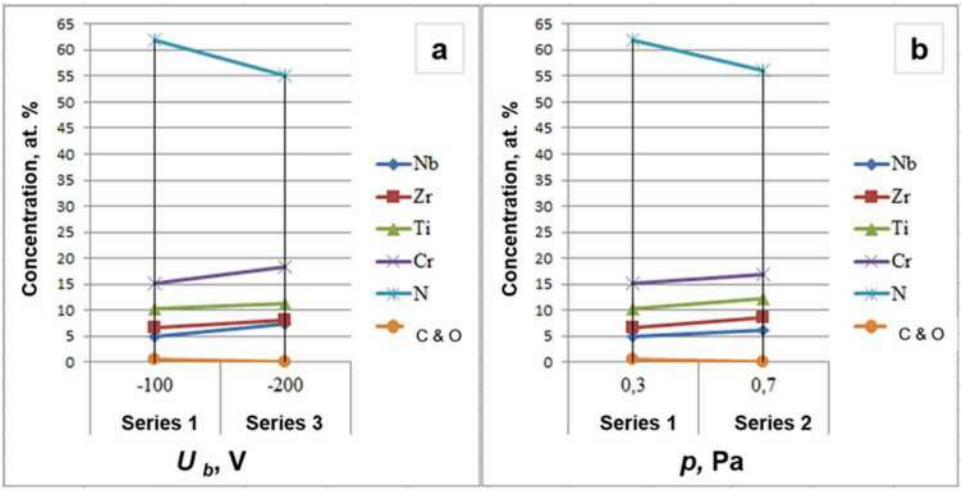

Table 3. Elemental analysis of (Zr-Ti-Nb)N, (Zr-Ti-Cr-Nb)N and (Zr-Ti-Cr-Nb-Si)N coatings

Series (Sample) Nº	Concentration, at.%						
	Ti	Zr	Cr	Nb	N	Si	Impurities (C and O)
(Zr-Ti-Nb) N							
1	20.91	20.38	-	19.99	39.00	-	-
2	20.52	19.36	-	19.26	41.00	-	-
(Zr-Ti-Cr-Nb)N							
1	10.21	06.63	15.22	04.96	62.00	-	0.57
2	12.30	08.48	16.92	06.17	56.00	-	-
3	11.27	08.03	18.23	07.48	55.00	-	-
4	10.40	07.81	11.00	06.73	64.00	-	0.39
(Zr-Ti-Cr-Nb-Si)N							
1	34.50	11.58	11.00	03.30	37.00	02.10	-
2	32.30	13.28	07.95	03.62	40.00	03.50	-

respectively, to the Nb-N and Nb-O bonds; N 1s peak at 397.4 eV to Cr-N bonds; O 1s at 531.3 eV to Nb-O bonds. These results show that the (Zr-Ti-Cr-Nb)N coating is composed of Ti-N, Ti-O, Cr-N, Zr-N, Zr-O, Nb-N, and Nb-O bonds, which can be are attributed to the TiN, TiO_2, Cr_2N, ZrN, ZrO_2, NbN and Nb_2O_5 phases, respectively. Thus, it can be assumed that the multiphase material (Ti, Zr, Nb)N-Cr is formed in the coatings.

The results of the RBS analysis of the elemental composition of nitride coatings based on (Zr-Ti-Cr-Nb)N are shown in Figure 20. As can be seen from Figure 20a, all peaks correspond to all the constituent elements of the coating, which corresponds to the chemical composition of the sputtered cathodes. From the element distribution profiles shown in Figure 20b, it is possible to judge the homogeneous distribu-

Figure 19. XPS-peaks of the (Zr-Ti-Cr-Nb)N coating deposited at P_N = 0.3 Pa, U_b = 200 V

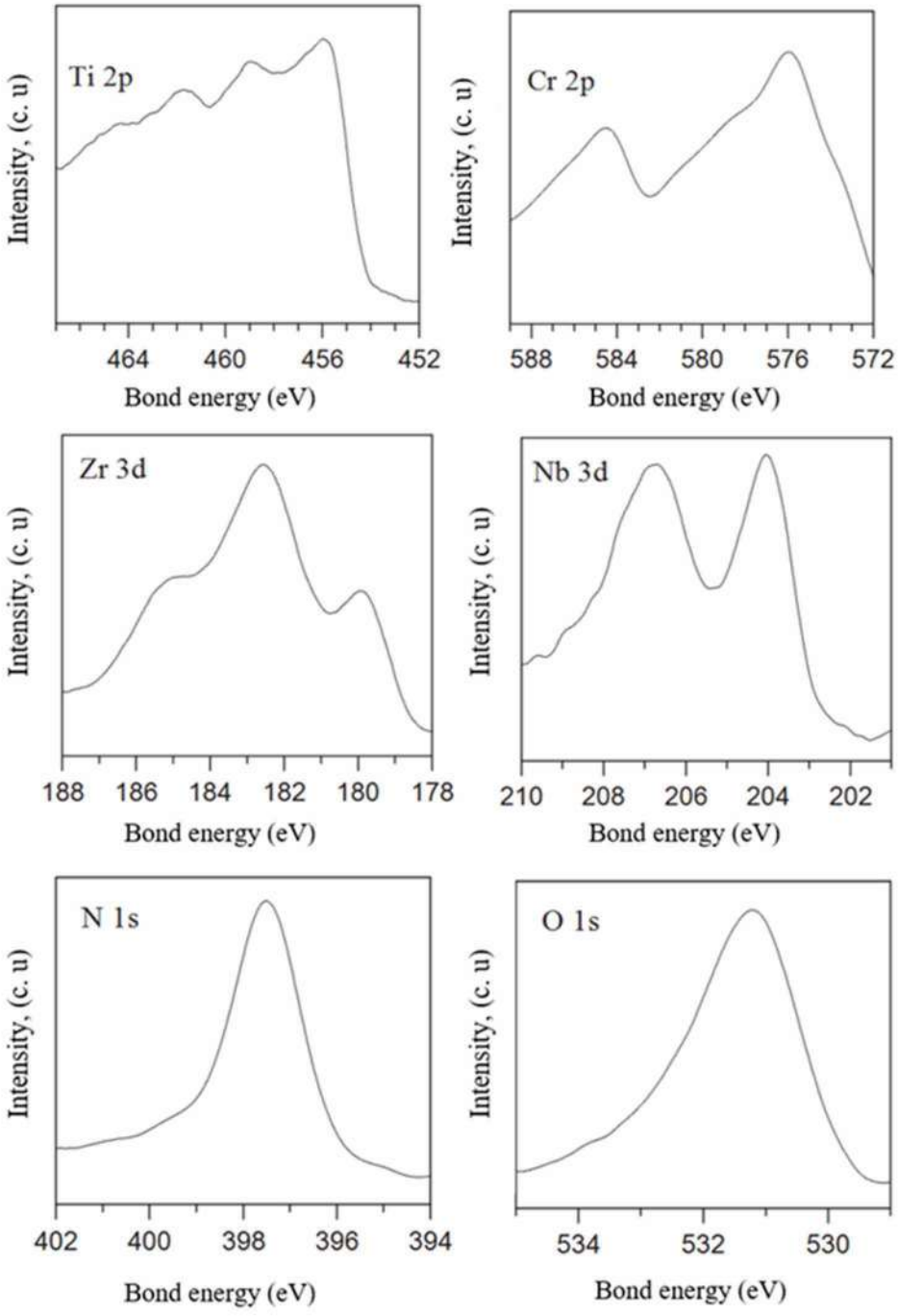

Figure 20. RBS-analysis of (Zr-Ti-Cr-Nb)N nitride coatings at P_N = 0.3 Pa and U_b = 200 V: a – energy spectrum (channeling); b – element distribution profile in depth

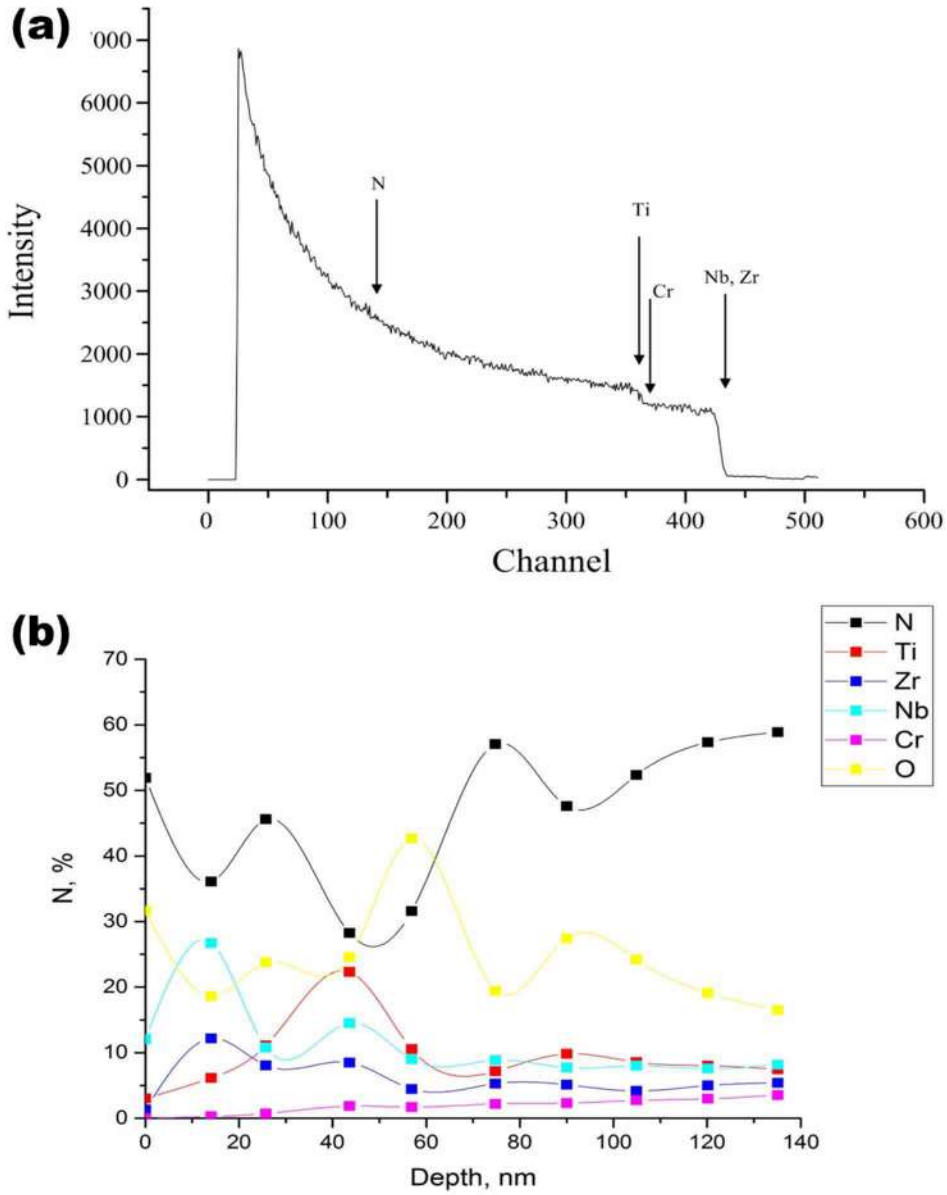

tion of the constituent elements in the near-surface layer, while the surface layer is enriched with N, O and Nb atoms, which have the highest concentration, which correlates well with the results of EDX/EDS analysis. In the case of coatings (Zr-Ti-Cr-Nb-Si)N with a high concentration of nitride-forming elements (Ti and Zr), the carbon content was controlled at a low level of about 2 at.%.

It is well known that the RBS method is a reference method for measuring the concentration of heavy elements and for determining the thickness of the coating with high accuracy (up to 0.1 nm). At the same time, peaks corresponding to light elements (N, C and O), which have a significant effect on the

properties of thin films, are almost impossible to separate from the general background of heavy elements due to the large atomic number of the substrate. In addition, as can be seen from Figure 20, the peaks corresponding to elements with a close atomic radius (located side by side in the periodic table) are superimposed on each other (Ti and Cr, Zr and Nb).

Figure 21 shows the initial state of the coating surface after deposition. The images were obtained using AFM.

The presence of micro-spherical and flat formations of various dispersity on the surface of condensed layers of titanium, chromium, zirconium, and niobium indicates the presence of a droplet phase in plasma flows emitted at high velocities from cathode spots towards the substrates. The use of a negative bias potential applied to the substrate, -100 and -200 V, affects the surface morphology of the multicomponent condensate and promotes the formation of denser layers. It is known that the efficiency of plasma-chemical reactions in the synthesis of compounds is determined, in particular, by the degree and nature of excitation of molecules, molecular ions, as well as by the ion kinetic energy E_i, which varies depending on U_b. These factors contribute to the dissociation of active gas molecules in the condensation zone and subsequent reactions of synthesis of compounds of metal and non-metal atoms. An increase in the energy of ions and fast atoms due to RF pulse technology leads to an increase in the surface diffusion mobility of atoms, causing the predominant growth of crystallites in the condensation plane, as well as to a redistribution of the components of the growing condensate (implanted atoms, vacancies, their complexes, second phases) over the depth of radiation exposure bombarding particles, as a result of which the microlayered structure of the coating is formed.

Studies of the features of the formation of the structural-phase state of multicomponent coatings based on Zr, Ti, Nb, Cr, Si and N were prepared from one evaporating Zr-Ti-Cr-Nb-Si cathode (Cr -17.08 at%, Zr - 30, 19 at%, Nb - 9.67 at%, Ti - 39.96 at%, Si - 3.1 at%). To study the features of the formation of the structural-phase state of the coatings, two series of coating samples were formed and at least five samples from each series were studied (see Figures 19 and 20).

Figures 22 and 23 show images of the coating surface (P_N = 0.3 Pa и U_b = -100 V). From which it can be seen that during the deposition process in the coating there are areas with a drop fraction up to 10 μm in size. However, no cracks were found, which indicates the good quality of the coating obtained

Figure 21. Surface morphology of the (Zr-Ti-Cr-Nb)N coating obtained using AFM: a – 2D-image; b – 3D-image

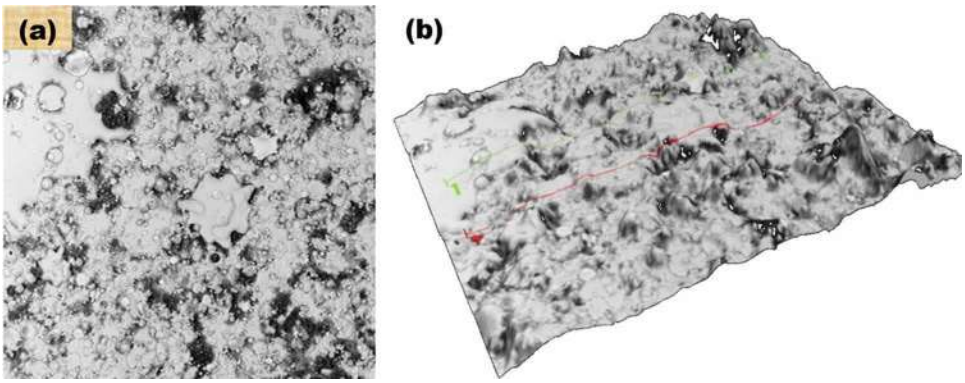

Figure 22. SEM-images of the surface morphology of coatings of the (Zr-Ti-Nb-Cr-Si)N system, obtained at P_N = 0.3 Pa and U_b = -100 V: a – general view, x2750; b – enlarged view, x6000

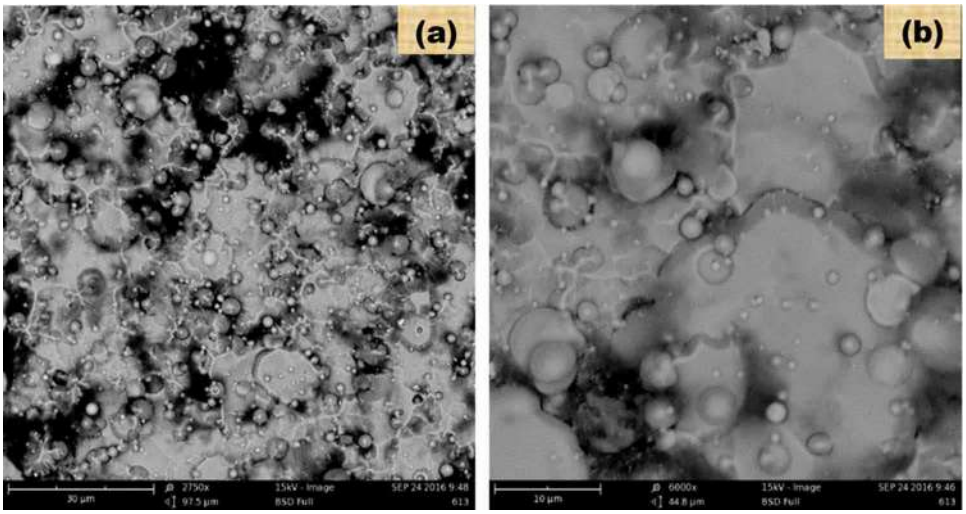

Figure 23. SEM-images of the surface morphology of coatings of the (Zr-Ti-Nb-Cr-Si)N system, obtained at P_N = 0.3 Pa and U_b = -200 V: a – general view, x1350; b – enlarged view, x18000

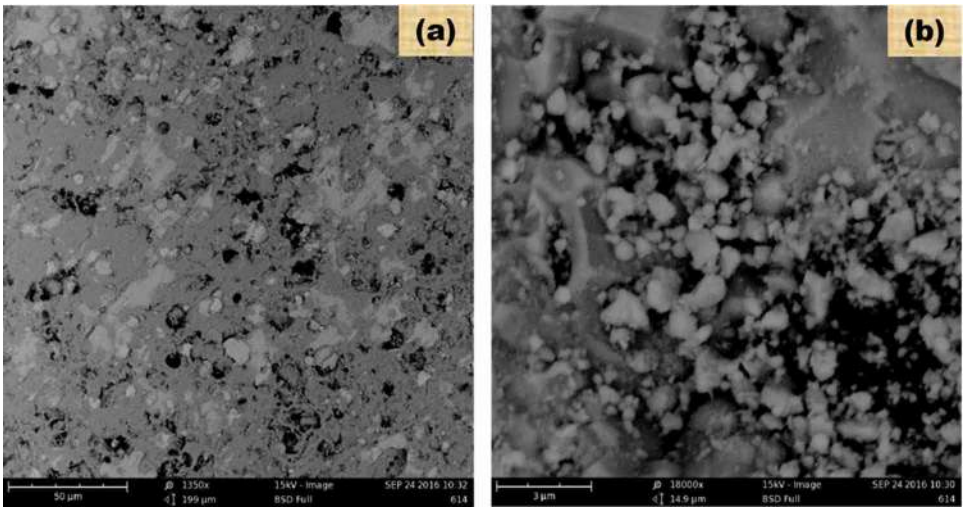

using pulsed RF stimulation of coating deposition. An increase in the bias potential changes the surface topography (Figure 23) and leads to a decrease in the silicon component in the coating.

More generalized data on the coverage area are given by the results of energy dispersive microanalysis, which are shown in Figures 24 and 25.

Energy dispersion analysis data, resulting mean values of elemental microanalysis of system coatings based on (Zr-Ti-Nb)N, (Zr-Ti-Cr-Nb)N and (Zr-Ti-Cr-Nb-Si)N show a good correspondence of the composition of the coating material to the composition of the atomized cathode for heavy elements. It should be noted that the weak diffusion characteristic of a multicomponent coating due to the heteroge-

Figure 24. SEM/EDX-elemental composition of coatings based on (Zr-Ti-Nb-Cr-Si)N, obtained by microanalysis of the surface of the first series of samples, at P_N = 0.3 Pa and U_b = -100 V: a – areas for EDX/EDS-analysis; b – EDX/EDS-spectrum

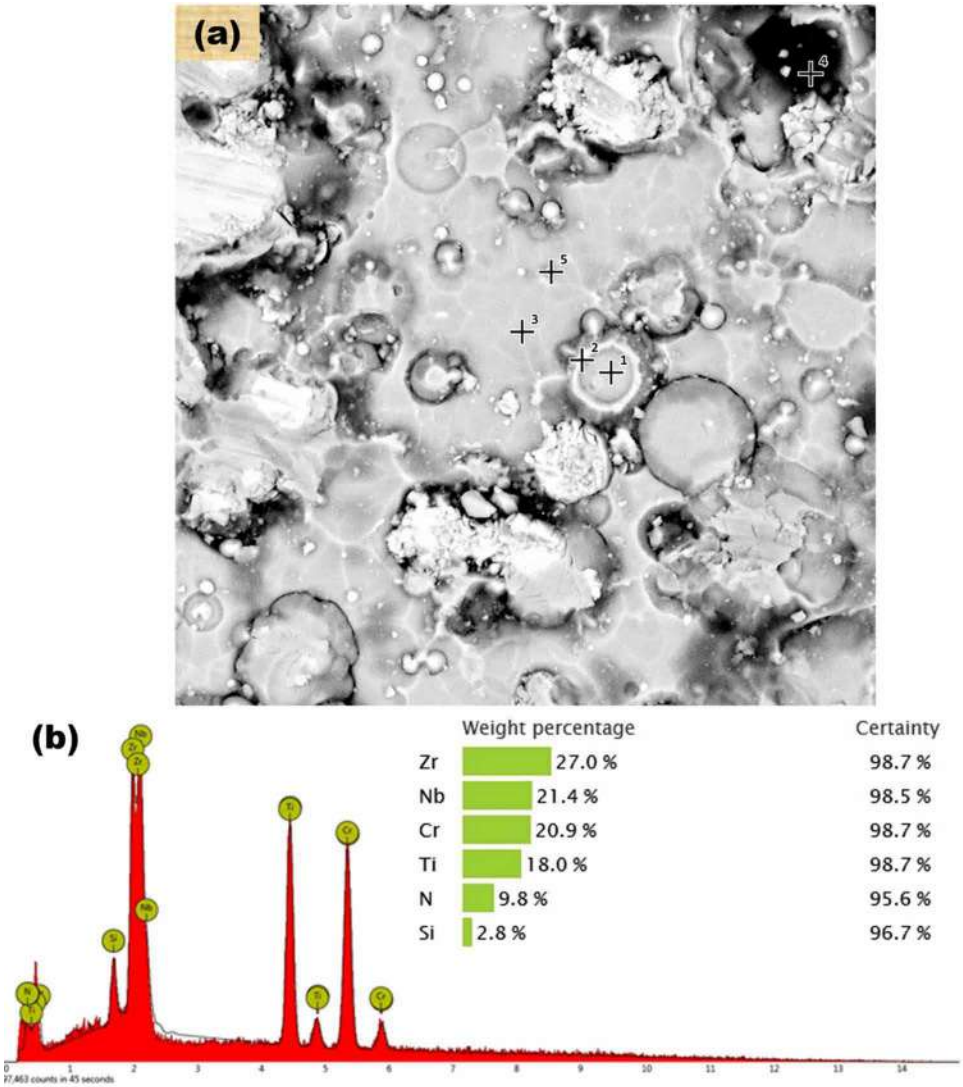

neity of the constituent elements that reduce the effective diffusion distance also leads to more difficult grain growth.

A distinctive feature of multicomponent coatings is the local redistribution of elements in the periodic lattice with the need to maintain one type of solid solution. At the same time, strong fluctuations in the chemical composition cannot but affect the distortions of the crystal lattice and the physical-mechanical properties of the coating. At the same time, it should be noted that with thermal exposure, this process occurs more intensively. As can be seen from the distribution of elements along the profile, in the initial state, the elements in the coating are distributed almost evenly over the surface and depth (Figure 22). From the presented data (Figure 25) it can be seen that the profiles corresponding to the elements Zr,

Figure 25. SEM/EDX-analysis, the profile of the distribution of elements over the depth of (Zr-Ti-Cr-Nb) N coatings

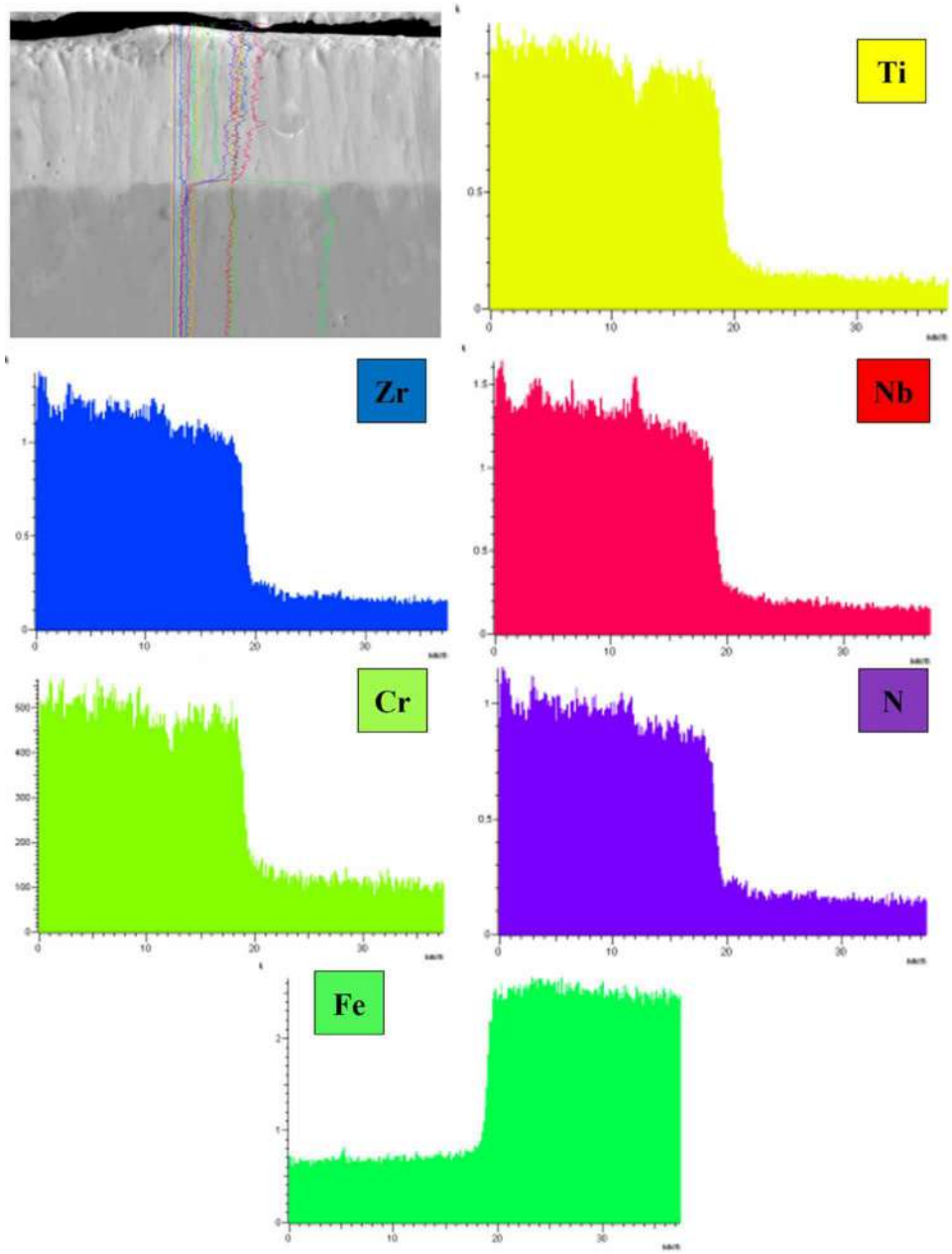

Ti, Cr, Nb and N indicate a homogeneous distribution of elements in depth. As can be seen from the profile of iron, the increase in intensity begins after the end of the coating matrix.

Thus, the use of complementary methods for studying surface morphology and elemental analysis, such as SEM, XPS, EDS, RBS and AFM, made it possible to study the surfaces of coatings and determine the chemical composition of the surface layer, to establish patterns of distribution of elements in depth, as well as to identify uncontrolled impurities.

3.2. Phase Composition of Multicomponent Nitride Coatings Based on (Zr-Ti-Nb)N, (Zr-Ti-Cr-Nb)N and (Zr-Ti-Cr-Nb-Si)N

The results of X-ray diffraction analysis for all samples obtained under various conditions of deposition of coatings based on (Zr-Ti-Nb)N are shown in Figure 26. Analysis of X-ray diffractometer spectra showed that the determining phase composition is a phase with a face-centered cubic lattice (FCC phase). A low peak intensity at 2θ=38° indicates the presence of small inclusions with a body-centered cubic lattice (BCC), typical of the vacuum-arc method for the droplet phase (Figures 12a and 13a). A characteristic feature of the increase in the pressure of the reaction gas (from 0.05 to 0.5 Pa) is the strengthening of the peaks of the family of planes {111}, which is determined by an increase in the perfection of the preferred orientation of the growth of crystallites with the axis perpendicular to the surface plane. It was found that the size of the crystallites increases from 10 nm at the lowest pressure of 0.05 Pa and 63 nm at the maximum operating pressure of 0.5 Pa.

Phase analysis of (Zr-Ti-Cr-Nb)N nitride coatings indicates the presence of the FCC TiN-phase (a=0.243 nm, $a_{tab.}$=0,244 nm) and trigonal modification Cr_2N (space group P31m, a = 0.4800 nm, c = 0.472 nm) (Figure 27). From the X-ray diffraction patterns, it was established that the substrate displacement potential strongly affects the change in the (111) orientation, which is preferable for mixed (111) and (200), and the appearance of (112) and (300) reflections at large angles (trigonal Cr_2N phase). The structural analysis of (Zr-Ti-Cr-Nb)N nitride coatings is consistent with XPS results, while the coatings undergo phase separation. Table 4 shows the grain sizes and lattice parameters of (Zr-Ti-Cr-Nb)N coatings, which were additionally estimated from X-ray diffraction patterns. This table shows that

Figure 26. Areas of XRD-patterns of (Zr-Ti-Nb)N coatings obtained at different partial pressures of nitrogen: 1 – P_N = 0.05 Pa; 2 – P_N = 0.5 Pa

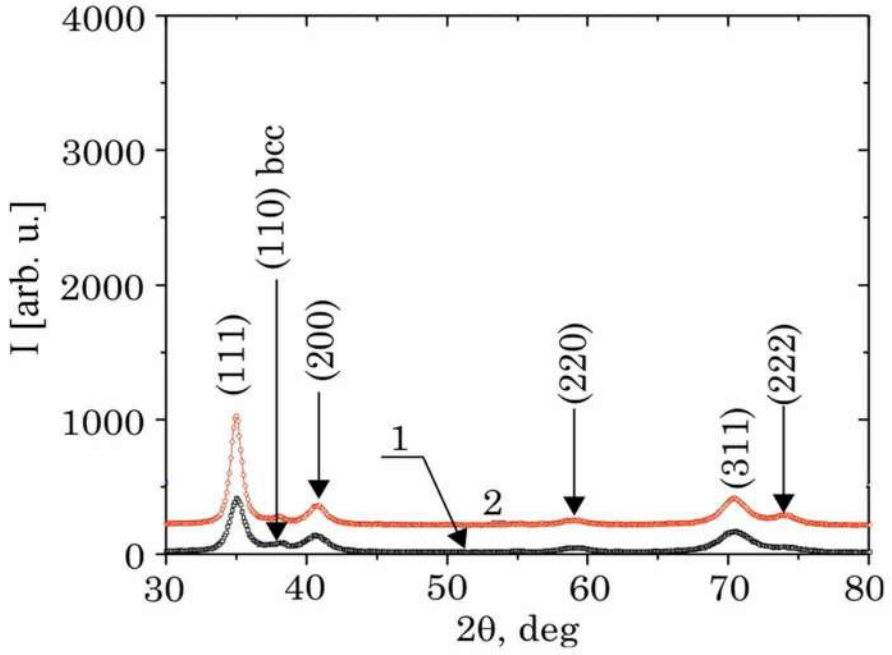

Figure 27. XRD-patterns of (Zr-Ti-Cr-Nb)N coatings deposited at different values P_N and U_b

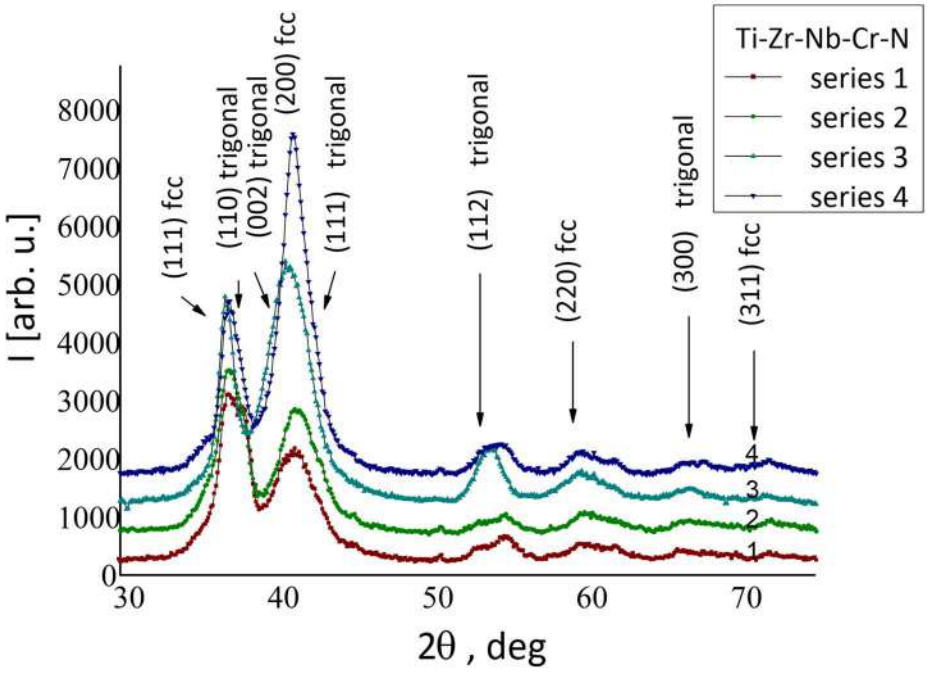

Table 4. Crystallite size and lattice period of (Zr-Ti-Cr-Nb-Si)N and (Zr-Ti-Cr-Nb)N coatings evaluated by X-ray diffraction analysis

Nº Series (Sample)	Nitride Coating	Lattice Period, nm	Crystallite Size, nm
1	(Zr-Ti-Cr-Nb)N	0.4365	5.2
2		0.4359	4.5
3		0.4410	5.1
4		0.4381	6.9
1	(Zr-Ti-Cr-Nb-Si)N	0.4332	11.5
2		0.4337	9.7

the lattice constant increases with U_b. This is reasonable since the energy bombardment results in the incorporation of nitrogen atoms into spaces in the growing film that are smaller than the usual atomic volume (the "atomic shot blasting effect"). In addition, the grain size of (Zr-Ti-Cr-Nb)N nitride coatings is about 5.5 nm for all possible biases, which means that the films have very fine-grained nanocrystalline structures. This statement is confirmed by the results of electron microscopic and diffraction studies. As can be seen from Figure 28, the transition metals of the Zr-Ti-Cr-Nb system form a coating with a finely dispersed structure during the condensation process. The electron diffraction patterns show rings that belong to the FCC-phase.

Figure 28. TEM-image of (Zr-Ti-Cr-Nb)N coatings: a – brightfield image; b – micro-diffraction pattern

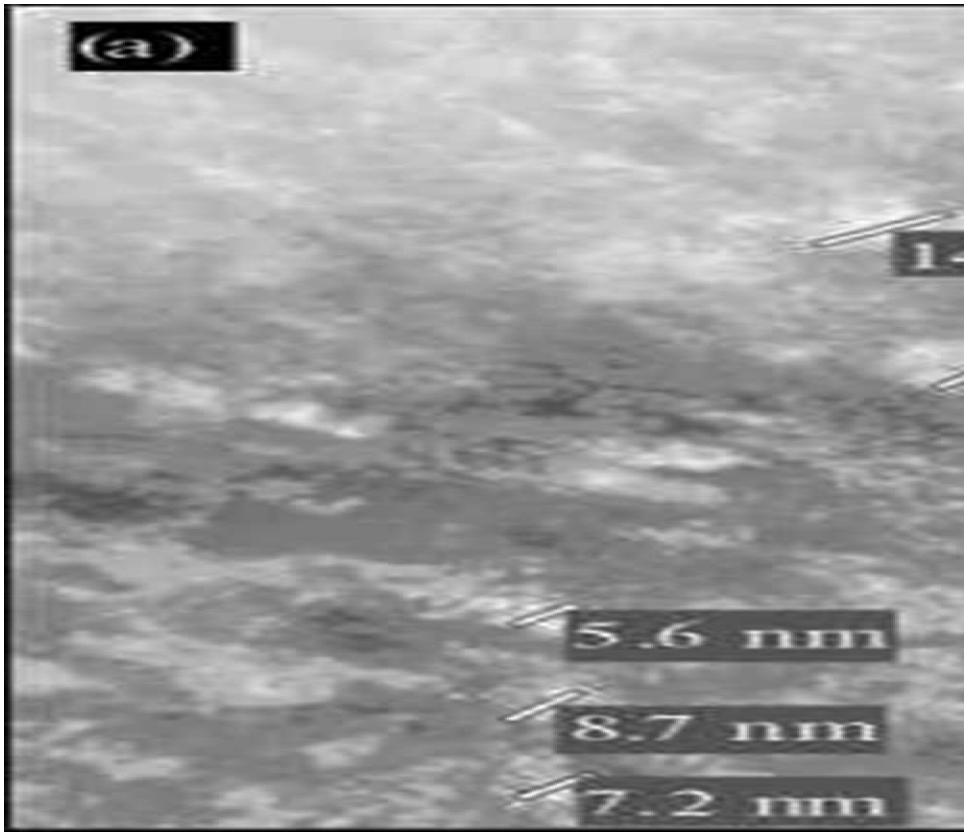

X-ray patterns of (Zr-Ti-Nb-Cr-Si)N coatings deposited at P_N = 0.3 Pa and U_b = 100 and 200 V are shown in Figure 29. As we can see, the substrate displacement has a great influence on the X-ray patterns of (Zr-Ti-Cr-Nb-Si)N coatings. For nitride coatings, only the XRD-lines related to the (111), (200), (220), (222), and (311) peaks from the FCC structure of the B1 phase (NaCl type) are confirmed. It is well known that nanocomposite coatings such as TiSiN are characterized by the formation of amorphous (Si_3N_4)/ crystalline (TiN) composite structures (Wagner, 1995). The non-FCC nitride phase of Si_3N_4 has low solubility in the FCC structure, and thermodynamically conditioned (spinodal) segregation may occur during precipitation. It should be noted that the appropriate Si content to achieve a single layer (Si_3N_4) around each TiN grain is between 5 and 12 at.%, although the exact amount varies depending on the average grain size (Hsieh et al., 2013; Martin et al., 2005). In our case, although the present systems contain several immiscible nitrides, such as TiN and Si_3N_4 (in low concentration), only one fcc phase in the coating was clearly identified (see figure 28). The formation of the nitride of the FCC phase is associated with the high mixing entropy effect and limited diffusion kinetics, in which the atoms cannot reach their stable configuration. (Holleck, 1988).

It was found that with an increase in the displacement potential on the substrate, the positions of the XRD peaks are shifted towards smaller angles (Figure 29). One explanation for this effect is an increase in the lattice parameters of (Zr-Ti-Cr-Nb-Si)N coatings due to the formation of Frenkel pairs and anti-Schottky defects. This shift can also be explained by the fact that a slight compression of the NaCl-type

Figure 29. XRD-patterns of (Ti-Zr-Nb-Cr-Si)N coatings, at P_N = 0.3 Pa and different values of U_b (-100 and -200 V)

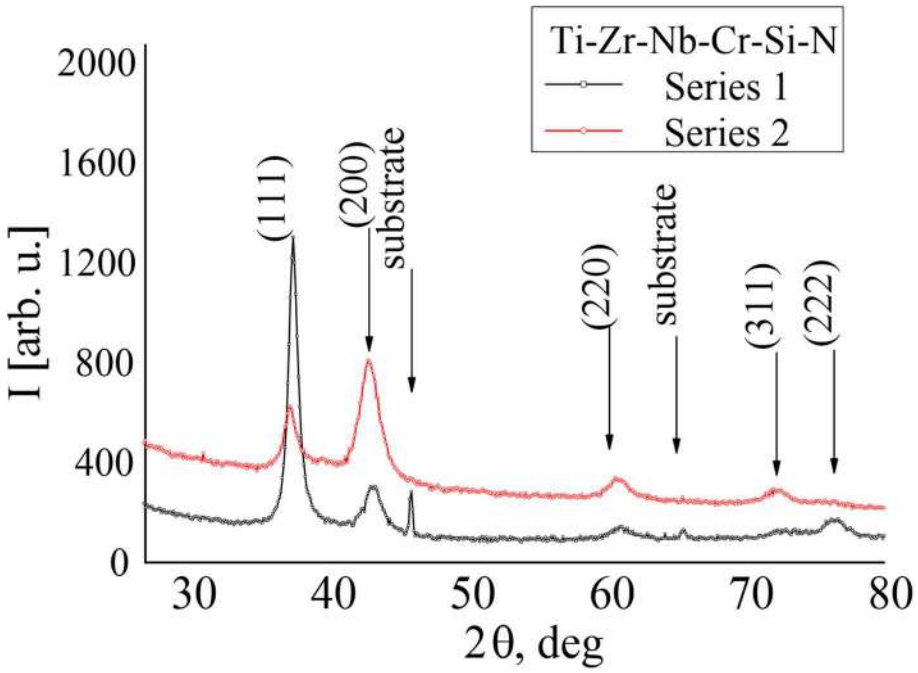

lattice with the presence of Si may be due to a small inclusion of Si in the lattice and the formation of short Me-Si bonds. Moreover, an increase in the Si concentration probably causes a shift of the XRD-peaks, which indicates a possible change in the lattice constant (Kim et al., 2002; Pilloud et al., 2004). Lattice parameters for deposited (Zr-Ti-Cr-Nb-Si)N coatings gradually increases from 0.4332 nm at a negative displacement of the substrate -100 V, 0.4337 nm at a displacement of -200 V (Table 5). The average grain sizes of the films were calculated from X-ray images using the Scherrer formula, and it was found that they strongly depend on an increase in the displacement potential on the substrate. The size of the crystallites in the coating of series 1 (U_b = -100 V) averaged 11.5 nm, for series 2-9.7 nm (U_b = -200 V). It is well known that high-energy ion bombardment prevents the migration of grain boundaries due to an increase in the number of preferred nucleation centers, which reduces the grain size. As can be seen from the results in Table 5, when the Si content increased from zero to 3.5, the size of the crystallites increased from 4.5 to 11.5 nm, while the lattice parameter decreased. Similar results were obtained in various papers devoted to the study of Si-containing nitride systems (Kim et al., 2002; Pilloud et al., 2004). From the XRD analysis, as shown in Figures 26, 27 and 29, it was found that on all (Zr-Ti-Nb)N and (Zr-Ti-Cr-Nb-Si)N coatings, only a single solid nitride phase was formed, and not separate nitrides coexisting with each other. Although some factors, such as the nonequilibrium process of physical deposition, from the vapor phase, high entropy of mixing (for multicomponent coatings) and a small difference in atomic radii, may contribute to the formation of crystal structures of this nature. Similar results were also obtained as precipitated nitrides, such as $Zr_xTi_{1-x}N$, $Cr_xTi_{1-x}N$, $Nb_xTi_{1-x}N$, (AlCrTaTiZr)N, (CrTaTiVZr)N, (TiHfVNbZr)N (Bagdasaryan et al., 2014; Cecchini et al., 2011).

Figure 30. Calculated mixing energy (E_{mix}) of $Ti_{1-x}Nb_xN$, $Ti_{1-x}Zr_xN$ u $Zr_{1-x}Nb_xN$ alloys depending on composition x

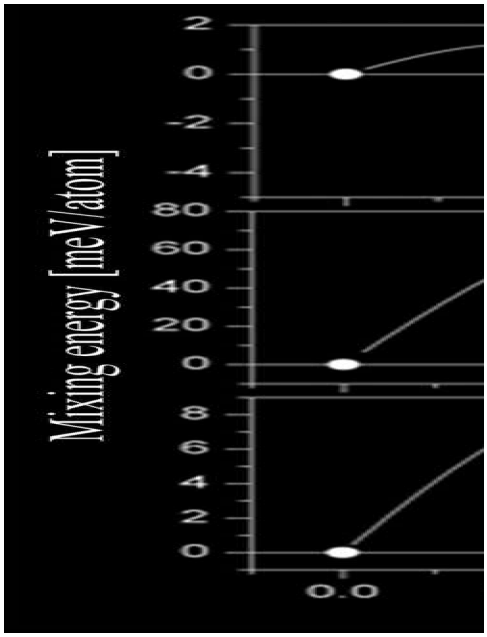

Figure 30 shows the Gibbs free energy of mixing of the studied alloys calculated at T = 0 K (i.e., the energy of formation) depending on the composition of *x*. The positive energy of formation means that $Ti_{1-x}Zr_xN$ alloys are unstable and will decompose into TiN and ZrN with chemical driving force (E_{mix}). However, all alloys can be stabilized in a certain range of composition, depending on temperature, since the configuration entropy is always positive and contributes to a decrease in the Gibbs free energy. Since the E_{mix} values for $Ti_{1-x}Nb_xN$ and $Zr_{1-x}Nb_xN$ are very small, and some of them are negative, these alloys can be stabilized as solid solutions at moderate temperatures. These data confirm the possibility of formation of solid FCC solutions based on TiN, ZrN and NbN in thin coatings. Since we observed only solid solutions based on these nitrides in our coatings, it can be assumed that the presence of NbN in the films excludes the separation of TiN and ZrN from $Ti_{1-x}Zr_xN$ alloys. Nevertheless, for the coatings of the (Zr-Ti-Cr-Nb)N system, experimental results indicate the existence of a two-phase structure: the FCC phase TiN (a = 0.243 nm, a_{tab} = 0.244 nm) and the trigonal modification Cr_2N (spatial group P31m, a = 0.4800 nm, c = 0.4472 nm). The formation of a two-phase structure is obviously associated with the presence of high concentrations of Cr and Nb elements, which have a low enthalpy of nitride formation (Table 5).

Table 5. The enthalpy of formation of nitrides of the constituent elements of the studied nitride coatings

-	TiN	ZrN	NbN	CrN	Cr_2N	Si_3N_4
ΔH, kJ/mol	-337.7	-365.3	-234.7	-117.2	-129.0	-106.0

Figure 31. Triangular map of the distribution elements, obtained using EDX (TEM): a – solid solution Nb-Zr-N; b – solid solution Zr-Ti-N; c – solid solution Cr-Zr-N; d – solid solution Nb-Ti-N

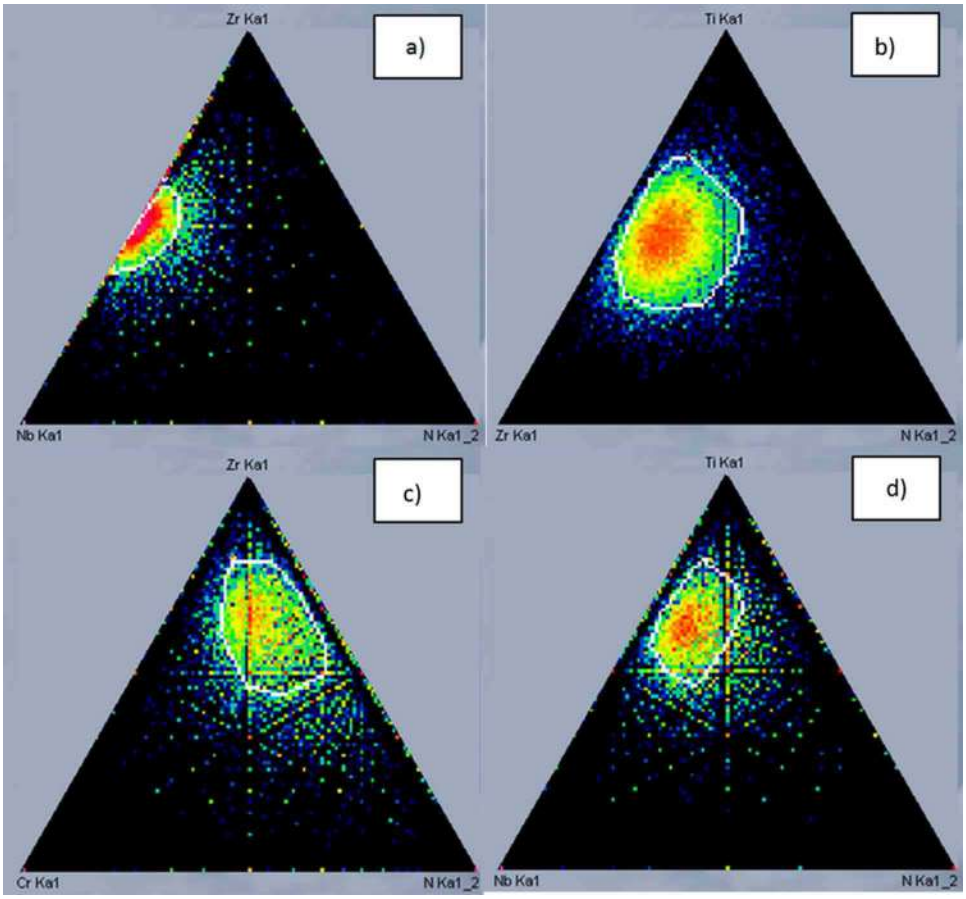

Cecchini R. et al. (Cecchini et al., 2011) showed that with increasing nitrogen pressure, the crystalline phase of the coatings passes from Cr_2N (main phase) + CrN to CrN (main phase) + Cr_2N. These results are confirmed by the presentation of the Gibbs-Rosenbaum triangle (Figure 31). The vertices of an equilateral triangle correspond to the 100% content of each component of the system. The elemental composition determination method is based on the fact that the sum of perpendiculars from any point inside an equilateral triangle on each side is equal to the height of the triangle. Rosenbaum proposed the use of three segments of straight lines parallel to the sides of the triangle and extending from that point to intersect with each side of the triangle. The sum of the three-line segments for each point inside an equilateral triangle is equal to the length of its sides. As can be seen from Figure 31, the percentage of Ti-N, Zr-N systems is higher than that of Cr-N and Nb-N, thus resulting in the formation of a solid solution with a high TiN and ZrN content.

It is well known that the application of a bias potential on a substrate can significantly change the structure of coatings and their properties. When a substrate bias potential is applied, reactive gas and metal ions bombard the substrate. With an increase in the bias potential on the substrate, the energetic ion bombardment becomes more intense. Due to the enhanced bombardment effect, the densification of the

coating is increased by reducing void areas in the microstructure.It should be noted that in all coatings, the predominant (111) orientation was observed at $U_b = –100$ V. When the substrate bias potential was increased to $U_b = -200$ V, the nitride films showed strong (200) and relatively weak (111) orientations. This phenomenon may be due to various kinetic constraints (anisotropy in surface diffusion, adatom mobility, and collisional cascade effects) that are thought to affect the preferential orientation.

Conclusions for Section 3

1. Nanostructured coatings of the (Zr-Ti-Nb)N, (Zr-Ti-Cr-Nb)N and (Zr-Ti-Cr-Nb)N and (Zr-Ti-Cr-Nb-Si)N systems were obtained by vacuum-arc deposition of a solid-cast cathode in a nitrogen reaction gas medium, the main matrix has a pronounced columnar structure and consists of droplet fractions up to 10 μm.
2. The use of complementary methods of elemental analysis (SEM, TEM, XPS, EDX/EDS, RBS and AFM) made it possible to study the surfaces of coatings and determine the chemical composition of the surface layer, to establish patterns of homogeneous distribution of titanium, chromium, zirconium, niobium, silicon and nitrogen atoms in depth, as well as to determine uncontrolled impurities as C and O.
3. When the pressure in the chamber increases from 0.05 to 0.3-0.7 Pa in some cases and the potential on the substrate from -100 to -200 V leads to a significant decrease in the concentrations of droplet fractions on the surface.
4. It is established that in the coating of the (Zr-Ti-Nb)N system, the main phase is the solid solution phase with a FCC lattice with a growth texture (111) and a small volume fraction of the phase with a BCC lattice with a growth texture (110).
5. When Cr and Si elements are added to the cathode in series, a TiN-based FCC phase and a phase with a Cr_2N trigonal lattice are formed in the coatings, for the first case, and for the second, a solid solution of FCC is also formed by a lattice and a growth texture (111).

4. MECHANICAL AND TRIBOLOGICAL CHARACTERISTICS OF MULTICOMPONENT NITRIDE COATINGS BASED ON Zr, Ti, Nb, Cr, AND Si

4.1. Mechanical Properties of Multicomponent Nitride (Zr-Ti-Nb)N, (Zr-Ti-Nb-Cr)N and (Zr-Ti-Nb-Cr-Si)N Coatings

The research and development of nanostructured materials is a promising area of materials science, promising the creation of fundamentally new protective coatings with excellent physical and mechanical properties. The uniqueness of such materials lies in the presence of structural elements with a size of less than 100 nm, which allows them to acquire physical and mechanical properties different from bulk bodies. Special attention should be paid to nanocrystalline multicomponent coatings based on nitrides, borides, oxides, etc. A feature of such coatings is the formation of a grain structure due to phase segregation, in which nanocrystals (solid phase) are separated by an interlayer of an amorphous phase. Studies show that coatings with a similar structure have excellent performance characteristics (superhardness > 40 GPa, elastic recovery > 70%, etc.) (Veprek, 2013).

A review of the literature showed that the main factors that increase the hardness of coatings are: the adhesion forces between atoms, compressive stresses, plastic deformation with the dominant role of dislocations, and nanostructure. The maximum hardness can be obtained with grain sizes d_c ~ 10 nm. The region near H_{max} corresponds to a continuous transition from microscopic processes of nucleation and motion of dislocations at $d > d_c$, described by the well-known Hall-Petch law ($H \sim d^{-1/2}$) for ordinary polycrystalline materials, to intercrystalline processes of local slip along grain and phase boundaries at $d \sim d_c$. The increase in the hardness of the coating is due to the interaction of all factors, which greatly complicates the determination of the real origin of hardness. The literature review showed the existence of two ways to increase the strength of the coating, namely: energy ion bombardment and the creation of nanocomposite coatings. Thus, in the case of an increase in the energy of the sprayed ions, the grain boundaries are compacted, the grain size is reduced, and high compressive stresses are formed. The creation of a nanocomposite structure in the coating leads to inhibition of the propagation of deformations such as cracks and dislocations, which has a beneficial effect on strength characteristics. In the case of nitride coatings based on multicomponent alloys, special attention should be paid to solid-solution hardening. A wide choice of coating components can lead to serious distortions of the crystal lattice due to the discrepancy of atomic radii. According to the dislocation theory, the strength increase occurs due to the inhibition of dislocations in the fields of elastic stresses caused by distortions of the crystal lattice. As a result, dislocations appear to be blocked by the atoms of the dissolved substance. An analysis of the periodic literature (Liang et al., 2011; Tsai et al., 2010) devoted to the study of the mechanical characteristics of nitride coatings based on multicomponent alloys has shown that the main factors affecting the hardness value are: the number of nitride-forming constituent elements, as well as the parameters of the deposition condition.

The study of the mechanical characteristics of nitride coatings deposited at various deposition parameters was carried out using microhardness testers “DM8-B” and “Durascan-20” manufactured by “CSM Systems AG” (Switzerland). The results of measurements of mechanical characteristics, in particular, the hardness of all obtained coatings, are shown in Table 6.

Table 6. Average hardness values of nitride coatings

Series (Sample) No.	Hardness, GPa
(Zr-Ti-Nb)N $HV_{0.025}$ GPa	
1	37.2
2	44.5
(Zr-Ti-Cr-Nb)N $HV_{0.1}$ GPa	
1	30.9
2	34.7
3	38.8
4	43.9
(Zr-Ti-Cr-Nb-Si)N $HV_{0.1}$ GPa	
1	29.0
2	24.0

As can be seen from Table 6, the maximum hardness value (44.5 GPa) for the (Zr-Ti-Nb)N nitride coating is achieved at a reaction gas pressure of $P_N = 0.5$ Pa. As we can see, the hardness of (Zr-Ti-Cr-Nb)N coatings deposited at $P_N = 0.3$ Pa and $U_b = -100$ V is 30.9 GPa and changes up to 43.9 GPa with increasing bias voltage on the substrate up to -200 V. It should be noted that coatings applied at a lower nitrogen content have low hardness. When P_N increases to 0.7 Pa, the increase in hardness is explained by the formation of more strong Me/N bonds present in the films. Moreover, the high hardness may be due to the high content of the Cr_2N phase since the hardness of the Cr_2N coating is higher than that of the CrN coating. For (Zr-Ti-Cr-Nb-Si)N nitride coatings deposited at $P_N = 0.3$ Pa and $U_b = -100$ V, the hardness is 29 GPa and the elastic modulus is 291 GPa. As the bias voltage on the substrate increased to –200 V, the hardness and elastic modulus decreased to 24 and 254 GPa, respectively. One explanation for the decrease in hardness is excessive ion bombardment, resulting in less textured coatings, a transition from a predominantly (111) high-intensity orientation to a high FCC orientation, including additional (111) and (200) orientations. The nanohardness and elastic modulus of (Zr-Ti-Cr-Nb-Si)N coatings were measured using a "Hysitron TI 950 TriboIndenter" nanoindenter with a Berkovich diamond indenter, the maximum load was 10,000 μN. The hardness value and modulus of elasticity were evaluated from indenter load-unload curves using the Oliver and Farr methods. From nanoindentation tests of load-unload curves of (Zr-Ti-Cr-Nb-Si)N coatings, the nanohardness and modulus of elasticity of the films deposited on the substrate at various bias voltages were determined and shown in Figure 32. Table 7 shows the results of tests for adhesion of (Zr-Ti-Nb)N, (Zr-Ti-Cr-Nb-Si)N and (Zr-Ti-Cr-Nb)N coatings

Figure 32. Dependences of hardness and elastic modulus on the contact depth for (Zr-Ti-Vr-Nb-Si)N coatings, at $P_N = 0.3$ Pa and different values: $U_b = -100$ V, a – hardness [GPa]; b – Young' modulus (Elastic modules) [GPa]; $U_b = -200$ V, c – hardness [GPa]; d – Young' modulus (Elastic modules) [GPa]

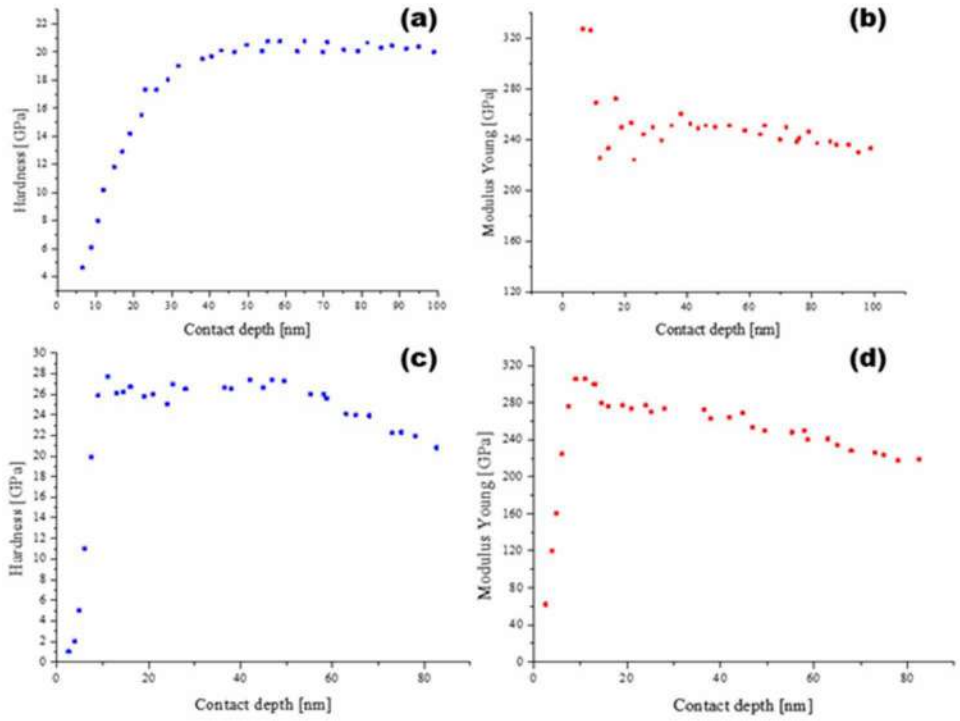

Table 7. Comparative results of adhesion tests for (Zr-Ti-Nb)N, (Zr-Ti-Cr-Nb)N and (Zr-Ti-Cr-Nb-Si) N coatings

Critical Loads [N]	Series (Sample) No.			
	No.1	No.2	No.3	No.4
(Zr-Ti-Nb)N				
L_{C1}	02.91	09.89	-	-
L_{C2}	29.04	20.62	-	-
L_{C3}	43.18	36.43	-	-
L_{C4} (L_{C5})	59.26	66.77	-	-
(Zr-Ti-Cr-Nb)N				
L_{C1}	10.94	11.80	10.35	15.21
L_{C2}	18.69	20.93	18.42	24.29
L_{C3}	26.95	30.35	23.12	33.45
L_{C4}	39.15	45.94	45.12	40.97
L_{C5}	49.09	56.17	61.08	62.06
(Zr-Ti-Cr-Nb-Si)N				
L_{C1}	09.54	11.28	-	-
L_{C2}	12.48	14.04	-	-
L_{C3}	18.36	24.00	-	-
L_{C4}	29.86	34.09	-	-
L_{C5}	45.33	45.57	-	-

Figure 33. Micrographs of the contact area of a diamond indenter coated with (Zr-Ti-Nb)N (P_N=0.5 Pa), at different stages of scratch testing: a – L_{C1}; b – L_{C2}; c – L_{C3}; d – L_{C4} (L_{C5})

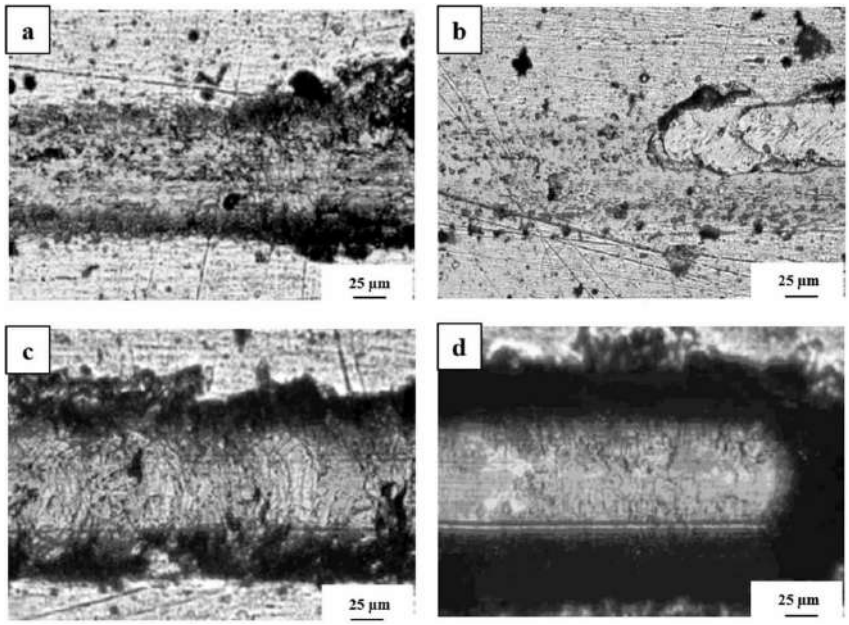

Figure 34. Dependence of the friction coefficient and the acoustic emission signal on the applied load during scratch testing of the (Zr-Ti-Nb)N coating obtained at P_N=0.5 Pa

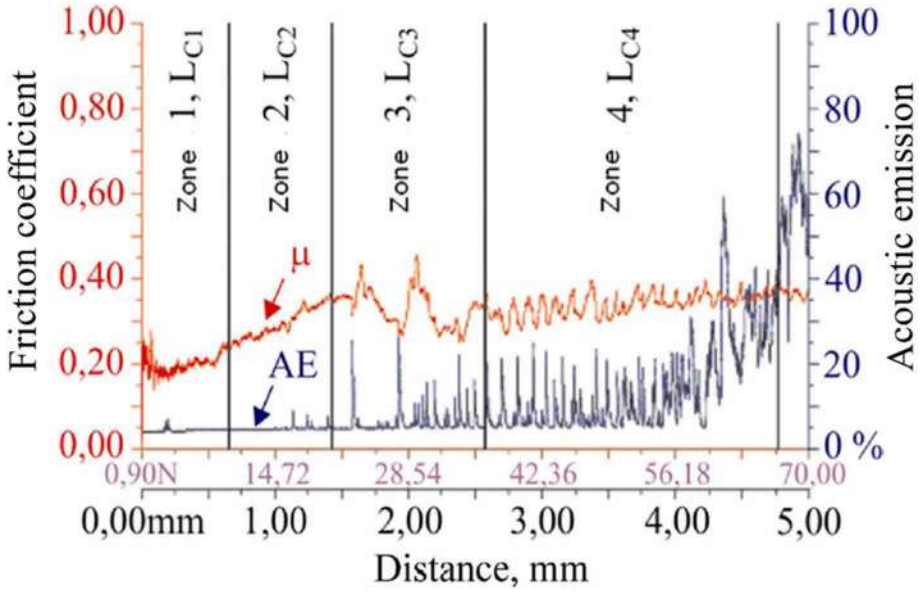

obtained at various deposition process parameters. The results of the study of adhesive-cohesive strength and scratch resistance of coatings are shown in Figures 33 and 34. In accordance with these criteria, the process of coating destruction during scratching with an indenter can be conditionally divided into four stages. In the load range from F=0.9 to 9.89 N, monotonous penetration of the indenter into the coating occurs, while the friction coefficient slightly increases, and the acoustic emission signal remains unchanged. At a load F=15.81 N, the indenter is completely immersed in the coating, and the diamond indenter slides over the coating with a friction coefficient of 0.35. With an increase in load (F=20.6-36.4 N), the material is squeezed out in front of the indenter in the form of tubercles and the penetration depth of the indenter increases.

Comparative analysis shows that (Zr-Ti-Cr-Nb)N coatings wear off but do not peel off during scratches, i.e. are destroyed due to the cohesive mechanism of plastic deformation and the formation of fatigue cracks in the coating material. Figure 35 shows the curve of change in the coefficient of friction (μ) when moving the diamond indenter on the surface of the coating of the (Zr-Ti-Cr-Nb)N system (sample 4), the curve of change in acoustic emission (AE) and the image of the remaining fragments of the coating at the bottom of the scratch after impact of a diamond indenter.

As we can see, monotonous penetration of the indenter into the coating occurs, and the first cracks appear (load up to 15.21 N); the coefficient of friction (μ) increases, but the acoustic emission signal remains unchanged. Subsequently, with an increase in the load, chevron and diagonal cracks appear, which leads to an increase in the friction coefficient to a value of 0.3. At a load of up to 14 N, the amplitude of the acoustic emission signal sharply increases, and its value remains at the same level until the end of the test. After that, with an increase in the load to 62 N, local abrasion of the coating occurs down to the substrate material. The dependence of the change in the friction coefficient and acoustic emission on the applied load on the (Zr-Ti-Cr-Nb-Si)N coating samples for series 1 and 2 is shown in

Figure 35. Dependence of the coefficient of friction and acoustic emission signal on the applied load during scratch testing of the (Zr-Ti-Cr-Nb)N coating series sample 4

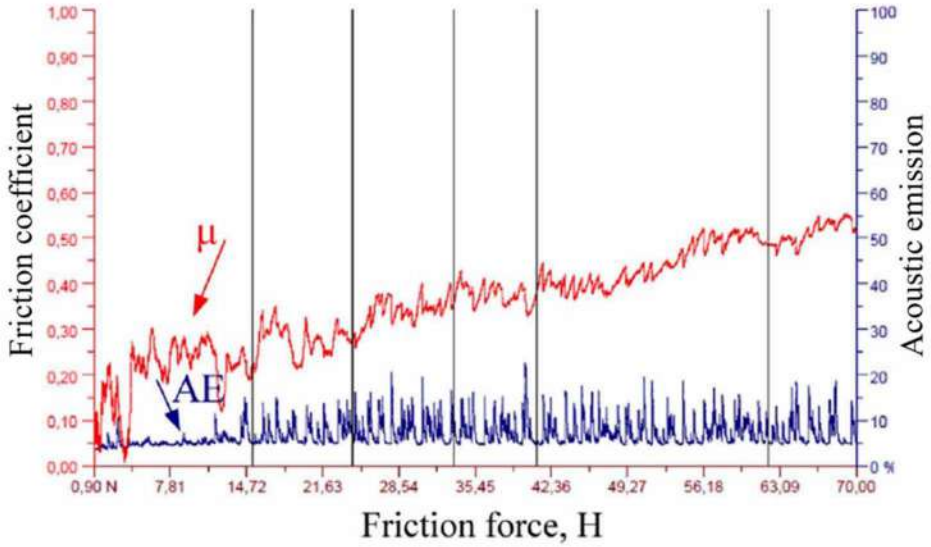

Figure 36. As we can see, at a load of 9 N (L_{C1} for series 1) and 11 N (L_{C1} for series 2) correspond to the appearance of the first cracks and fragments (figure 37 and 38). This is confirmed by the beginning of the increase in the amplitude of acoustic emission (Figure 36). The initial abrasion of coatings occurs at loads L_{C3}=18 N (series 1) and L_{C3}=24 N (series 2) (Figures 37 and 38), which leads to an increase in the friction coefficient to a value of 0.49 for all coatings. Local abrasion of coatings down to the substrate material occurs when the load reaches 45 and 46 N. In this case, the friction coefficient increases to a maximum value of 0.63.

Figure 39 shows the changes in the chemical composition of (Zr-Ti-Cr-Nb-Si)N coatings' during the scratch-test. A sharp increase in the iron concentration (at a distance of 3 mm) corresponds to the appearance of the first cracks and the beginning of the initial abrasion of the coatings.

In addition, it should be noted that the iron (Fe) content in the (Zr-Ti-Cr-Nb-Si)N coatings increases more intensively at a bias voltage U_b = -100 V. This statement is confirmed by a lower value of the critical load ((L_{C3}): 18.36 and 24 N, respectively), which corresponds to the beginning of the initial abrasion of the coatings (Table 7). The chemical composition of the (Zr-Ti-Cr-Nb-Si)N coatings at local abrasion is practically the same, but the nitrogen concentration in series 2 is higher than in series 1, which is consistent with the EDX result. For multicomponent (Zr-Ti-Cr-Nb-Si)N coatings for series 1, the adhesion strength at different intervals of the experiment differs significantly from the strength of coatings (samples) of series 2. As the load increases, a noticeable crack propagation on the coating surface does not occur. Based on the nature of the failure, the main contribution appears to be related to shear stresses. Cohesive failure occurs during cracking in a plane perpendicular to the direction of coating growth. The first signs of coating abrasion were recorded at a load of 18 N. The results of the adhesive strength tests show that the coatings were worn during scratches but did not peel off, i.e., the failure occurred due to the cohesive mechanism associated with plastic deformation and the formation of fatigue cracks in the coating material. A comparative analysis shows (Table 7) that the difference in

Figure 36. Dependence of the friction coefficient and acoustic emission signal on the applied load during scratch testing of the (Zr-Ti-Cr-Nb-Si)N coating, a – series (sample) 1: U_b = -100 V; b – series (sample) 2: U_b = -200 V

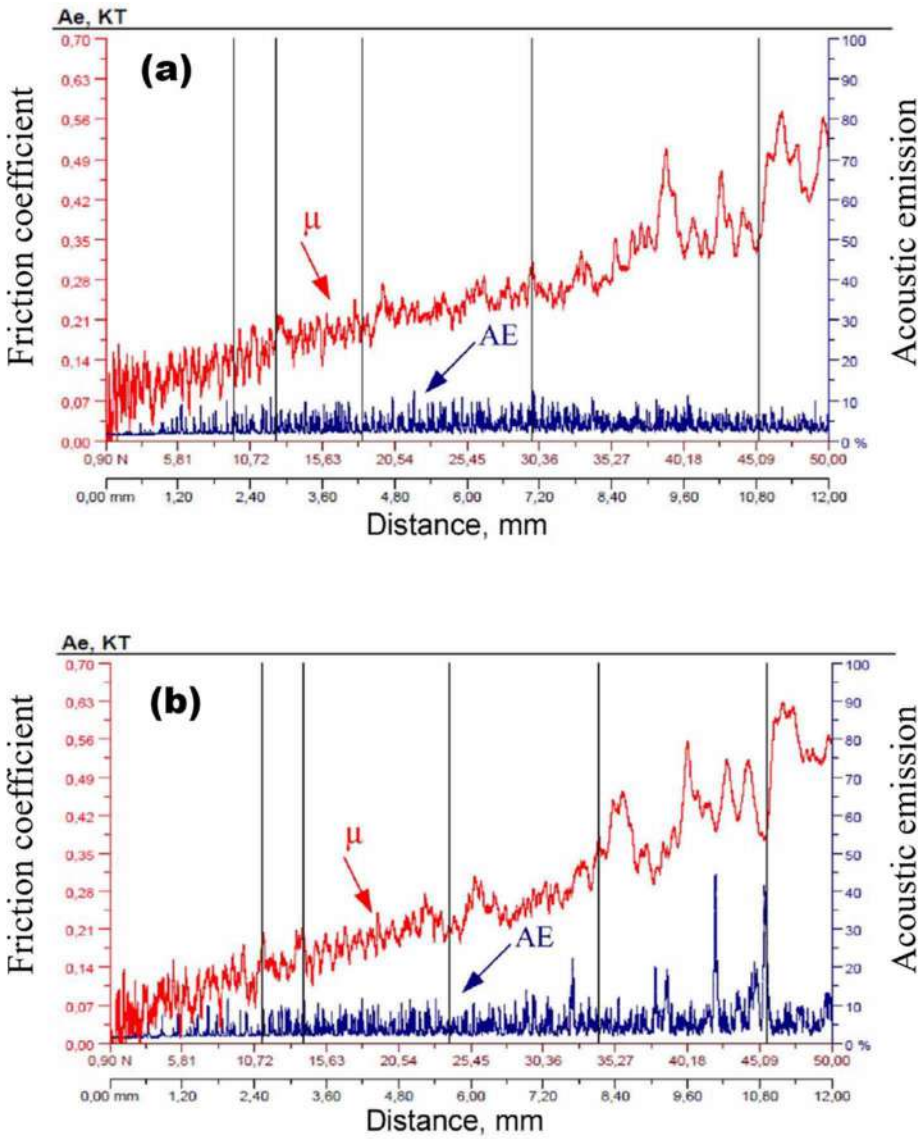

the adhesion strength (adhesion) of the coatings is apparently due to differences in their structure and mechanical properties. As shown in Table 7, as the substrate displacement increases, the adhesion strength between the coating and the substrate increases. Increased adhesion may be associated with increased resistance to cracking and plastic deformation. Loads (L_{C5}) for (Zr-Ti-Cr-Nb)N and (Zr-Ti-Cr-Nb-Si)N coatings increases, with increasing substrate displacement (from -100 to -200 V), their maximum value was 62.06 and 45.57 N, respectively. In addition, it should be noted that coatings obtained with a high displacement potential have a higher hardness and are more stable (Pogrebnjak, Yakushchenko, Bondar et al, 2016; Shypylenko et al., 2016). Nitride coatings (Zr-Ti-Cr-Nb)N and (Zr-Ti-Cr-Nb-Si)N with

Figure 37. Microphotographs of the contact area of a diamond indenter coated with (Zr-Ti-Cr-Nb-Si) N series (sample) 1, at different loads on the indenter: a – 9.54 N (L_{C1}); b – 12.48 N (L_{C2}); c – 18.36 N (L_{C3}); d – 29.86 N (L_{C4}); e – 45.33 N (L_{C5})

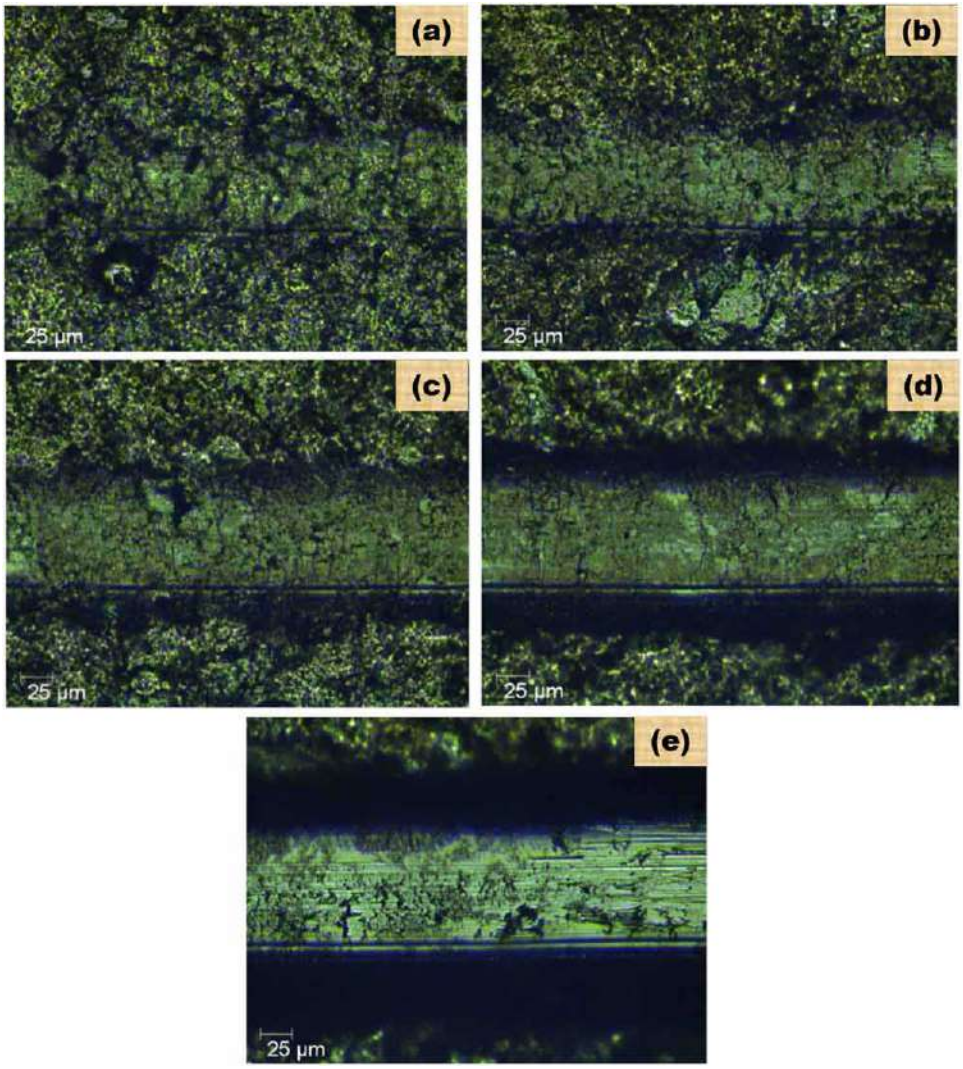

good adhesive strength demonstrate high hardness values of 43.9 and 29 GPa, respectively. Comparing the results from Tables 6 and 7, it can be seen that coatings with high hardness have good adhesive strength. It was previously reported that the application of the displacement potential on the substrate during deposition can cause collision mixing and, consequently, lead to improved adhesion (Hones et al., 1998; Yamamoto et al., 2003).

Figure 38. Microphotographs of the contact area of a diamond indenter coated with (Zr-Ti-Cr-Nb-Si)N series (sample) 2, at different loads on the indenter: a – 11.28 N (L_{C1}); b – 14.04 N (L_{C2}); c – 24 N (L_{C3}); d – 34.09 N (L_{C4}); e – 45.57 N (L_{C5})

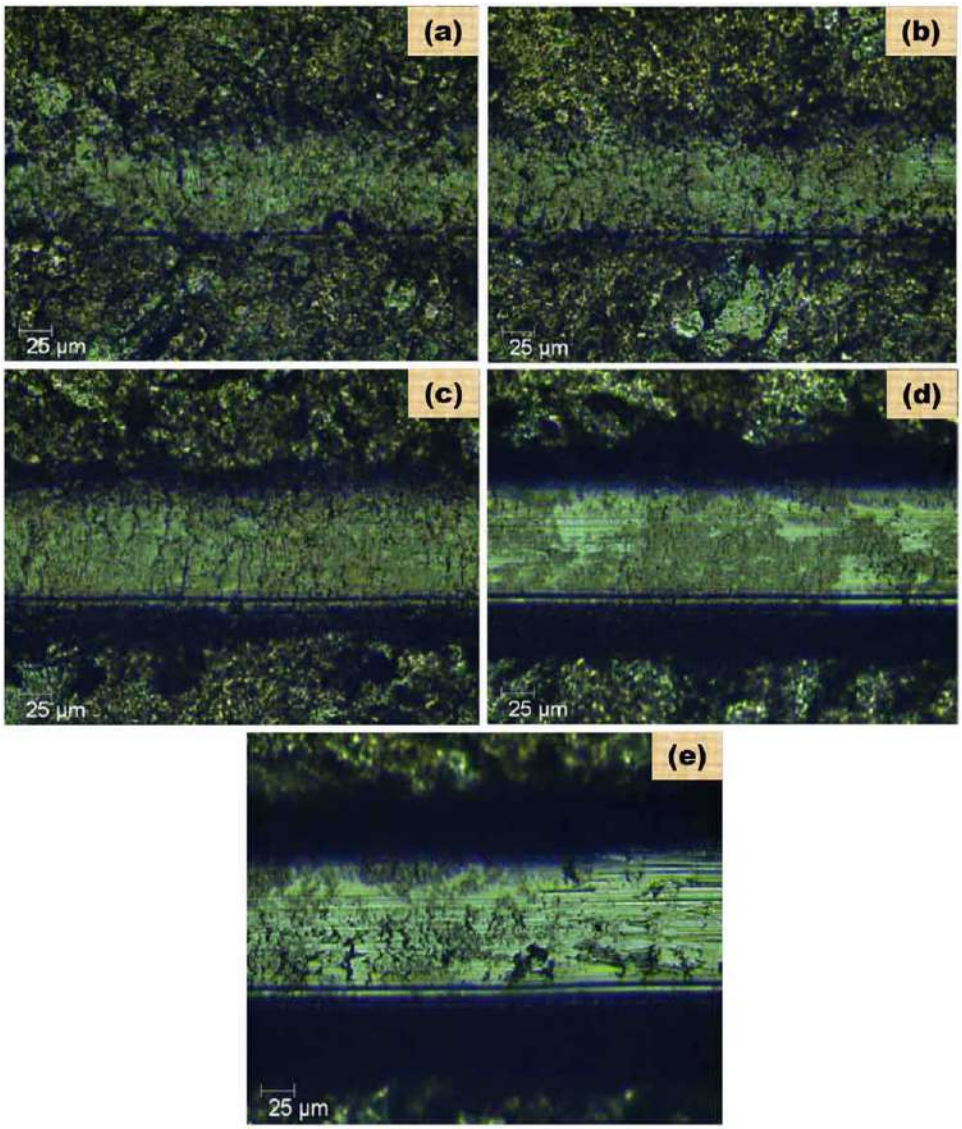

4.2. Tribological Characteristics of Coatings Based on Zr, Ti, Nb, Cr and Si Elements

One of the tasks of materials science and industry is to solve the problems of wear of machine parts, tools, mechanisms, etc. Thus, the concept of creating tribological coatings seeks to optimize two main characteristics of nanostructured coatings, namely, an increase in hardness *H* with a simultaneous decrease in the elastic modulus *E*, in other words, it is necessary to increase the ratio *H/E*. This ratio plays a key role for coating surfaces, since the behaviour of the latter under load must be consistent with the char-

Figure 39. EDX-chemical composition of scratches on (Zr-Ti-Cr-Nb-Si)N coatings after testing, a – series (sample) 1: U_b = -100 V; b – series (sample) 2: U_b = -200 V

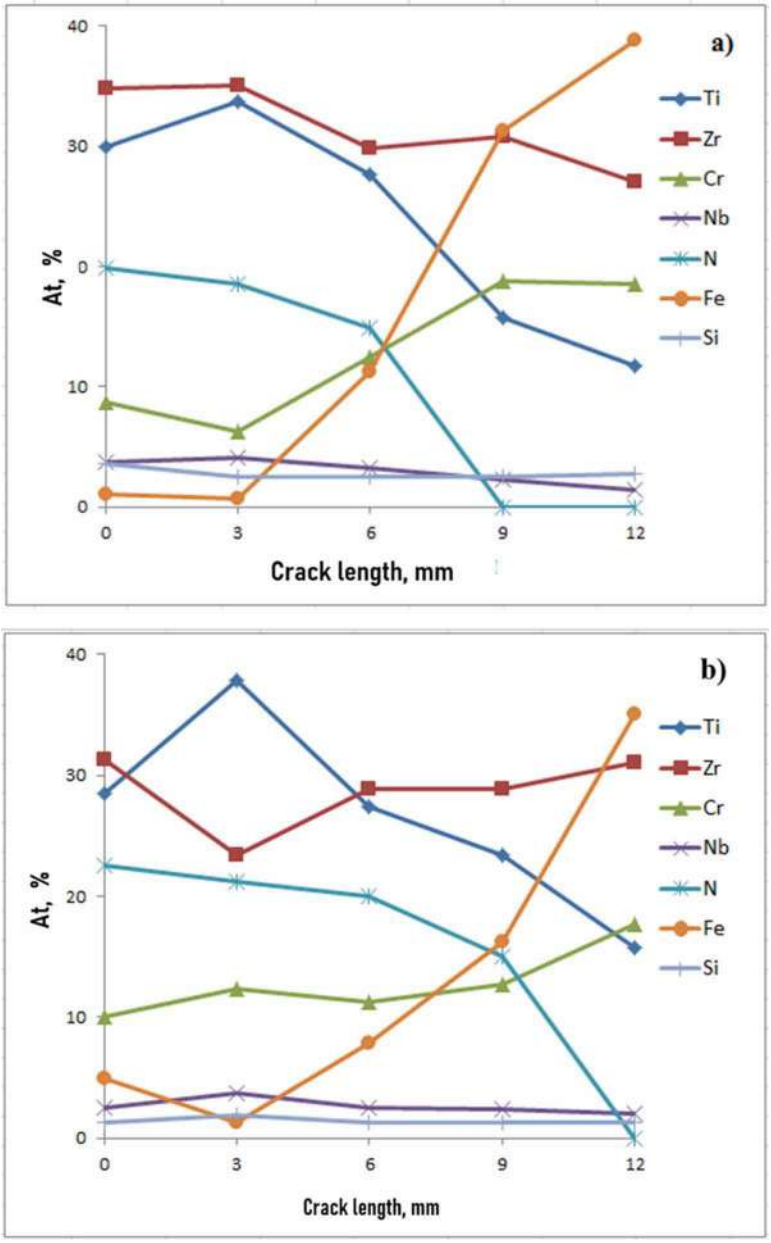

acteristics of the substrate. It follows from this that the elastic modulus of the substrate and the coating should be as close as possible in value, this allows to reduce the peak stress values at the contact points, as well as to reduce the stress values at the interface between the hard coating and the substrate (Godet et al., 1991; Ramalingam & Zheng, 1995).

The development of general ideas and ideas for creating wear-resistant coatings is primarily related to the works of Holmberg (Holmberg & Matthews, 1994), where the classification of interactions in the process of friction of surfaces is given, namely:

a) macromechanical;
b) micromechanical;
c) substance transfer processes;
d) tribomechanical;
e) nanomechanical.

The first class (macromechanics) includes macroscopic processes that occur under the action of macroscopic loads that cause stresses and deformations in the near-surface layer (Gavaleiro & De Hosson, 2006). The mechanisms of processes at the micro level are primarily associated with the origin and development of cracks, the formation of fragments, etc. The transfer of matter and tribomechanical reactions of the surface are related to the characteristics of materials and their phase composition. One of the main methods of applying protective coatings to the inside of parts is vacuum arc deposition. The specific features of this method make it possible to obtain coatings that are superior to ceramic in many respects (adhesion, hardness, fracture toughness, etc.) (Gavaleiro & De Hosson, 2006). Coatings obtained by vacuum arc deposition are often a compound of the type of embedding phases, however, the use of alloying elements with low solubility can lead to the formation of substitution phases, which is a key condition for the creation of a nanocrystalline phase, as well as glassy films.

First of all, the selection of constituent elements for the creation of wear-resistant coatings comes from the ability of the elements to form nitrides. In our case, Zr, Ti, Nb, Cr and Si elements have a high heat of nitride formation (see Table 1). At the same time, the melting point of the mentioned elements exceeds 1700°C, which allows them to be attributed to refractory materials. It is also worth noting that the atoms of the selected elements have similar geometric dimensions and electronic compatibility, which significantly expands the area of their mutual solubility. As a result, the driving thermodynamic forces of crystallization from the melt are stronger than amorphization. Thus, the use of materials that have their own high temperature resistance should be the basis for creating wear-resistant coatings. It is known that the main disadvantage of vacuum arc deposition is the presence of a micron-sized droplet fraction, which significantly affects the degree of wear of the protective coating.

As a sample for tribological tests, nitride multicomponent (Zr-Ti-Nb)N, (Zr-Ti-Nb-Cr)N and (Zr-Ti-Nb-Cr-Si)N coatings obtained by vacuum-arc deposition at the previously mentioned displacement potentials and working gas pressure were selected (see table 2). According to (Boxman & Zhitomirsky,), high values of technological parameters of deposition contribute to a decrease in the droplet fraction on the surface of coatings. The morphology of the surface of the test sample is shown in Figure 40. As can be seen from Figure 40, the coating has a homogeneous surface with minimal inclusion of microparticles. The presence of small craters is obviously associated with sputtering processes due to the high energy of the sprayed ions (Beresnev et al., 2016; Maksakova et al., 2017; Plotnikov et al., 2016; Pogrebnjak, Maksakova, Kozak et al, 2016). The study of surface morphology shows that deposition of coatings leads to an increase in surface roughness (0.088-0.42 μm for (Zr-Ti-Nb)N coatings and 1.02-1.82 μm for (Zr-Ti-Cr-Nb-Si)N) coatings due to the molten components of the droplets, which can be incorporated into the coating in the form of macroparticles. This is a typical phenomenon in the process of vacuum-arc deposition. Tribological tests were carried out on an automated friction machine of the brand "Tribometer"

(CSM Instruments) in air according to the "ball–disc" scheme at a temperature of 20°C. The discs on which the coatings were applied were made of 45 steel (HRC = 55) with a diameter of 42 mm, a height of 5 mm. A ball with a diameter of 6.0 mm, made of sintered certified material – Al_2O_3, was used as a counterbody. The load was 3.0 N, the sliding speed was 10 cm/s. The test conditions conformed to the international standards ASTM G99-959, DIN50324 and ISO 20808 (Kantay et al., 2021). Profilograms of the surface of the steel disc before and after the test are shown in Figures 41 and 42.

In the absence of coating, the average disc roughness is Ra = 0.088 microns. The application of a coating (Zr-Ti-Nb)N (6.7 μm thick) in a nitrogen reaction gas medium by vacuum-arc deposition on the polished surface of a steel disc leads to an increase in roughness (Figure 42) up to 0.42 μm. A noticeable increase in the roughness of the steel disc is obviously due to both the presence of a flow of macroparticles and the formation of craters during deposition of the coating. The results of tribological tests of the steel disc after coating are shown in Figure 43 and in Table 8.

An important parameter determining the performance of the coating is also its tribological characteristics (friction coefficient and wear factor). The coefficient of friction μ determines the adhesion strength of the rubbing materials, and the wear factor determines the resistance to wear (the smaller the wear factor, the higher the wear resistance). From the data presented in Figure 42 and in Table 8, it can be seen that the application of a nitride (Zr-Ti-Nb)N coating on steel 45 leads to an increase in the coefficient of friction from 0.674 to 1.95, which is consistent with the results of the study of the surface roughness of the steel disc.

Figure 40. SEM-images of the surface morphology of (Zr-Ti-Nb)N coatings obtained at Ub = -100 V: a – PN = 0.04 Pa, Ra » 1.17 μm; b – PN = 0.5 Pa, Ra » 0.42 μm

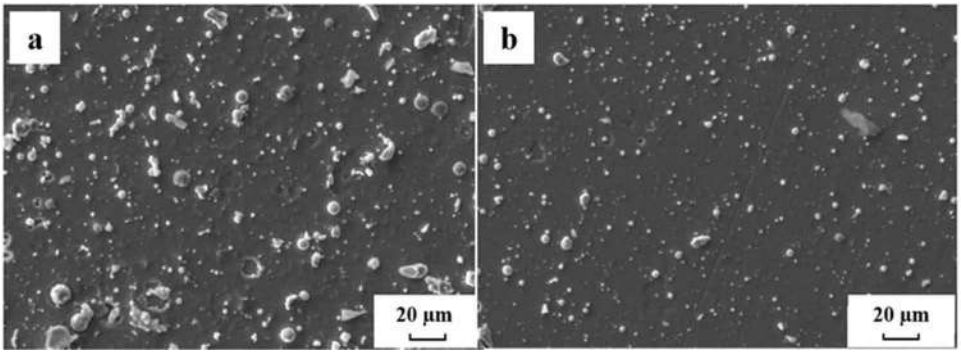

Figure 41. Surface roughness profile of the steel disc after polishing (R_a » 0.088 μm)

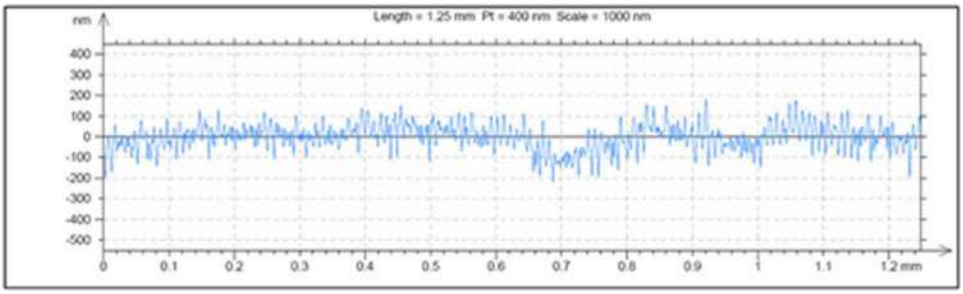

Figure 42. Profile of the surface roughness of the steel disk after deposition of the (Zr-Ti-Nb)N coating (Ra » 0.42 μm)

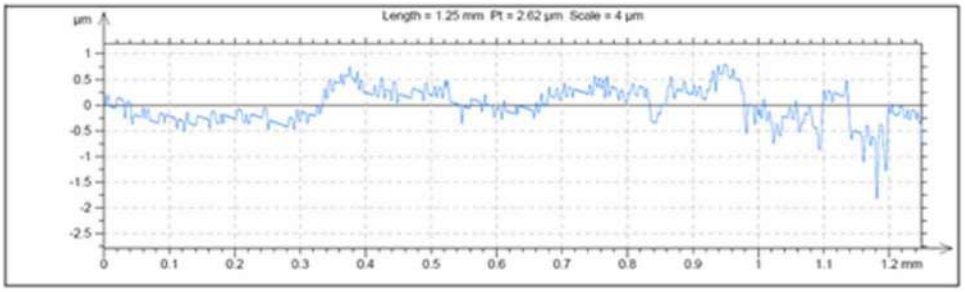

Figure 43. Results of tribological tests of a steel disk after (Zr-Ti-Nb)N coating

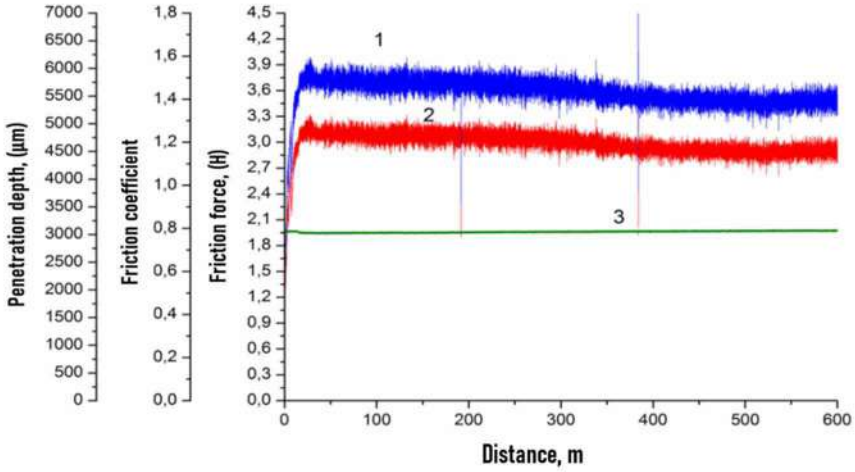

The friction coefficient takes on values from initial (during the first contact) to stationary (column "during tests" in Table 8) - when reaching constant values during tests. On all coated samples (series 1, 2), the friction coefficient was higher than 1.0. Such high values can be explained by the high roughness (Figure 40) associated with the presence of a droplet fraction on the surface and in the coating, which is formed during vacuum-arc deposition. The appearance of a solid droplet component, as well as the formation of wear products in the form of particles consisting of solid nitrides during the destruction of the coating, leads to abrasive wear of the coating. Reducing the roughness reduces the friction coefficient from 1.95 to 1.05. With an increase in hardness (see table 6) of the coating, the wear factor *W* of the coating decreases, while the counterbody increases (table 8). Of considerable interest is the study of friction tracks, as a result of which it is possible to draw a conclusion about the wear mechanism. It is known that the main mechanisms of wear of coatings during friction are: 1) adhesive wear, in which the coating material adheres to the counterbody; 2) abrasive wear, in which the formation of grooves on the surface of the material by a harder material of the counterbody occurs; 3) fatigue wear - the process of removing coating particles; 4) plastic deformation of the coating material.

Table 8. Tribological characteristics of the system "(Zr-Ti-Nb)N coating - Al_2O_3"

(Zr-Ti-Nb)N Coating, Series (Samples)	Friction Coefficient, μ		Wear Factor W, 10^{-5} mm³/N·m	
	Initial	During Testing	Counterbody	Coated Sample
1	0.61	1.95	0.391	9.69
2	0.491	1.05	3.21	2.4
Steel 45 (substrate)	0.204	0.674	0.269	35.36

Figure 44 (a) and (b) show photographs of the friction tracks of the (Zr-Ti-Nb)N coating obtained by vacuum-arc deposition. Analysing the images of the friction tracks of the coating under study, we can conclude that the presence of scratch marks, as well as particles of similar wear products (see Figure 44) indicate the abrasive nature of the wear of the coating. From the figures shown (Figure 43) it can be seen that the groove has a smooth surface. The presence of such a groove is obviously associated with a large number of defects in the coating. Figures 44b and 44d show the results of the analysis of wear products along the formed groove. The micrograph of the wear products clearly shows the presence of the counterbody material on the surface. The energy dispersive spectrum (Figures 44b and 44d) indicates the presence of aluminium oxide on the surface of the coating, which is obviously associated with the transfer of the counterbody material. This circumstance is confirmed by the data presented in Table 8, namely by comparing the wear factors of the counterbody and the test sample.

Figure 44. SEM-surface of the system (Zr-Ti-Nb)N coating after tribotechnical tests (a, c) and EDS-energy-dispersive spectra of friction tracks (b, d): a, b – sample series 1; c, d – sample series 2

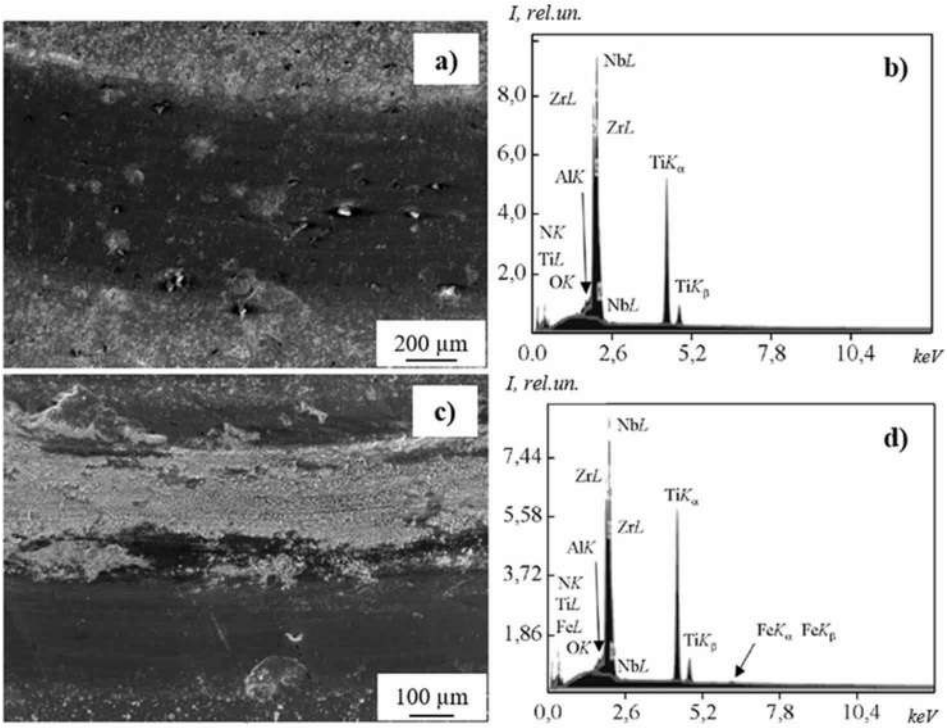

The results of processing profilograms indicate that the average value of the substrate roughness for non-deposited (Zr-Ti-Cr-Nb)N coatings is R_a = 0.088 μm, and it changes after coating deposition (Figure 45).

Figure 45. Surface roughness profile of (Zr-Ti-Cr-Nb)N coatings: a – series (sample) 1 (R_a » 1.88 μm); b – series (sample) 4 (R_a » 1.55 μm)

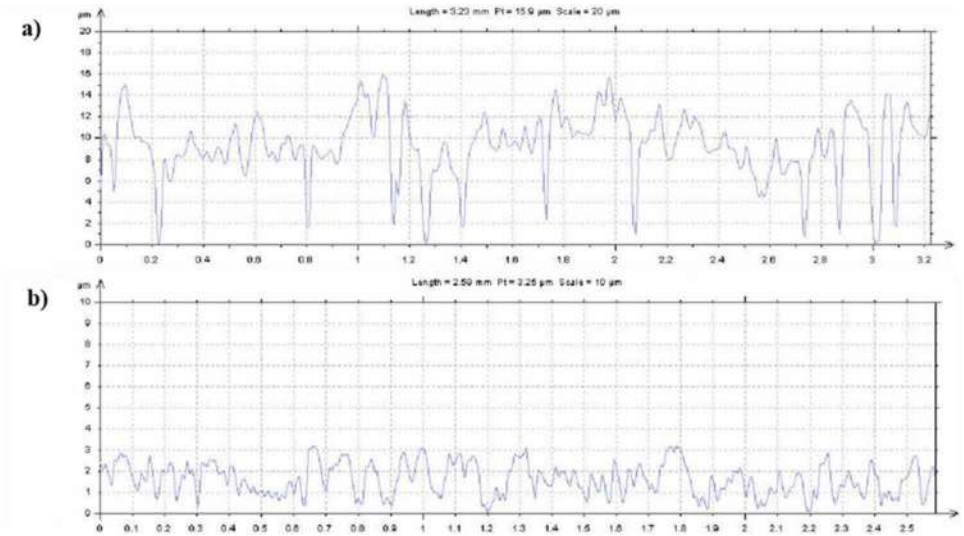

Figure 46. AFM-three-dimensional images of the (Zr-Ti-Cr-Nb)N coating surface: a – PN=0.3 Pa, Ub=-100 V, Ra=1.88 μm; b – PN=0,7 Pa, Ub=-100 V, Ra=1.83 μm; c – PN=0.3 Pa, Ub=-200 V, Ra=1.69 μm; d – PN=0.7 Pa, Ub=-200 V, Ra=1.55 μm

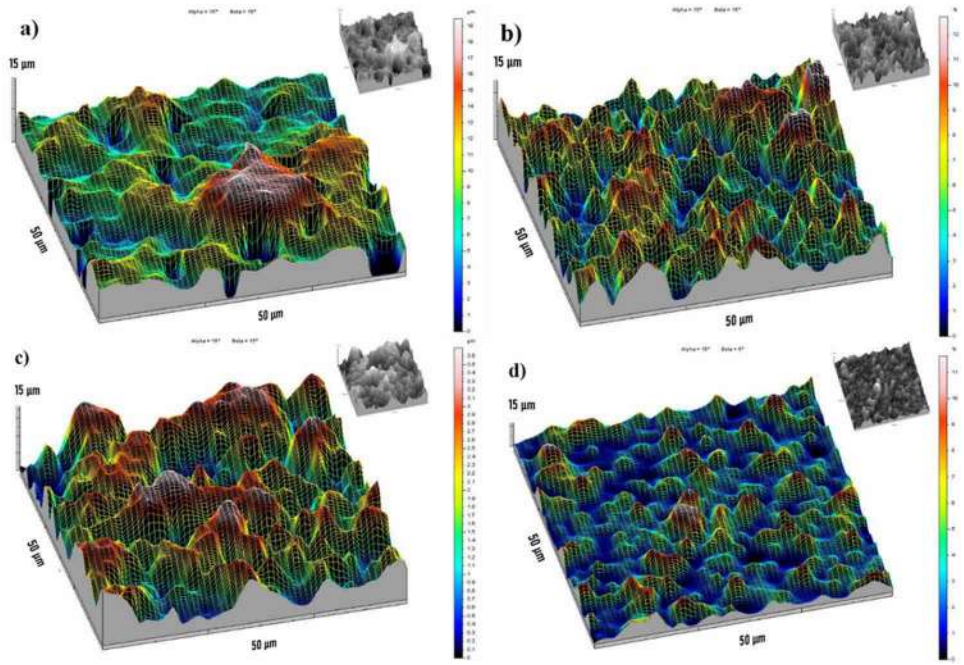

Figure 46 shows AFM-images of the topography surface of the coating of the 4th series of the (Zr-Ti-Cr-Nb)N system.

Comparison of the obtained data shows that the change in the roughness of the (Zr-Ti-Cr-Nb)N coating directly depends on the pressure of the nitrogen reaction gas and the mixing voltage. At a pressure of $P_N = 0.7$ Pa, the surface of the coating is more homogeneous, with clearly expressed droplet inclusions of small sizes. At a pressure of $P_N = 0.3$ Pa, incompletely melted compounds of the elements Ti, Zr, Cr, Nb, with nitrogen are formed on the surface of the coating.

Conclusions for Section 4

1. The relationship between the structural-phase state and the mechanical characteristics of the coatings has been studied. It has been established that the hardness of (Zr-Ti-Nb)N nitride coatings, depending on the physical parameters of deposition, varies from 37 to 45 GPa.
2. An analysis of experiments on measuring microhardness indicates that the hardness for (Zr-Ti-Cr-Nb)N coatings, depending on the physical parameters of deposition, is in the range from 31 to 44 GPa.
3. The influence of physical-technological parameters of deposition on the hardness and modulus of elasticity for (Zr-Ti-Cr-Nb-Si)N nitride coatings deposited at $P_N = 0.3$ Pa and $U_b = -100$ V, the hardness is 29 GPa, and the modulus elasticity is 291 GPa. With an increase in the bias potential on the substrate to -200 V, the hardness and elastic modulus decreased to 24 and 254 GPa, respectively.
4. It is shown that the application of a (Zr-Ti-Nb)N coating on a steel disk leads to an increase in the friction coefficient from 0.674 to 1.95. The study of wear resistance (wear factor) of the analysed coating showed a noticeable increase in the resistance of the sample to wear (0.039×10^{-5} $mm^3\times N^{-1}\times mm^{-1}$ and 35.36×10^{-5} $mm^3\times N^{-1}\times mm^{-1}$).
5. It was found that the adhesion of the studied coatings was improved by using higher deposition parameters (bias voltage on the substrate and nitrogen working gas pressure). Local wear of (Zr-Ti-Cr-Nb-Si)N coatings to the substrate material occurs when the load reaches the maximum value of 46N, for (Zr-Ti-Cr-Nb)N coatings - 62N and for (Zr-Ti- Nb)N - 66N.

CONCLUSION

The research results obtained in the course of this work made it possible to solve a scientific and technical problem, which consisted in the development of physical and technological foundations for the creation of multicomponent hard and superhard nanostructured coatings obtained by vacuum-arc deposition and the establishment of their structural-phase, physical-mechanical and tribological-technical characteristics. Also, in this work, the authors considered the role of Cr and Si addition on the properties of (Zr-Ti-Nb)N coatings, including morphology, relative hardness and adhesion. Based on the results of the research work obtained for the first time, the following conclusions are formulated:

1. Using complementary methods of analysis, the influence of the physical parameters of deposition (the pressure of the nitrogen working gas and the bias voltage of the substrate) on the elemental composition and phase structure of multicomponent nanostructured nitride (Zr-Ti-Nb)N, (Zr-Ti-Nb-Cr)N and (Zr-Ti-Nb-Cr-Si)N coatings obtained by vacuum-arc deposition, in which the formation of nanocrystallites with sizes ranging from 5.2 nm to 63 nm of various phases was found.

2. It has been found that the main phase in triple coatings is a solid solution phase with an FCC-lattice with a (111) growth texture and a small volume fraction of a phase with a BCC-lattice with a (110) growth texture.
3. It has been found that, as a result of adding Cr and Si elements to the cathode in succession, the TiN-based FCC-phase and the Cr_2N trigonal lattice phase are formed in the coatings in the first case, while in the second case, a solid solution of the FCC-lattice and (111) growth texture is also formed.
4. The relationship between the structural-phase state and the mechanical characteristics of the coatings is determined. An analysis of experiments on measuring hardness indicates that the highest hardness values were obtained in the (Zr-Ti-Nb)N coating - 37-45 GPa and (Zr-Ti-Nb-Cr)N - 31-44 GPa, at the same time, alloying with Si leads to a decrease in hardness to 24–29 GPa. The increase in the hardness of the coatings was due to the formation of a preferred orientation of crystallite growth with the (111) axis.
5. It is shown that with an increase in pressure in the chamber from 0.05 to 0.3-0.7 Pa, in some cases and an increase in the potential to the substrate from -100 to -200 V, the adhesion of coatings to the substrate increases. Local abrasion of coatings (Zr-Ti-Cr-Nb-Si)N to the substrate material occurs when the load on the indenter reaches 46N, for coatings (Zr-Ti-Nb-Cr)N - 62N, and for coatings from (Zr-Ti-Nb)N - 66N (i.e. the largest value).
6. It has been found that coating (Zr-Ti-Nb)N on a steel disk results in an increase in the friction coefficient from 0.674 to 1.95. A study of the wear resistance of the analyzed coating showed a noticeable decrease in the wear factor of the sample (0.391×10^{-5} $mm^3/N\cdot m$ and 35.36×10^{-5} $mm^3/N\cdot m$).

Summing up, these results represent a new step in solving the problem of creating protective coatings based on multicomponent systems. A change in the structural and phase properties that affect the increase in the operational characteristics of various products operating at high temperatures, loads and wear rates.

REFERENCES

Anishik, V. M., Ponaryadov, V. V., & Uglov, V. V. (2011). *Difraktsionnyy analiz.*

Azarenkov, N. A., Sobol, O. V., & Pogrebnjak, A. D. (2012). Materyalovedenye neravnovesnogo sostoyania modificirovannoy poverhnosti. Sumy, Sumy State University.

Bagdasaryan A.A., Smirnova E., Konarski P., Misnik M. & Zawada A. (2014). The analysis of elemental composition and depth profiles of nitride nanostructures coating based on the TiHfVNbZr high-entropy alloy. *JNEP*, (6), 1–5.

Beresnev, V. M., Sobol, O. V., Grankin, S. S., Nemchenko, U. S., Novikov, V. Y., Bondar, O. V., Belovol, K. O., Maksakova, O. V., & Eskermesov, D. K. (2016). Physical and mechanical properties of (Ti–Zr–Nb)N coatings fabricated by vacuum-arc deposition. *Inorganic Materials: Applied Research*, *7*(7), 388–394. doi:10.1134/S2075113316030047

Boxman R.L. & Zhitomirsky V.N. Vacuum-arc deposition devices. *Review Science Instruments* (77), 1 – 15.

Cecchini, R., Fabrizi, A., Cabibbo, M., Paternoster, C., Mavrin, B. N., Denisov, V. N., Novikova, N. N., & Haidopoulo, M. (2011). Mechanical, microstructural and oxidation properties of reactively sputtered thin Cr/N coatings on steel. *Thin Solid Films*, *519*(19), 6515–6521. doi:10.1016/j.tsf.2011.04.115

Engel, L. (1986). *Rastrovaya electronnaya microskopia*. Metallurgy.

Ganeyev, A. A., Gubal', A. R., Uskov, K. N., & Potapov, S. V. (2012). Analiticheskaya mass-spektrometriya s tleyushchim razryadom. Izvestiya Akademii Nauk. *Seriya Khimicheskaya*, (4), 1–17.

Gavaleiro, A., & De Hosson, J. T. (2006). *Nanostructured Coating*. Springer-Verlag. doi:10.1007/978-0-387-48756-4

Geller, Yu. A., & Rakhshadt, A. G. (1989). *Materialovedeniye. Metody analiza, laboratornyye raboty i zadachi*. Metallurgiya.

Gladkikh, A. I., Malykhin, S. V., & Pugachev, A. T. (2006). *Difraktsionnyye metody analiza vnutrennikh napryazheniy, Teoriya i eksperiment*. NTU HPI.

Godet, M., Berthier, Y., Vincent, L., & Flamand, L. (1991). Hard coatings for tribological applications: A pluridisciplinary approach. *Surface and Coatings Technology*, *45*(1-3), 1–8. doi:10.1016/0257-8972(91)90199-7

Golovin, Yu. I. (2008). Nanoindentirovaniye i mekhanicheskiye svoystva tverdykh tel v submikroob"yemakh, tonkikh pripoverkhnostnykh sloyakh i plenkakh. *FTT*, *50*(12), 2113–2140.

Gouldsteyn, Dj., N'yuberi, D., & Echlin, P. (1984). Rastrovaya elektronnaya mikroskopiya i rentgenovskiy mikroanaliz. *Mir, Moscow*, (2), 348.

Holleck, H. (1988). Metastable coatings – Prediction of composition and structure. *Surface and Coatings Technology*, *36*(1-2), 151–159. doi:10.1016/0257-8972(88)90145-4

Holmberg, K., & Matthews, A. (1994). Coating's tribology: A concept, critical aspects and future directions. *Thin Solid Films*, *253*(1-2), 173–178. doi:10.1016/0040-6090(94)90315-8

Hones, P., Sanjine, R., & Levy, F. (1998). Sputter deposited chromium nitride based ternary compounds for hard coatings. *Thin Solid Films*, *332*(1-2), 240–246. doi:10.1016/S0040-6090(98)00992-4

Hsieh, M. H., Tsai, M. H., Shen, W. J., & Yeh, J. W. (2013). Structure and properties of two Al-Cr-Nb-Si-Ti high-entropy nitride coatings. *Surface and Coatings Technology*, *221*, 118–123. doi:10.1016/j.surfcoat.2013.01.036

Kantay N., Rakhadilov B., Kurbanbekov Sh., Yeskermessov D., Yerbolatova G. & Apsezhanova A. (2021). Influence of detonation-spraying parameters on the phase composition and tribological properties of Al2O3 coatings. *Coatings, 11*(7), 793, 1-10.

Kim, H., Choi, S. R., & Yoon, S. Y. (2002). Superhard Ti-Si-N coatings by a hybrid system of arc ion plating and sputtering techniques. *Surface and Coatings Technology*, *161*(2-3), 243–248. doi:10.1016/S0257-8972(02)00499-1

Kim, S. K., & Cha, B. C. (2005). Deposition of tantalum nitride thin films by D.C. magnetron sputtering. *Thin Solid Films*, *475*(1-2), 202–207. doi:10.1016/j.tsf.2004.08.059

Lee, G. R., Kim, H., Choi, H. S., & Lee, J. J. (2007). Superhard tantalum-nitride films formed by inductively coupled plasma-assisted sputtering. *Surface and Coatings Technology*, *201*(9-11), 5207–5210. doi:10.1016/j.surfcoat.2006.07.207

Leng, Y. X., Sun, H., Yang, P., Chen, J. Y., Wang, J., Wan, G. J., Huang, N., Tian, X. B., Wang, L. P., & Chu, P. K. (2001). Biomedical properties of tantalum nitride films synthesized by reactive magnetron sputtering. *Thin Solid Films*, *398-399*, 471–475. doi:10.1016/S0040-6090(01)01448-1

Liang, S. C., Chang, Z. C., Tsai, D. C., Lin, Y.-C., Sung, H.-S., Deng, M.-J., & Shieu, F.-S. (2011). Effects of substrate temperature on the structure and mechanical properties of (TiVCrZrHf)N coatings. *Applied Surface Science*, *257*(17), 7709–7713. doi:10.1016/j.apsusc.2011.04.014

Maksakova, O. V., Beresnev, V. M., & Eskermesov, D. K. (2017). Effects of Cr and Si additions under the various deposition conditions on the mechanical properties of the (Zr-Ti-Nb)N coatings. *Proceedings of the 2017 IEEE 7th International Conference on Nanomaterials: Applications & Properties*, (1), 1-6.

Martin, P. J., Bendavid, A., Cairney, J. M., & Hoffman, M. (2005). Nanocomposite Ti-Si-N, Zr-Si-N, Ti-Al-Si-N, Ti-Al-V-Si-N thin film coatings deposited by vacuum-arc deposition. *Surface and Coatings Technology*, *200*(7), 2228–2235. doi:10.1016/j.surfcoat.2004.06.012

Morris, D. G. (1998). Material. Science foundation, Trans Technical publication LVD.

Nordin, M., Larsson, M., & Hogmark, S. (1998). Mechanical and tribological properties of multilayered PVD TiN/CrN, TiN/MoN, TiN/NbN and TiN/TaN coatings on cemented carbide. *Surface and Coatings Technology*, *106*(2-3), 234–241. doi:10.1016/S0257-8972(98)00544-1

Nordin, M., Larsson, M., & Hogmark, S. (1999). Mechanical and tribological properties of multilayered PVD TiN/CrN. *Wear*, *232*(2), 221–225. doi:10.1016/S0043-1648(99)00149-0

Oliver, W. C., & Pharr, G. M. (1992). An improved technique for determining hardness and elastic modulus using load and displacement sensing indentation experiments. *Journal of Materials Research*, *7*(7), 1564–1583. doi:10.1557/JMR.1992.1564

Palatnik, L. S., Fuks, M. Y. A., & Kosevich, V. M. (1972). *Mekhanizm obrazovaniya i substruktura kondensirovannykh plenok*. Nauka.

Pilloud, D., Pierson, J. F., Marques, A. P., & Cavaleiro, A. (2004). Structural changes in Zr-Si-N films vs. their silicon content. *Surface and Coatings Technology*, *180-181*(180), 352–356. doi:10.1016/j.surfcoat.2003.10.087

Plotnikov, S. V., Pogrebnjak, A. D., Yerokhina, L. N., Yeskermessov, D. K., & Erdybaeva, N. K. (2016). Study of nanostructured (Ti-Zr-Nb)N coatings' physical- mechanical properties obtained by vacuum arc evaporation. *IOP Conference Series: Material Science and Engineering, 110*(1), 1-6 (012031). 10.1088/1757-899X/110/1/012031

Pogrebnjak, A. D., Maksakova, O., Kozak, C., Koltunowicz, T. N., Grankin, S., Bondar, O., Eskermesov, D. K., Drozdenko, A., Petrov, S., & Erdybaeva, N. (2016). *Przegląd Elektrotechniczny*, (8), 180–183.

Pogrebnjak, A. D., Yakushchenko, I. V., Bondar, O. V., Beresnev, V. M., Oyoshi, K., Ivasishin, O. M., Amekura, H., Takeda, Y., Opielak, M., & Kozak, C. (2016). Irradiation resistance, microstructure and mechanical properties of nanostructured (TiZrHfVNbTa)N coatings. *Journal of Alloys and Compounds*, *679*, 155–163. doi:10.1016/j.jallcom.2016.04.064

Pogrebnjak, A. D., Yakushchenko, I. V., Bondar, O. V., Sobol', O. V., Beresnev, V. M., Oyoshi, K., Amekura, H., & Takeda, Y. (2015). Influence of Implantation of Au- Ions on the Microstructure and Mechanical Properties of the Nanostructured Multielement (TiZrHfVNbTa)N Coating. *Physics of the Solid State*, *57*(8), 1559–1564. doi:10.1134/S1063783415080259

Pogrebnyak, A. D., Ponomarev, A. G., Shpak, A. P., & Kunitskiy, Yu. A. (2012). Primeneniye mikro- i nanozondov dlya analiza malorazmernykh 3D materialov, nanosistem i nanoobyektov. *UFN*, *182*(3), 287–321.

Ramalingam, S., & Zheng, L. (1995). Film-substrate interface stresses and their role in the tribological performance on surface coatings. *Tribology International*, *28*(3), 145–161. doi:10.1016/0301-679X(95)98963-E

Randall, N. (2002). Overview of mechanical testing standards. *CSM Instruments Applications Bulletin*, (18), 3.

Rizzo, A., Signore, M. A., Penza, M., Tagliente, M. A., De Riccardis, F., & Serra, E. (2006). RF sputtering deposition of alternate TiN/ZrN multilayer hard coatings. *Thin Solid Films*, *515*(2), 500–504. doi:10.1016/j.tsf.2005.12.279

Samsonov G.V. (1969). Nitridy. *Scientific Opinion*, 380.

Shin, C. S., Kim, Y. W., Gall, D., Greene, J. E., & Petrov, I. (2002). Phase composition and microstructure of polycrystalline and epitaxial TaNx layers grown on oxidized Si(001) and MgO(001) by reactive magnetron sputter deposition. *Thin Solid Films*, *402*(1-2), 172–182. doi:10.1016/S0040-6090(01)01618-2

Shulayev, V. M., Anreyev, A. A., & Rudenko, V. P. (2006). Moderniacia vacuumno-dugovih ustanovok dlya sinteza pokriti i azotirovania metodom ionnoy implantacii i osajdenia. *FIP*, *4*(3-4), 136–142.

Shypylenko, A., Pshyk, A. V., Grzeskowiak, B., Medjanik, K., Peplinska, B., Oyoshi, K., Pogrebnjak, A., Jurga, S., & Coy, E. (2016). Effect of ion implantation on the physical and mechanical properties of Ti-Si-N multifunctional coatings for biomedical applications. *Materials & Design*, *110*, 821–829. doi:10.1016/j.matdes.2016.08.050

Thornton, J. A. (1982). *Deposition technologies for films and coating*. Noyes Publications.

Troyan, V. I., Pushkin, M. A., Borman, V. D., & Tronin, V. N. (2008). *Fizicheskie osnovi metodov issledovania nanostruktur i poverhnosti tverdogo tela*. MIFI.

Tsai, D. C., Huang, Y. L., Lin, S. R., Liang, S.-C., & Shieu, F.-S. (2010). Effect of nitrogen flow ratios on the structure and mechanical properties of (TiVCrZrY)N coatings prepared by reactive magnetron sputtering. *Applied Surface Science*, *257*(4), 1361–1367. doi:10.1016/j.apsusc.2010.08.078

Uglov, V. V., Chereda, N. N., & Anishin, V. M. (2007). *Metodi analiza elementnogo sostava poverhnostnih sloev. Learning guide*. Belarusian State University.

Umanskiy, Ya. S., Skakov, Yu. A., Ivanov, A. N., & Rastorguyev, L. N. (1982). *Kristallografiya, rentgenografiya i elektronnaya mikroskopiya*. Metallurgiya.

Veprek S. (2013). Recent search of new superhard materials: Go nano. *Journal Vacuum Science Technology A*(31), 1-33.

Vershinin D.S., Smolyakova M.Yu., Manokhin S.S., Druchinina O.A. & Akhmadeyev Yu.H. (2010). Issledovaniye tribologicheskikh svoystv azotirovannogo titanovogo splava VT16. Zavodskaya laboratoriya. *Diagnostika materialov, 76*(12), 45-49.

Voevodin, A. A., Shtansky, D. V., Levashov, E. A., & Moore, J. J. (2004). *Nanostructured Thin Films and Nanodispersion Strengherred Coatings*. Kluger Academic. doi:10.1007/1-4020-2222-0

Wagner, C. D. (1995). Handbook of XPS. Physical Electronics.

Yamamoto, K., Sato, T., Takahara, K., & Hanaguri, K. (2003). Properties of (Ti,Cr,Al)N coatings with high Al content deposited by new plasma enhanced arc-cathode. *Surface and Coatings Technology*, *174-175*(174), 620–626. doi:10.1016/S0257-8972(03)00580-2